UNIVERSITÉ DE SHERBROOKE
Faculté de génie
Département de génie mécanique

APPAREIL ET MÉTHODE FACILITANT LA RECANALISATION DES OCCLUSIONS TOTALES CHRONIQUES VIA LA TRANSMISSION D'ONDES MÉCANIQUES DANS UN FIL GUIDE

DEVICE AND METHOD TO FACILITATE CROSSING OF CHRONIC TOTAL OCCLUSIONS VIA THE TRANSMISSION OF MECHANICAL WAVES IN A GUIDEWIRE

Thèse de doctorat
Specialité: génie mécanique

Louis-Philippe RIEL

Sherbrooke (Québec) Canada

Juillet 2018

JURY MEMBERS

Martin BROUILLETTE

Supervisor

Alain BERRY

Examiner

Denis RANCOURT

Examiner

Simon BÉRUBÉ

Examiner

RÉSUMÉ

Les maladies vasculaires périphériques et coronariennes touchent des millions de personnes dans le monde. Les occlusions totales chroniques (CTO), qui représentent un blocage complet des artères, sont l'une des conséquences de ces maladies cardiovasculaires. Une CTO peut être observée dans les jambes et dans les artères coronaires. Une CTO située dans les coronaires peut causer l'angine de poitrine tandis qu'une CTO périphérique peut causer une claudication pouvant conduire jusqu'à une amputation du membre inférieur. Les principales causes menant à un échec d'une procédure de recanalisation percutanée d'une CTO sont la présence de calcification, une tortuosité sévère des artères, la présence d'un cap proximal convexe, la longueur de l'occlusion ainsi qu'un échec précédent. L'absence d'un appareil simple, efficace et sécuritaire pour la recanalisation percutanée d'une CTO a motivé les présents travaux de recherche.

L'objectif principal des travaux de recherche présentés ici consiste à concevoir, développer et fabriquer un appareil facilitant la recanalisation des occlusions totales chroniques via la transmission d'ondes mécaniques dans un fil guide. Les objectifs secondaires consistent à évaluer les résultats préliminaires liés à l'efficacité et la sécurité d'un tel appareil.

L'appareil proposé a deux principales composantes : (i) le générateur d'ondes de choc (ou console) et (ii) le fil guide actif. La console utilise des transducteurs piézoélectriques pour convertir les signaux électriques des amplificateurs en ondes mécaniques. Ces ondes sont ensuite amplifiées en se propageant dans le réflecteur parabolique et le guide dispersif. Un mécanisme de connexion est ajouté à la console pour faciliter la transmission des ondes mécaniques vers le fil guide actif. Le design et la construction du fil guide actif sont similaires à ceux des fils guides conventionnels. Les ondes mécaniques transmises le long du fil guide actif créent un effet marteau piqueur et un mouvement de fluide devant le fil qui favorisent ces performances. De plus, le système proposé ne génère aucune chaleur au bout du fil et a la capacité de différencier les tissus en fonction de leur élasticité.

Plusieurs expériences ont été proposées afin d'évaluer les performances préliminaires de l'appareil de recanalisation. Le profil de sécurité de la technologie a été évalué en analysant la réponse des cellules de l'endothélium suite à une exposition au fil guide actif et à l'énergie des ondes mécaniques. Une étude animale sur des cochons sains a aussi été conduite afin d'évaluer les effets adverses associés à l'appareil et d'analyser les artères coronariennes traitées avec le fil guide actif. L'efficacité de l'appareil a été évaluée en mesurant la pression dans l'eau tout près du bout du fil guide actif. Des tests ont aussi été effectués afin d'évaluer les performances de recanalisation de l'appareil sur des matériaux analogues aux calcifications vasculaires et sur des vraies CTOs ex-vivo. Des résultats prometteurs ont été obtenus tant d'un point de vue de l'efficacité que de la sécurité de l'appareil.

Mots-clés : Angioplastie, recanalisation, occlusion totale chronique, onde mécanique, fil guide

ABSTRACT

Peripheral Arterial Disease (PAD) and Coronary Heart Disease (CHD) affects million of people over the world. Chronic Total Occlusions (CTO) are a prevalent and problematic condition in cardiovascular medicine. CTOs can be found in the lower extremities of patients with PAD, and in the coronary arteries of patients with CHD. CTOs are defined as totally occluded arterial segments that have remained occluded for an extended period. This may cause angina in the case of a coronary CTO, or claudication possibly leading to limb amputation in the case of a peripheral CTO. The principal causes associated with the failure of a CTO angioplasty are the presence of calcification, severe tortuosity, blunt proximal cap morphology, CTO length and prior failed attempt. The lack of a simple, effective and safe angioplasty CTO crossing device has led to this research project.

The main goal of this thesis was to design, develop and build a device to facilitate crossing of CTOs via the transmission of mechanical waves in a guidewire. The secondary goals were to evaluate the preliminary safety and efficacy of such device.

The proposed CTO crossing system has two main components: (i) the shock wave generator (console) and (ii) the active guidewire. Inside the console generator, piezoelectric transducers are used to convert amplified electric signals into mechanical waves. These waves are further amplified as they are traveling in the parabolic reflector and dispersive waveguide. A connector is used to mechanically join the console generator with the active guidewire. The active guidewire design, construction and method of use are similar to conventional guidewire with the difference that it can transmit mechanical waves. These mechanical waves create a micro-jackhammer effect at the distal tip of the active guidewire and fluid motion that are believed to enhance its crossing ability. In addition, the proposed CTO crossing system avoids heat accumulation at the tip of the active guidewire and can differentiate tissues based on their elasticity.

Different experiments were proposed to evaluate the preliminary safety and efficacy performance of the CTO crossing system. The safety profile of the technology was evaluated by looking at the endothelial cell response when exposed to the active guidewire with mechanical energy delivery. An in-vivo study on healthy pigs was also used to evaluate the technical handling of the active guidewire. In addition, safety was assessed by looking at adverse events during the procedure and histology analysis of the treated arteries. Efficacy was evaluated by measuring the output pressure in water near the distal tip of the active guidewire. Crossing ability was also assessed on the bench using surrogate materials and ex-vivo CTO specimens. Promising safety and efficacy results were demonstrated and motivated to continue the development of this unique technology.

Keywords: Angioplasty, recanalization, chronic total occlusion, mechanical wave, guidewire

À mes parents, Céline et Claude

ACKNOWLEDGEMENTS

The author would like to thank all people who contributed to this research work. In particular, the author will like to thank Gabriel and Charles Bertrand from the support staff of the engineering faculty of the Université de Sherbrooke, Étienne Bousser for his help with the nanoindentation, Annie Vaillancourt and the other animal technicians from the research center of the Centre Hospitalier Universitaire de Sherbrooke, all the group from the Montreal Heart Institute and specially Dr Jean-François Tanguay, Marie-Jeanne Bertrand, Pascale Geoffroy and Marie-Élène Clavet-Lanthier, and Dr Marc-Antoine Despatis for his help with the amputations.

The author would like to thank the financial support from the Fonds de Recherche sur la Nature et Technologies du gouvernement du Québec (FQRNT). The author would also like to thank members of its Jury for their support, understanding and patience. A special thank to Dr Simon Bérubé who played an instrumental role to facilitate access to ex-vivo chronic total occlusion specimens.

Another thank to the SoundBite team. Without them, it would have been impossible to transform this technology into a real medical device. Your trust, hard work and perseverance are impressive. I'm learning everyday with you. You made my dream became a reality. A special thank to Maude, Klaus, Gholamreza and Manuel who took a big risk by joining the company at its early stage. Another special thank to Dustin who help with the review of this manuscript. One last thank to Steve Arless who first believed in us and in the technology.

Another special thanks to my girlfriend Frédérique Morin, my parents, family and friends who supported me, and helped me stay focus and motivated.

Finally, the author will like to acknowledge and thank the support of Martin Brouillette and Steven Dion. Thank you for giving me the opportunity to participate in this incredible adventure. You are truly inspirational and great role model. Your passion, optimism, kindness, work ethic, sense of humor, life balance and vast knowledge are outstanding. You motivate me to bring my best game everyday.

TABLE OF CONTENTS

LIST OF FIGURES

LIST OF TABLES

CHAPTER 1

INTRODUCTION

1.1 Context

Chronic Total Occlusions (CTO) are a prevalent and problematic condition in cardiovascular medicine. CTOs can be found in the lower extremities of patients with Peripheral Arterial Disease (PAD), and in the coronary arteries of patients with Coronary Heart Disease (CHD). PAD affects approximately 0.8 million Canadians and 9 million Americans [113] while CHD affects approximately 2.4 million Canadians and 15 million Americans [82, 159].

CTOs are defined as totally occluded arterial segments that have remained occluded for an extended period (i.e. greater than 3 months as evaluated by patient symptoms, prior angiography and/or CTO composition) [12, 183]. The presence of a CTO reduces blood supply to muscle which lead to ischemia. This may cause angina in the case of a coronary CTO, or claudication possibly leading to limb amputation in the case of a peripheral CTO. Recanalization of coronary CTOs can improve left ventricular function, reduce risk of arrythmias and better tolerance of an acute coronary syndrome [41]. Recanalization of peripheral CTOs is of particular importance considering that the rate of death after lower extremity amputation in the United States is approximately 48% at 1 year and 71% at 3 years [188].

CTOs are common in PAD patients. Femoropopliteal and infrapopliteal (together grouped as infrainguinal) artery CTOs are present in up to 50% of patients with claudication or critical limb ischemia (CLI) [17, 175]. CTOs are also common in patients diagnosed with coronary arterial disease on angiography, occurring in about 15% to 50% of patients [41, 66, 196].

Previously, patients with peripheral CTOs would have been referred for bypass surgery. More recently, bypass surgery was shown to be associated with increased morbidity, increased mortality risks and significant costs to the healthcare system. Supported by the BASIL trial [1], a new trend has emerged whereby minimally invasive peripheral endovascular treatments have gained greater use over conventional surgery [16, 131].

1. Bypass versus Angioplasty in Severe Ischaemia of the Leg.

Similarly the presence of vascular coronary CTO is also associated with higher rates of referral for coronary artery bypass graft surgery (CABG) [19]. The principal causes of percutaneous coronary intervention (PCI) CTO crossing failure are the presence of calcification, severe tortuosity, blunt proximal cap morphology, CTO length and prior failed attempt [49, 174]. However, the SYNTAX trial [2] suggests that CTO-PCI is becoming an acceptable alternative to CABG for patients with less complex CTO disease [124]. This trend is also supported by the recent increase in CTO-PCI success rate [48].

The use of a conventional wire coupled with a support catheter has been documented to cross infrainguinal CTOs in 40-60% of cases (crossing failure rate of 40-60%) [20, 35]. With the introduction of subintimal technique (passage of the guidewire between the layers of the arterial wall, refer to section 2.1), re-entry devices and hydrophilic guidewires, the success rates have increased to approximately 80% (crossing failure rate of approximately 20%) although this statistic is largely limited to above-the-knee occlusions and to experimented operators [16, 112, 117]. Success rates for infrapopliteal vessels are lower. It was shown that success rate was about 75% for lesions shorter than 15 cm long and approximately 54% for occlusions longer than 15 cm long [162]. Subintimal tracking and re-entry in the true lumen remain challenging in infrapopliteal arteries due to smaller vessel size and increased calcification [169]. It was also found that distal CTOs were more calcified than proximal ones [34]. The crossing failure rates in femoropopliteal and infrapopliteal vessels suggest that there remains an unmet need to cross CTOs.

In recent years, several new specialty crossing devices have attempted to improve crossing success rates of CTO intervention [5, 169]. These devices are typically larger than wires, more complex to use and incorporate some type of energy. Their mechanisms of action vary widely, and include:

- rotational drilling [36];
- radiofrequency ablation [96];
- photochemical ablation [103];
- blunt dissection [206];
- mechanical vibration [193];

In a recent publication on data from the multicenter Excellence in Peripheral Artery Disease (XLPAD) database, primary crossing success of specialty crossing devices was 72.1% (crossing failure rate of 27.9%) as opposed to 51.9% (crossing failure rate of 48.1%) with guidewire-catheter [20]. However, fluoroscopy time, contrast volume and procedure duration were all significantly higher for specialty crossing devices versus guidewire-catheter.

2. Synergy between PCI with Taxus and Cardiac Surgery.

Also, the use of specialty crossing devices is limited due to equipment cost and operator experience [20].

Most of the new specialty crossing devices are only used in peripheral interventions. Not many of these technologies were able to penetrate the coronary CTO market. Coronary CTO-PCI operators continue to use a combination of various non-energized guidewires, microcatheters and balloons to cross CTO. Recent improvements in coronary CTO crossing rates have been obtained by the use of new advanced crossing strategies (dissection re-entry, retrograde, etc.) and the so-called Hybrid algorithm [42, 196, 208]. The Hybrid algorithm uses angiographic characteristics from the CTO (proximal cap ambiguity, length, etc.) to guide the choice of the crossing strategy and crossing techniques before and during the procedure. For example, the OPEN-CTO registry study reported a CTO crossing rate of 86% using the Hybrid approach [160]. In comparison, a meta-analysis of published studies, from 1979 to 2006, that compared CTO recanalization to medical management showed that the recanalization success rate was of only 69% [95]. Techniques in the Hybrid algorithm are used by only a few high volume and dedicated expert operators [48, 76, 174]. In an analysis of the National Cardiovascular Data Registry, a CTO-PCI procedural success rate of 59% was reported in less experienced centers [139]. The lower success rate achieved by less experienced operators suggests that there is still an opportunity to develop a new easy-to-use device that can fit into conventional techniques to facilitate CTO crossing.

The crossing failure rates, the devices complexity, the longer procedure time and the steep learning curve suggest that there remains an unmet need to address the field of CTO crossing. The lack of a simple, effective and safe CTO crossing wire or specialty device has led to the research work described in this thesis.

1.2 Objective and assumptions

To address the aforementioned limitations in CTO crossing, the main objective of this thesis was to answer the following research question: "*Is it possible to facilitate crossing of chronic total occlusion using mechanical waves transmitted along a guidewire inserted inside the vascular system?*". To answer this question, the following objectives were proposed:

1. Design, develop and build a mechanical wave generator capable of producing high amplitude mechanical waves.

2. Design, develop and build an active guidewire that can transmit mechanical waves up to CTO located in a tortuous vascular anatomy.
3. Investigate preliminary safety and efficacy of the system (generator and active guidewire) through various bench tests, ex-vivo and in-vivo studies.

It is assumed that the use of mechanical waves delivered via a guidewire platform, referred here as the active guidewire, can safely and efficiently facilitate the crossing of CTOs. First, this hypothesis is supported by the fact that interventionists are already familiar with the use of guidewires for angioplasty procedure. By proposing a device having similar properties, geometry and construction to commercially approved guidewires, it is anticipated that adoption by specialists will be favorable. Second, this hypothesis is supported by the use of an energy source that was proven to be safe and effective in many other medical devices. For examples, mechanical waves are used in diagnostic imaging, drug delivery therapy and high-power low-frequency device for tissue fragmentation [123, 132]. Extracorporeal lithotripsy also uses shock waves generated outside the patient and focused toward a kidney stone inside the patient to break it into smaller pieces [64]. By doing so, elimination through the urinary track is facilitated. Another example is the lithoplasty technology developed by Shockwave Medical (Fremont, United States) to facilitate low-pressure balloon inflation during angioplasty procedure [172].

1.3 Original contribution

This research project is in continuation with previous work initiated during my Master degree. The goal of my Master research project was to demonstrate the potential of a mechanical wave generator that can be used for intracorporeal lithotripsy and interventional cardiology [152]. Even though the potential of such device was demonstrated, it was still limited in terms of performance, size, durability and usability. Moreover, the previous device did not have a guidewire platform to deliver the mechanical waves inside arteries and did not use the same mechanism to amplify the mechanical waves.

Another complementary research project is ongoing at the Laboratoire d'Onde de Choc de l'Université de Sherbrooke (LOCUS) which uses a similar energy source, but in the context of another medical application. This other project is related to the development of a novel extracorporeal lithotripter apparatus using piezoeletric transducers in combination with dispersive mechanical wave amplifiers [59]. Even though both projects share a similar energy source, specific requirements associated to each individual application need to be addressed in their own unique way.

The original contribution of this thesis is related to the method used to generate, amplify and transmit the mechanical waves up to the site of an arterial occlusion. In this research work, it is proposed to combine the use of a parabolic reflector and a dispersive waveguide to spatially and temporally compress many small amplitudes waves, generated by discrete piezoeletric transducers, into one single large amplitude wave (i.e. a shock wave). Also, it is proposed to use a guidewire platform, connected to a generator, to efficiently and safely transmit these shock waves up to the occlusion. The resulting micro-jackhammer effect at the distal tip of the active guidewire presents unique advantages to facilitate CTO crossing.

1.4 Thesis outline

This thesis is divided into six chapters: introduction, background, method, results, discussion and conclusion. The background chapter will review the vascular anatomy, CTO pathophysiology and current technologies in the field of CTO angioplasty. This chapter will also cover the wave propagation theories underlying the technology proposed here. The method chapter will present the experimental and numerical methods used during design, and the experimental protocols used for verification of the system's performance. The results chapter will describe the final design of the proposed CTO crossing system and the outcomes from the various performance tests. The discussion chapter will expand on the key results from performance testing, describe the system's mechanisms of action and expand on potential device improvements. Lastly, the system performance will be compared against the research objectives and a brief summary of the work that took place following this research project will be presented.

CHAPTER 2

BACKGROUND

This chapter presents the arterial anatomy and the atherosclerosis development leading to the formation of a chronic total occlusion. Treatment options are described and emphasis is put on the minimally invasive percutaneous transluminal angioplasty (PTA) procedure. New CTO crossing techniques, guidewire construction and specialty CTO crossing devices are presented. Lastly, theories associated with the propagation of elastic waves in a solid are explained.

2.1 Chronic total occlusion

The cardiovascular system allows for the circulation of blood across the body through a network of arteries and veins. The main function of blood is to distribute and exchange nutrients, oxygen, electrolytes and waste product to/from surrounding tissues. For example, blood passing through the lungs absorbs oxygen that will then be used to fuel the muscle cells. Simultaneously, blood removes carbon dioxide that was created in the muscle cells as a byproduct of energy consumption. Blood circulation is maintained around the body by the heart.

Arteries are used to carry blood from the heart to the different tissues and organs. Arteries are strong and generally thick vessels that can sustain the high pressure load from the heart (usually around 120 mmHg). As shown in figure 2.1, the artery wall is composed of three main layers: intima, media and adventitia [100]. The first layer of cells in contact with blood, and within the intima, is called the endothelium. This single cell layer has many key regulatory functions [151]. The endothelial cells act as semi-selective barrier controlling the passage of material in and out of the bloodstream. It also provides a non-thrombogenic surface to avoid blood from clotting. The endothelial cells also regulate vascular tone. The media layer is principally composed of smooth muscle cells (SMC) that can contract or dilate to change the vessel diameter in response to various stimuli. The media is bound by the internal and external elastic lamina. The adventitia is the outer layer and is mostly composed of connective tissue.

Atherosclerosis is an arterial disorder associated with thickening of the inner wall (plaque formation) resulting from the deposition of lipids in the vessel intima [100, 207]. Both coro-

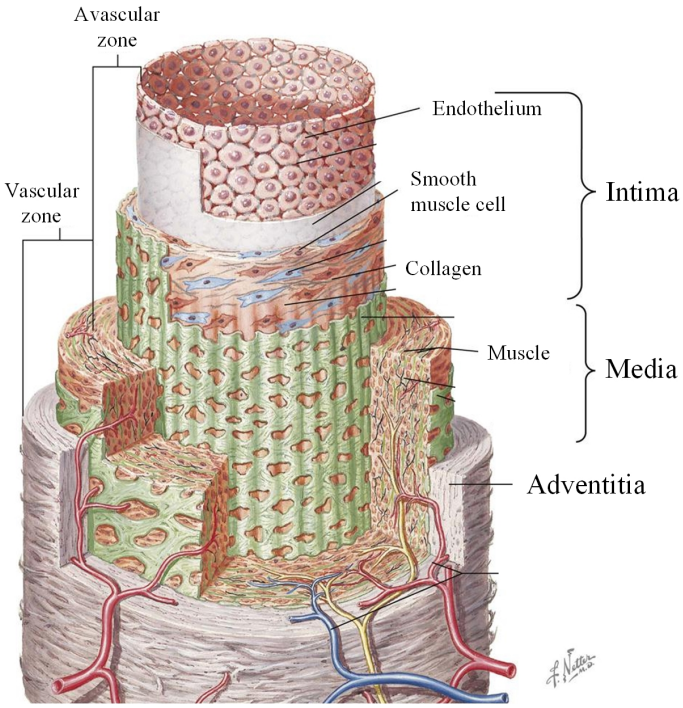

Figure 2.1 Structure of the wall of an artery (figure adapted from Conti [52])

nary and peripheral arterial diseases are usually caused by atherosclerosis [88]. The principal risk factors of atherosclerosis are age, gender, genetics, hypercholesterolemia (high level of lipids in blood), hypertension, cigarette smoking and diabetes [100]. Atherosclerosis is a very complex, multi-factorial and progressive disease that is the result from a cascade of multiple events [29]. Luminal narrowing of the vessel can compromise blood supply to downstream tissues, which may lead to ischemic injury. Also, during atherosclerosis plaque progression, thrombus may form, detach and create emboli which has a similar detrimental effect downstream. As the plaque progresses, vessel narrowing increases over an extended amount of time and can ultimately completely block the vessel, leading to a chronic total occlusion.

Figure 2.2 attempts to illustrate the atherosclerosis development. The next paragraphs describe its main processes and are based the following literature [29, 100, 158, 207]. Atherosclerosis is typically initiated by an injury or dysfunction of the endothelial cells. This can be caused by different factors like, but not limited to, hemodynamic disturbance, hypercholesterolemia or toxins from cigarette smoke present in the blood. Endothelium dysfunction/injury allows lipoprotein, mainly low-density lipoprotein (LDL), to migrate and accumulate inside the vessel. Also, dysfunction/injury of the endothelium allows for circulating monocytes to adhere to the vessel wall and migrate within the vessel structure. Once inside the intima, monocytes differentiate into macrophage. These macrophages then

engulfed and oxidized the LDL. Foam cells are resulting from this cascade of events and contribute to sustain this cycle via the recruitment of various cell types. These dynamic processes and the dysfunctional endothelial cells also promote inflammation and smooth muscle cells proliferation which participate also to sustain the atherosclerosis progression. SMC and foam cells can aggregate to form a fibrous collagen cap over the atherosclerosis plaque. Within the plaque, lipid pools accumulate and necrotic cores are formed resulting from cellular death. During progression, the plaque may rupture inside the vessel and a thrombus may form at its surface. Vascular calcification (VC) can also result from the atherosclerosis process and form within the plaque [192]. Risk of finding VC increases with age, chronic kidney disease and diabetes [130]. Process of VC formation is not that well understood. Contemporary research suggests that VC development shares similarity with bone formation [23, 38]. VC represents an accumulation of dense calcium phosphate within the vessel and can usually be observed by fluoroscopy, ultrasound and other type of imaging [126]. It was found that VC can accumulate within the vessel wall (medial calcification) and even protrude within the intima and into the lumen (intimal calcification) [7, 29, 58, 155]. Medial calcification, also called Mönckeberg calcification, forms circumferential sheet of calcium crystal. Intimal calcification is found in the form of small mineral deposits (calcified nodules) that can coalesce to produce larger solid crystals [146]. It is believed that the vascular calcification pattern and presence can vary across vascular regions. For example, VC content was reported to vary relative to the CTO location in the peripheral arteries; distal CTOs were more calcified then proximal ones [34]. In the coronary, calcified nodules are typically found in the middle right coronary or the left anterior descending arteries [211].

In angiography, CTOs are characterized by an absence of contrast flow (see figure 2.3). During angiography, contrast fluid is injected and artery outlines can be observed with fluoroscopy (X-ray) imaging. When a CTO is present, contrast cannot flow and blood is deviated via proximal side branches. CTOs are defined as totally occluded arterial segments that have remained occluded for an extended period (i.e. greater than 3 months) [12, 183]. CTOs are primarily composed of a heterogeneous mix of calcium, fibrosis, thrombus, lipid deposits and necrotic core [178]. The general composition of a CTO formed in the coronary or in the peripheral arteries is similar. However, the arrangement of the different CTO components can largely vary from lesion to lesion. Depending on the vascular bed, the CTO length is also different. Coronary arteries, which have usually smaller caliber and are more tortuous vessels, tend to have shorter CTO length, averaging at about 37 mm (N=482) [48]. In comparison, peripheral arteries are usually larger and straighter, and

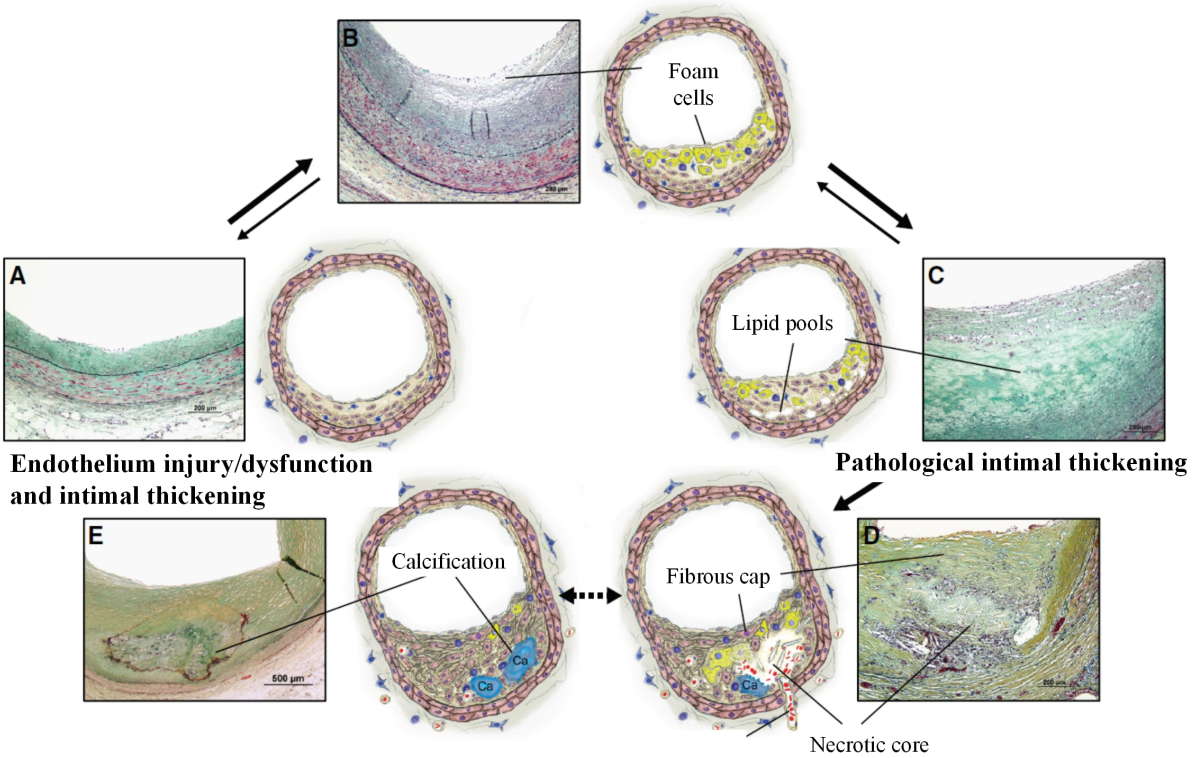

Figure 2.2 Summary of atherosclerosis progression (figure adapted from Bentzon *et al.* [29])

have CTO length averaging at about 165 mm (N=1092), with maximal length reaching over 400 mm [18].

Figure 2.4 shows examples of histology cross-sections from different CTOs. Panel (a) shows a CTO from a coronary artery composed of a thrombus (Thr), a necrotic core (NC) and calcifications (black arrows) [158]. This CTO is characterized by the almost total absence of a fibrous cap. The medial wall is also almost completely destroyed. Panel (b) shows a coronary CTO cross-section stained with hematoxylin-eosin. This CTO is characterized by the presence of extensive calcification (black arrow). Panel (c) shows a coronary CTO cross-section stained with elastic van Gieson. This CTO is characterized by the presence of lipid pools and extensive cholesterol deposition (black arrow).

Once an arterial circulatory problem is diagnosed and depending of the patient symptoms, different treatment options are available. When the patient is asymptomatic, lifestyle improvement and medical therapy are usually sufficient. When the patient is symptomatic, for example angina (chest pain) or with critical limb ischemia, percutaneous transluminal angioplasty (PTA), bypass graft surgery or medical therapy can be used as treatment options [22, 97, 101, 191].

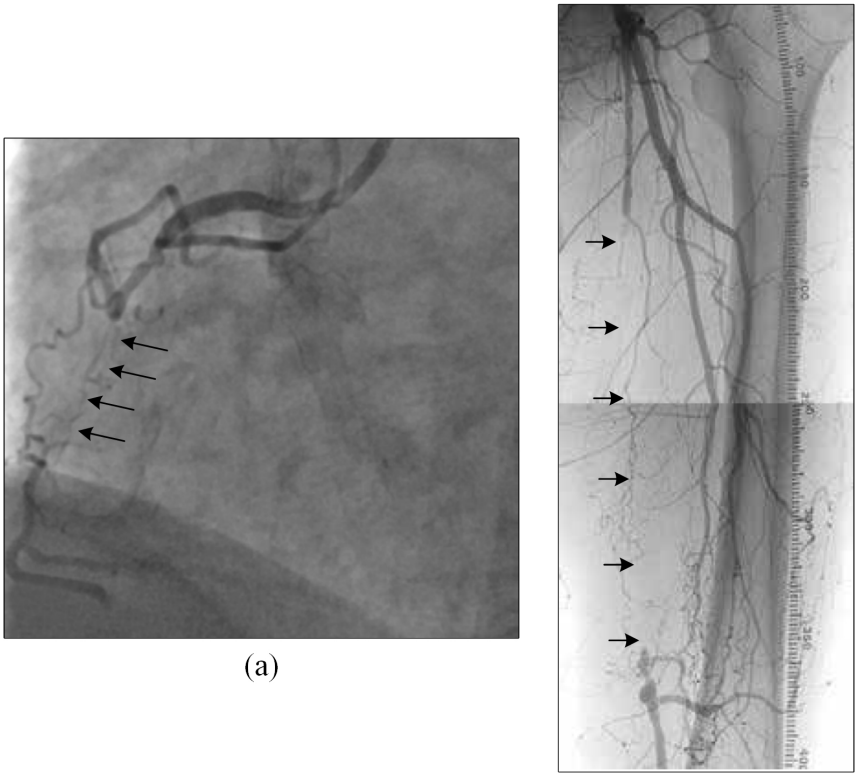

(a) (b)

Figure 2.3 Chronic total occlusion as observed angiographically (black arrows show CTO location). Panel (a) and panel (b) respectively show a lack of contrast flow in the mid-right coronary artery and in the superficial femoral artery (figure adapted from Benko *et al.* [28], Opolski and Achenbach [136])

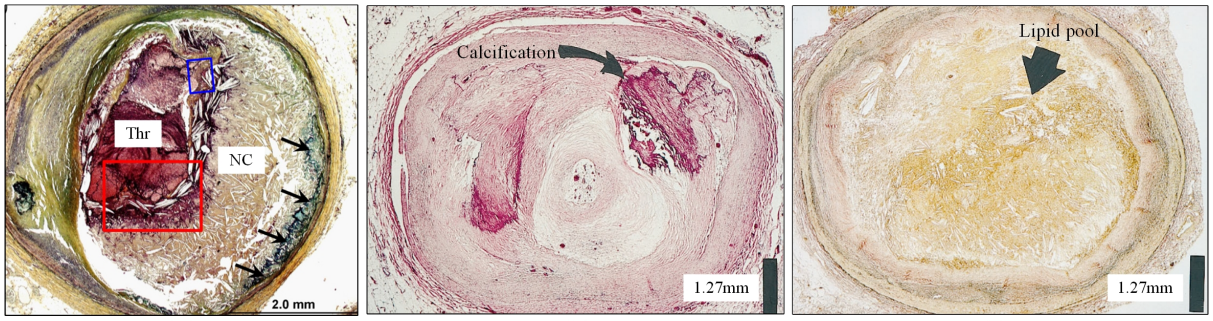

(a) (b) (c)

Figure 2.4 Histology cross-section from various CTOs (figures adapted from Srivatsa *et al.* [178] and Sakakura *et al.* [158])

PTA is a minimally invasive intervention in which different tools are inserted within the vasculature to recanalize the diseased vessel (i.e. partially or totally occluded artery). In a PTA procedure, the tools (guidewires, catheters) are inserted via an access site that is most commonly created in the femoral artery. Alternatively, the radial artery

(wrist) can be used for coronary CTO and a pedal access (foot) can be used for peripheral CTO. PTA interventions are similar between coronary and peripheral. A coronary PTA procedure is typically referred as a percutaneous coronary intervention (PCI). Once the access site is created, a floppy and atraumatic guidewire is inserted through the circulation and advanced near the target site. Then, an introducer sheath is advanced over the guidewire. The introducer is usually short and is used to maintain the access site open. The introducer has a luer connection with a valve from which fluid and contrast and can be injected to the blood stream. Over the floppy guidewire and through the introducer, a guide (or diagnostic) catheter is loaded. Guide catheters are typically 5 to 7 Fr [1] in size. Guide catheters are mostly used in PCI procedure. Their function is to provide support, facilitate delivery of other equipment and for selective contrast injection within the coronary arteries. Typically, introducer sheaths and guide catheters are not replaced during a procedure. A support catheter is then advanced, within the introducer sheath or guide catheter and over the guidewire. The floppy and atraumatic guidewire is exchanged for a workhorse guidewire that will be used to navigate in the arteries and to reach the lesion. For CTOs, various techniques and multiple devices can be used depending on its location, length, cap morphology, tortuosity, calcification level and presence of side branches. Also, support catheters and guidewires can be exchanged multiple times during a procedure. The objective is to position a guidewire or support catheter across the CTO and in the distal true lumen. Sometimes, crossing can be achieved within the intraluminal space (i.e. through the CTO), while other times, it is achieved via the subintimal space (i.e. through the layers of the arterial wall). When within the subintimal space, special techniques and devices may be needed to re-enter into the true lumen. Once the CTO is crossed, specialty debulking devices may be used to remove atherosclerotic plaque material. This is done to increase the residual lumen and to prepare the lesion for the next steps of the procedure. This specific process is called atherectomy. Following CTO crossing and atherectomy (when applicable), conventional balloons, drug coated balloons (DCB), bare metal stents (BMS), drug-eluting stents (DES), or combination of these devices are used to dilate and maintain the artery open. Procedure-related complications include perforation, distal embolization and dissection of the vessel wall. Reocclusion of the disease vessel may also happen days or months following the procedure and is referred to restenosis.

Figure 2.5 summarizes the steps in a typical PTA procedure. In this example, the diseased vessel is first crossed with a guidewire. Then, a stent, pre-mounted over a deflated balloon catheter, is brought over the guidewire and advanced across the lesion. The balloon is inflated and the stent is expanded. The size and length of the stent should be carefully

1. Size of guide catheter is defined in Fr unit, where 3 Fr equals 1 mm.

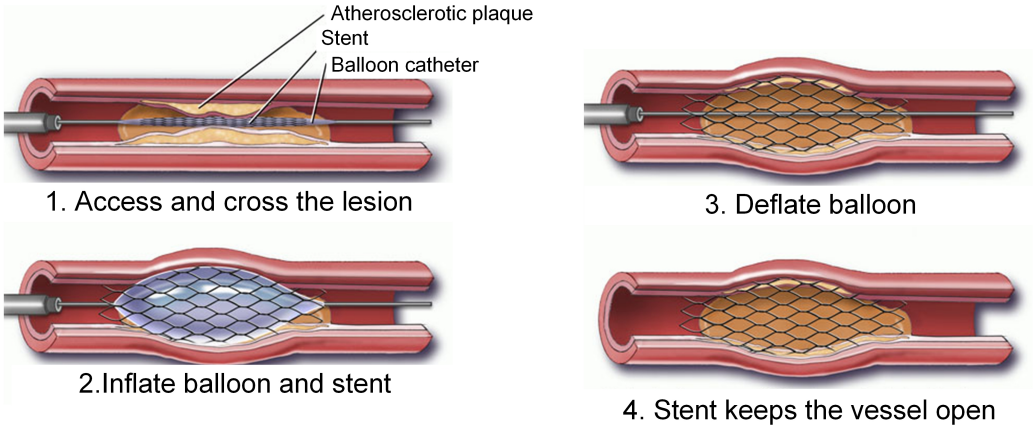

Figure 2.5 Example of a percutaneous transluminal angioplasty (PTA) procedure (figure adapted from [184])

selected to cover the whole lesion, and not more. The balloon is deflated and the equipment is removed from the patient, leaving the stent in place and the vessel open.

2.2 Techniques and devices for CTO crossing

Multiple CTO crossing techniques, using conventional equipment like guidewires and support catheters, were developed over the last few years [16, 56, 108, 196]. These techniques were mostly developed by high-skilled operators in the coronary space and are slowly adopted by peripheral interventionists. For example, both antegrade (direction of the blood flow) and retrograde (starting from the distal end and progressing toward the proximal end of the CTO) approaches are used to attempt CTO crossing. The retrograde approach is done through collateral arteries that naturally bypassed the CTO or using an alternative access site (e.g. pedal access in a peripheral procedure). Techniques like wire escalation/de-escalation, dissection/reentry and knuckle wire are also part of the operator new skill set. As previously described, the new hybrid-algorithm is more and more used by PCI operators to better plan and execute CTO crossing [42]. Such an algorithm in the peripheral space is yet to be developed [16].

Typical guidewire constructions are illustrated on figure 2.6. Guidewires are characterized by their core material, grind profile, coating(s), radiopaque marker configuration and tip profile. Each guidewire is designed to achieve a unique set of specifications (e.g. support, flexibility, penetration, lubricity, tip load, torque response, etc.) that are required by its specific use. The two most common core wire material are stainless steel 304V and Nitinol (nickel-titanium alloy) [45, 204]. The size of the guidewire depends on the principal vascular bed it is intended to be used. For example, coronary guidewires have generally

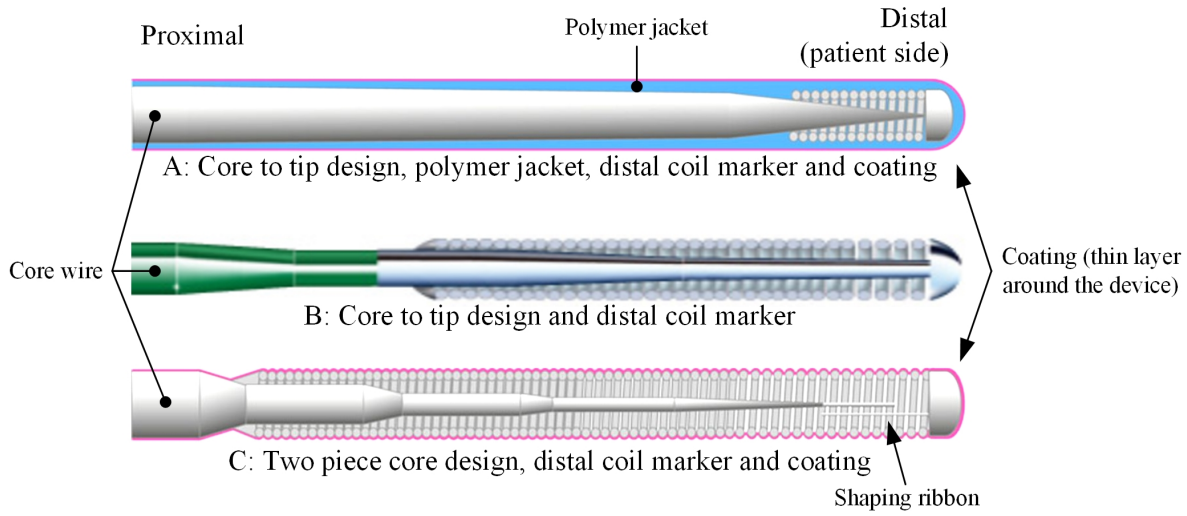

Figure 2.6 Illustration of typical guidewire constructions (not to scale) (figure adapted from Godino *et al.* [80])

an outer diameter of 0.36 mm (0.014") while peripheral guidewires have generally an outer diameter of 0.46 mm (0.018"). Two kinds of coatings can be used on commercial guidewires: (i) hydrophobic and (ii) hydrophilic. Hydrophobic coating repels water while hydrophilic absorbs water to create a hydro-gel layer [204]. Coatings are used to increase lubricity, better transmit torque, reduce thrombogenicity and improve tactile feedback [33, 45, 80]. However, it was suggested that coating may increase risk of perforation, but such thing was never clearly demonstrated [6]. Another disadvantage of coatings is that they may separate (crack, peel, flake, shed, delaminate) from medical devices, releasing particles inside the blood circulation and potentially causes serious injuries to patients [72, 85]. In a safety alert posted in 2015, the Food and Drug Association (FDA) still believes that the benefits of coated devices outweigh the risks. However, the FDA provided a list of recommendations addressed to the health care providers using such devices [72]. A radiopaque marker is added over the core wire distal end to increase visibility under fluoroscopy. A typical radiopaque marker design is represented by a platinum coil that is slipped over the distal core wire and attached to it [80]. The tip geometry can vary from guidewire to guidewire to change its tip load (flexural rigidity), outer diameter tapering profile and size. As shown in figure 2.6, the core wire generally tapers down toward the distal end to increase flexibility. In some designs, the core wire does not extend to the distal tip, increasing even more its flexibility (bottom image of figure 2.6). Other designs have a polymer jacket covering the distal region to increase lubricity and provide a uniform outer surface (top image of figure 2.6).

In addition to conventional guidewires, multiple specialty CTO devices are currently available on the market. Current and in-development specialty CTO crossing devices are summarized in table 2.1 along with their manufacturer, indication and proposed mechanism of action. References to the manufacturer website and to associated scientific literature are also provided. The same devices are illustrated in figure 2.7. In some rare occasions, atherectomy devices can also be used to cross CTO (e.g. the Rotablator), but they are not listed here.

Table 2.1 Summary of specialty CTO crossing devices

Device	**Manufacturer**	**Indication**	**Mechanism of action**	**References**
CrossBoss	Boston Scientific	C	Rotational blunt dissection	[40, 206]
PlasmaWire*	RetroVascular	C	Radiofrequency ablation	[96]
Crosser	Bard Peripheral	C and P	Mechanical impact (high frequency) and cavitation	[179, 193] [21, 102, 213]
Excimer laser	Spectranetics	C and P	Photochemical ablation	[103, 168, 177]
FrontRunner	Cordis	C and P	Blunt dissection	[108, 171] [53, 137]
CiTop	Ovalum	C and P	Blunt dissection	[163]
WildCat	Avinger	P	Manual or assisted rotational drilling	[142]
Truepath	Boston Scientific	P	Assisted rotational drilling	[36, 37]
Viance	Covidien	P	Rotational blunt dissection	[169]
Ocelot	Avinger	P	Manual rotational drilling	[167]
Piculet*	Medinol	P	High-frequency hammering	[81]
DABRA	Ra Medical	P	Photochemical ablation	[73, 150]
Enabler-P	EndoCross	P	Assisted guidewire dissection	[212]

C = Coronary and
P = Peripheral
*Device is not currently commercialized in the United States

From the list of devices presented in table 2.1, the excimer laser from Spectranetics is the oldest technology, the PlasmaWire is still under research and the DABRA catheter just recently obtained commercial approval in the United States. From the list of specialty CTO crossing devices, these technologies, except the CiTop, PlasmaWire and the Truepath, are considered catheter based devices. The CrossBoss and Viance catheters were originally developed by Bridgepoint who sold the two devices to two different companies. Their mechanisms of action are the same, but their indications are different. Both catheters

(a) CrossBoss and Viance catheter

(b) Spectranetics laser catheter

(c) PlasmaWire

(d) FrontRunner

(e) Crosser catheter

(f) Truepath

(g) WildCat and Ocelot catheter

(h) DABRA catheter

(i) Piculet vibrating catheter

(j) Enabler-P balloon catheter

Figure 2.7 Specialty CTO crossing devices: a. Viance/CrossBoss device (figure adapted from [206]); b. Spectranetics laser catheter (figure adapted from [177]); c. PlasmaWire (figure adapted from [96]); d. FrontRunner (figure adapted from [53]), e. Crosser catheter (figure adapted from [21]); f. Truepath (figure adapted from [37]); g. WildCat/Ocelot catheter (figure adapted from [142]); h. DABRA catheter (figure adapted from [150]); i. Piculet (figure adapted from [197]); j. Enabler-P (figure adapted from [54])

have an oversized blunt distal tip that can rotate when the proximal handle is spun. The Spectranetics laser catheter is composed of many optical fibers running the length of the catheter and are exposed at the distal tip. The DABRA laser catheter is similar to the Spectranetics laser, but rather uses a catheter filled with a fluid to transmit light. While the Spectranetics laser is an over-the-wire device, the DABRA laser catheter has no lumen and cannot be maneuver. The PlasmaWire technology facilitates CTO crossing via radiofrequency (RF) ablation. Interestingly, this system is used by inserting two PlasmaWires in the CTO. Each PlasmaWire has an electrode at its distal tip. When their distal tip is positioned next to each other, short (200 μs) square-wave pulses are delivered to the wire tips at a frequency of 250 kHz. Emission of these pulses is synchronized with the cardiac cycle. Delivery of RF energy continues for up to 5 s or until the creation of a channel. The FrontRunner has blunt jaws at its distal tip that can be controlled by a proximal handle and works by creating micro-dissection to channel through the CTO. The Crosser is a high-power low-frequency ultrasonic catheter device that is meant to create mechanical impact and cavitation to facilitate CTO crossing. The Crosser has an ultrasonic wire inside a catheter that is brought to its resonance frequency by a stack of piezoelectric transducers positioned inside the proximal handle. This creates peak-to-peak distal tip displacement of about 20 μm at a frequency rate of about 20 kHz. Simultaneously, saline is injected through the catheter to avoid overheating and to facilitate cavitation. The Truepath is a miniature drill (0.46 mm outside diameter) that rotates at about 13000 rpm. The Truepath has a sharp distal tip that is diamond-powder coated to facilitate erosion. The WildCat and Ocelot catheters are similar with the exception that the Ocelot allows for optical coherence tomography (OCT) imaging. These devices can be used manually or with a handheld motorized unit. The distal tip is equipped with a spiral wedge that can rotate and bore a channel into the CTO. With the Ocelot, OCT can be used to guide the device to stay within the vessel walls. The Piculet catheter device vibrates at high frequency rate and hammers the CTO to create a channel. Alternatively, it can also grab the distal tip of a guidewire inside its lumen and make it vibrate as well. The Enabler-P technology has two main components: a specialized balloon catheter and a pressure control unit (PCU). First, the balloon is anchored in the lumen of the vessel to center the guidewire. The shape of the balloon is such that when it is inflated in a certain way, it grabs the inside guidewire and pushes it forward. This movement can be repeated by using the PCU to facilitate progression. The CiTop device is similar to a conventional guidewire with the difference that it has a deflectable tip controlled with a proximal handle. The deflectable tip can be used to enlarge the residual lumen while crossing or to facilitate finding microchannels.

Even considering the new CTO crossing techniques that were developed over the last few years and the variety of specialty CTO crossing devices, there still is an unmet need in the field of percutaneous CTO recanalization [84, 156, 161]. Indeed, the proposed crossing techniques are still recent and only adopted by a handful of skilled and experienced operators. Each specialty CTO crossing devices has its advantages and limitations. Most notable limitations of these devices are their size (too bulky catheter type), difficulty to use and their limited efficacy. Also, these devices and techniques are complex to use, which impacts the procedure workflow and time.

2.3 Theories of wave propagation in elastic solids

As it will be further described in section 4.1, the proposed system exploits mechanical waves that are generated, amplified and transmitted in solid structures to facilitate CTO crossing. The proposed technology takes advantage of various principles that are associated with the propagation of elastic waves in solids. For example, in the proposed system, small amplitude mechanical waves are spatially and temporally compressed in a solid waveguide to create a high amplitude wave at the opposite end. Also, wave attenuation is considered in the design process to allow for efficient transmission and delivery of the high amplitude mechanical wave at the end of the system in contact with the CTO. The following concepts associated with the propagation of mechanical waves in a solid are described in the next subsections along with their governing equations: wave propagation in an infinite medium, effect of boundary conditions, wave diffraction and directivity, wave focalization, dispersion, attenuation and nonlinearity.

2.3.1 Wave equation in an infinite medium

Two kinds of wave can travel in an infinite elastic solid. These waves are referred as dilatation and distortion waves [83]. Dilatation waves are waves caused by volume change and are associated with longitudinal (or compression) waves. Distortion (or rotational) waves are waves involving no dilatation and are associated with transverse (or shear) waves. Both wave types can exist independently and propagate at their own velocity. Conceptually, one way to understand the difference is by referring to the slinky experiment shown on figure 2.8. Longitudinal waves are created by compressing or expending the length of the slinky (panel a of figure 2.8). Transverse waves are created by moving the slinky sideways relative to its central axis (panel b of figure 2.8).

The following describe how to derive the wave equation and is largely based on the textbook of Kolsky [99]. The governing equation of wave motions in a solid is referred as the wave

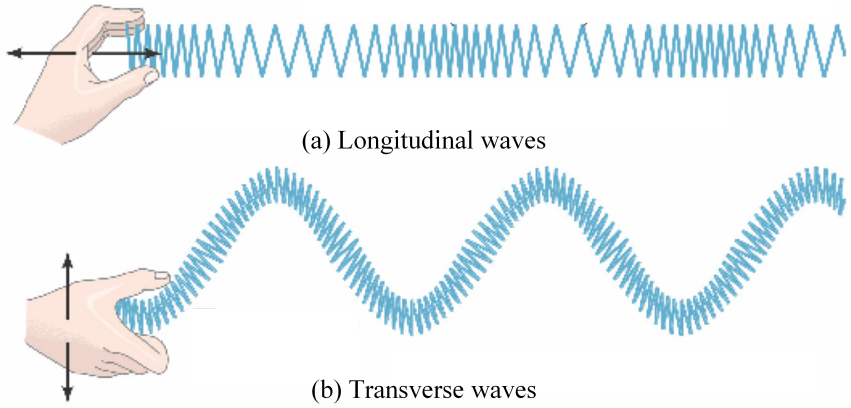

Figure 2.8 Representation of longitudinal and transverse waves (figure adapted from [79])

equation. This equation is obtained by derivation of the Hooke's law, Newton's second law and the strain matrix for a minuscule element from an infinite (unbounded) and perfectly elastic solid. Such element is shown on figure 2.9. On the left side of figure 2.9, the element is initially at rest and on the right, the same element is shown a short time after being disturbed. On the left side, the equilibrium stress components σ_{ij} are shown on the three main faces, where i corresponds to the direction of the stress and j corresponds to the plane in which it is applied. Displacement of any points from the infinitesimal element of figure 2.9 can be described by its cartesian components u, v and w. An example of that is provided for a single point in figure 2.9. In the more general case, the relative displacement of all points can be evaluated to obtain the associated compression/expansion strains, shear strains and rigid body rotations. Their associated equations are shown in relation 2.1. The compression/expansion strains of the infinitesimal element in the three directions are identified as ϵ_{xx}, ϵ_{yy} and ϵ_{zz}, the shear strains are labeled ϵ_{yz}, ϵ_{zx} and ϵ_{xy}, and the rigid body rotations are labeled $\bar{\omega}_x$, $\bar{\omega}_y$ and $\bar{\omega}_z$. For small displacements, the rotations are equivalent to the shear strains.

$$\begin{aligned}
\epsilon_{xx} &= \frac{\partial u}{\partial x}, & \epsilon_{yy} &= \frac{\partial v}{\partial y}, & \epsilon_{zz} &= \frac{\partial w}{\partial z} \\
\epsilon_{yz} &= \frac{\partial w}{\partial y} + \frac{\partial v}{\partial z}, & \epsilon_{zx} &= \frac{\partial u}{\partial z} + \frac{\partial w}{\partial x}, & \epsilon_{xy} &= \frac{\partial v}{\partial x} + \frac{\partial u}{\partial y} \\
2\bar{\omega}_x &= \frac{\partial w}{\partial y} - \frac{\partial v}{\partial z}, & 2\bar{\omega}_y &= \frac{\partial u}{\partial z} - \frac{\partial w}{\partial x}, & 2\bar{\omega}_z &= \frac{\partial v}{\partial x} - \frac{\partial u}{\partial y}
\end{aligned} \tag{2.1}$$

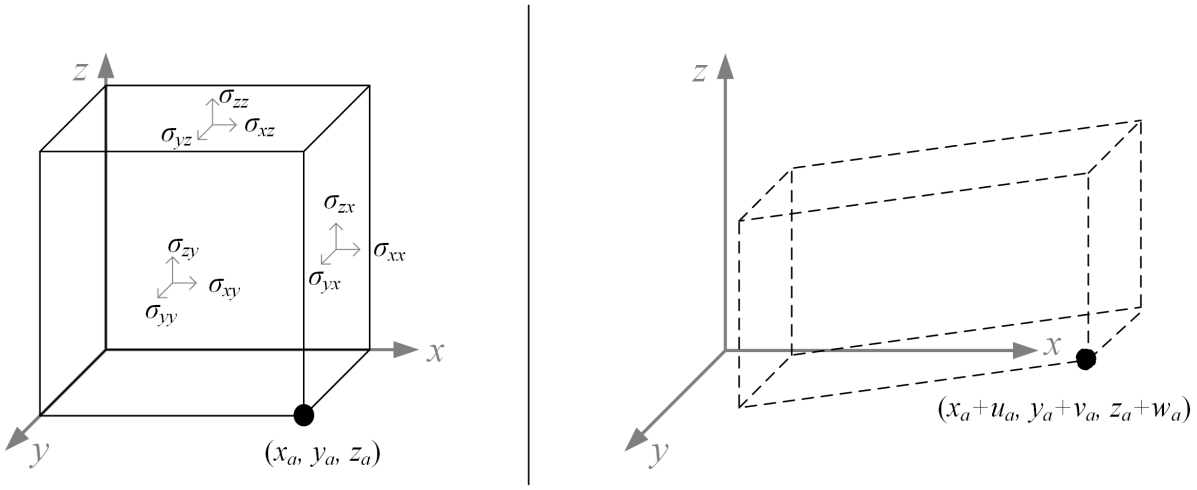

Figure 2.9 Infinitesimal element from an isotropic solid before (solid line) and a short time (dotted line) after being disturbed

The elastic solid from which this infinitesimal element was selected is assumed to be isotropic (i.e. the properties of the medium do not depend on the direction). The elastic properties of this solid can be expressed by its Lamé's constants λ_a and μ_a. However, the Young's Modulus (E), Shear Modulus (G) and Poisson ratio (ν) are most commonly used in engineering to characterize the elastic properties of a solid. The Young's Modulus and the Poisson ratio can be associated with the Lamé's constants from equations 2.2 and 2.3 respectively, while the Shear Modulus is directly related to μ_a. For reference, Table 2.2, presented at the end of this chapter, summarizes the properties of different materials.

$$E = \frac{\mu_a(3\lambda_a + 2\mu_a)}{\lambda_a + \mu_a} \tag{2.2}$$

$$\nu = \frac{\lambda_a}{2(\lambda_a + \mu_a)} \tag{2.3}$$

The Hooke's law states that for a solid, strain is proportional to the applied load, as long as this load is small enough to avoid plastic deformation and that the system is linear [105]. The general form of the Hooke's law is presented by equation 2.4, where σ corresponds to the stress, ϵ corresponds to the strain and k_{xy} is a constant. For the isotropic and infinitesimal element of figure 2.9, the Hooke's law can be rewritten by equation 2.5, where the Lamé's constants are used and the dilatation Δ (volume change) is equal to $\epsilon_{xx} + \epsilon_{yy} + \epsilon_{zz}$.

$$\sigma = k_{xy}\epsilon \tag{2.4}$$

$$\begin{aligned} \sigma_{xx} = \lambda_a\Delta + 2\mu_a\epsilon_{xx}, \quad \sigma_{yy} &= \lambda_a\Delta + 2\mu_a\epsilon_{yy}, \quad \sigma_{zz} = \lambda_a\Delta + 2\mu_a\epsilon_{zz} \\ \sigma_{yz} = \mu_a\epsilon_{yz}, \quad \sigma_{zx} &= \mu_a\epsilon_{zx}, \quad \sigma_{xy} = \mu_a\epsilon_{xy} \end{aligned} \tag{2.5}$$

Newton's second law defines that the sum of forces is equal to the change in momentum over time. This can be translated by general equation 2.6, where F corresponds to the sum of forces applied to a body, m is its mass and a is the acceleration of the same body. Note that this equation is typically expressed in a vector form. The left side of equation 2.6 is obtained by calculating the force balance in each direction of the infinitesimal element of figure 2.9. The force acting on each face is given by the product of the stress and its corresponding surface area. In this example, body forces are not taken into consideration. The right side of equation 2.6 is obtained by the product of the element density ρ, its volume and the second partial derivative of its displacement relative to time t. The resulting simplified equations are presented by relation 2.7 for each direction.

$$F = m * a \tag{2.6}$$

$$\begin{aligned} \rho\frac{\partial^2 u}{\partial t^2} &= \frac{\partial\sigma_{xx}}{\partial x} + \frac{\partial\sigma_{xy}}{\partial y} + \frac{\partial\sigma_{xz}}{\partial z} \\ \rho\frac{\partial^2 v}{\partial t^2} &= \frac{\partial\sigma_{yx}}{\partial x} + \frac{\partial\sigma_{yy}}{\partial y} + \frac{\partial\sigma_{yz}}{\partial z} \\ \rho\frac{\partial^2 w}{\partial t^2} &= \frac{\partial\sigma_{zx}}{\partial x} + \frac{\partial\sigma_{zy}}{\partial y} + \frac{\partial\sigma_{zz}}{\partial z} \end{aligned} \tag{2.7}$$

The general wave equation is obtained by combining equations 2.1, 2.5 and 2.7, and is represented by relation 2.8. In this equation, the Laplace operator ∇^2 is described by relation 2.9. The wave equation can be further simplified to obtain the dilatation and distortion wave equations. The former is presented in equation 2.10, where the wave velocity c_l was introduced and is equal to $\sqrt{(\lambda_a + 2\mu_a)/\rho}$. The latter is presented in equation 2.11, where the wave velocity c_s was introduced and is equal to $\sqrt{\mu_a/\rho}$. In

equation 2.11, $\bar{\omega}_x$ correspond to the rotation of the element along the x axis. Similar equations can be found for $\bar{\omega}_y$ and $\bar{\omega}_z$. For reference, table 2.2, presented at the end of this chapter, summarizes the different wave velocities of various materials.

$$\rho\frac{\partial^2 u}{\partial t^2} = (\lambda_a + \mu_a)\frac{\partial \Delta}{\partial x} + \mu_a \nabla^2 u \tag{2.8}$$

$$\nabla^2 = \frac{\partial^2}{\partial x^2} + \frac{\partial^2}{\partial y^2} + \frac{\partial^2}{\partial z^2} \tag{2.9}$$

$$\frac{\partial^2 \Delta}{\partial t^2} = {c_l}^2 \nabla^2 \Delta \tag{2.10}$$

$$\frac{\partial^2 \bar{\omega}_x}{\partial t^2} = {c_s}^2 \nabla^2 \bar{\omega}_x \tag{2.11}$$

The wave equation represents a second order partial differential equation. Analytical solutions for the wave equation can be found when considering the assumptions mentioned before [1]. Typical solution for the one-dimensional wave equation in the x direction has the form shown by equation 2.12, where u_1 and u_2 are arbitrary functions that can be derived twice and c is the wave velocity (can be c_l or c_s depending on the wave type identified by the problem) [1]. Arbitrary functions u_1 and u_2 are found using the initial conditions from the problem. It is seen from equation 2.12 that the solution shows a wave traveling in the $+x$ direction and another one traveling in the -x direction. In the special case of a harmonic wave and taking into consideration only one direction of propagation, one potential solution for equation 2.12 is given by equation 2.13. In the latter, A represents the amplitude of the wave, k is the wave number which and is equal to ω/c, ω is the circular frequency and is equal to $2\pi f$, and f is the frequency associated with the oscillation. Alternatively, the wavelength parameter $\lambda = c/f$ can also be used which is associated with the distance traveled by one cycle of the harmonic wave.

$$u(x,t) = u_1(x + ct) + u_2(x - ct) \tag{2.12}$$

$$u(x,t) = u_1(x + ct) = A\cos(kx + \omega t) \tag{2.13}$$

In summary, two types of waves can propagate in an unbounded, linear, isotropic and elastic solid. These are the dilatation (compression / longitudinal) and the distortion (shear / transverse) waves. These waves travel at different velocities that are directly associated with the elastic properties of the medium (Young's Modulus, Shear Modulus and Poisson ratio). The wave equation is found by combining the Hooke's law, Newton's second law and the associated strains from an infinitesimal element selected within the elastic medium. For simple problems, an analytical solution can be found for the wave equation knowing the initial conditions.

2.3.2 Boundary conditions

In certain real life conditions, the geometry of the body cannot be assumed infinite and one or more boundaries must be taken into consideration. Such boundary condition introduces the concept of a third wave, called the surface wave or Rayleigh wave, which propagates along the free surface of the body [127]. This wave type travels at its own velocity c_R and has the particularity that it rapidly decays along the depth of the medium. Surface wave velocity is equal to $\approx 0.93c_s$ for a solid medium having a Poisson coefficient of 0.3 [1]. Rayleigh waves can propagate on a plane or distorted surface. Also, since these waves travel along a surface, they are by nature two-dimensional and tend to attenuate less rapidly over the distance than dilatation and distortion waves that travel in three-dimensions.

Let's consider the special case of a circular rod of constant cross-section, infinite length, made from an isotropic, lossless and elastic solid, with a free surface in vacuum and where the wavelength is much larger than its radius. The wave equation associated to this special case can be derived following the same method described in subsection 2.3.1. Considering these assumptions and the longitudinal motion (x) only, the associated wave equation is presented by relation 2.14 [99]. The velocity c_0 at which a longitudinal wave is traveling in this waveguide is presented by equation 2.15. It should be noted that the longitudinal wave velocity c_0 in a rod is not equal to the longitudinal wave velocity c_l in an infinite elastic solid because of the newly introduced boundary conditions.

$$\rho\frac{\partial^2 u}{\partial t^2} = E\frac{\partial^2 u}{\partial x^2} \tag{2.14}$$

$$c_0 = \sqrt{\frac{E}{\rho}} \tag{2.15}$$

When a medium is bounded, the notion of wave reflection at an interface must be established. Depending on the nature of the surrounding medium, the wave can also be partially transmitted in this new medium. The amplitude and direction of the reflected and transmitted waves are solved knowing the incident wave characteristics and by satisfying the boundary conditions (equal displacements and stresses at both sides of the interface). By solving the associated wave and boundary condition equations, it is found that the amplitude of the reflected and transmission waves is function of the relative acoustic impedance of each medium. The acoustic impedance is defined as the pressure to velocity ratio of a propagating wave. In the case of a plane harmonic wave propagating in a solid, the acoustic impedance Z is referred as the specific acoustic impedance and is defined by the medium properties (density ρ and wave velocity c) [127]. The specific acoustic impedance is shown in equation 2.16 [99]. The acoustic impedance refers to the resistance of a wave to propagate and is analogue to an electrical resistance which restrict the amount of current that can flow through it [83]. For reference, table 2.2, presented at the end of this chapter, summarizes the specific acoustic impedance of various materials.

$$Z = \rho * c \tag{2.16}$$

Consider the special case in which a plane one-dimensional harmonic dilatation wave is traveling from a semi-infinite medium 1 bounded by a semi-infinite medium 2. The plane interface between these two media is perfect and perpendicular to the direction of propagation of the wave. When satisfying the boundary conditions between the two media, it is found that the resulting amplitude of the reflected and transmitted waves are given by the reflection r and transmission t coefficients defined in equation 2.17 [165]. When medium 1 is a solid and medium 2 is air, it can be considered that $Z_2 \ll Z_1$ and that the wave will be totally reflected in medium 1 (r = -1 and $t = 0$). It is noticed that the sign in front of the reflection coefficient is negative. It should also be considered that the reflected wave is propagating in the reversed direction relative to the incident wave. Therefore, the two signs canceled each other.

$$r = \frac{Z_2 - Z_1}{Z_2 + Z_1}, \qquad t = \frac{2Z_2}{Z_2 + Z_1} \tag{2.17}$$

Now consider another special case where semi-infinite medium 1 has a free interface (bounded by vacuum). Let also suppose that the angle of incidence between the direction of propagation of the dilatation wave and the interface is not perpendicular. In such case,

two wave types are reflected within medium 1 to satisfy the boundary conditions; one is a dilatation wave and the other is a distortion wave. By analogy, the same principle can be applied to an incident distortion wave or an incident wave combining dilation and distortion waves. This process is also referred as mode conversion as one wave type is transformed into two wave types.

Figure 2.10 shows a more complicated case where the incident plane wave is not perpendicular to the plan interface and where the two media are different than vacuum [99, 165]. In this example, the dilatation wave A_i reaches the interface at an incident angle α_i, is reflected into a dilatation wave A_r at an angle α_r and into a distortion wave B_r at an angle β_r. Similarly, wave A_i is transmitted (also called refraction) in medium 2 into a dilatation wave A_t at an angle α_t and into a distortion wave B_t at an angle β_t. The angles of transmission and reflection can be found using the Snell law with the different wave velocities. The relative amplitudes can be found using equations similar to relation 2.17, but derived for a two-dimensional problem. It is understood that there exist special conditions (medium properties and angle of incident) for which waves will not be transmitted into medium 2 or that will be transmitted along the interface between the two media.

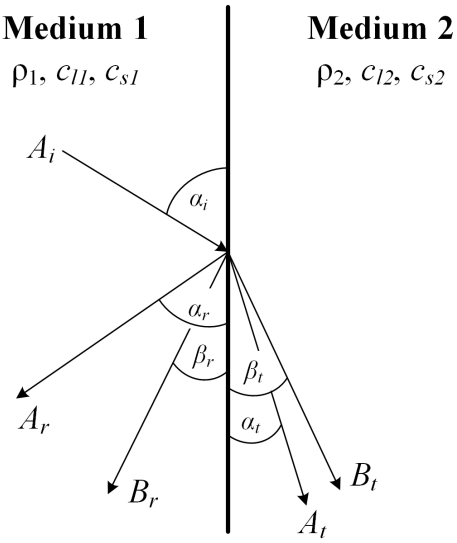

Figure 2.10 Reflection and transmission of an incident plan wave at a plane interface

In summary, when deviating from an infinite medium and considering a bounded medium, a third wave type called the surface wave is introduced. It was shown that a longitudinal wave traveling in an infinitely long rod with no lateral displacement will propagate at a wave velocity c_0 different than the dilatation and distortion wave velocities in an infinite solid. The concept of specific acoustic impedance and the notion of reflection and

transmission at the interface between two media were described. Mode conversion was discussed. It was shown that the angle of incidence, the nature of the wave and the properties of the media can impact the resulting reflected and transmitted waves.

2.3.3 Diffraction and directivity

In the proposed CTO crossing system, mechanical waves are generated at the surface of an elastic solid medium by piezoelectric transducers of finite size. The characteristics of the emitted waveform, the size of the transducer and the medium properties all effect how the waves are propagating inside the elastic solid. The concepts of diffraction and directivity are presented to understand how the resulting waves are propagating inside a solid medium.

In the field of non-destructive testing, it is common to divide the field of wave propagation in front of the transducer in two distinct regions: (i) near field and (ii) far field. This is illustrated by figure 2.11, where a transducer and the resulting wave amplitude pattern along the central axis and the transducer's cross-section are shown. In the near field, the multiple wave interference and interactions make it difficult to evaluate the wave amplitude. However, in the far field, the wave propagation is more uniform and its amplitude usually decays as it travels away from the source. For a circular and harmonic source, the near/far field transition N occurs at the distance provided in equation 2.18, where λ is the wavelength and r is the radius of the source [165]. For a source having a radius of 25.4 mm, emitting a waveform having a centered frequency of 450 kHz in an elastic medium having longitudinal wave velocity of 6100 m/s, the distance N is equal to 47.6 mm.

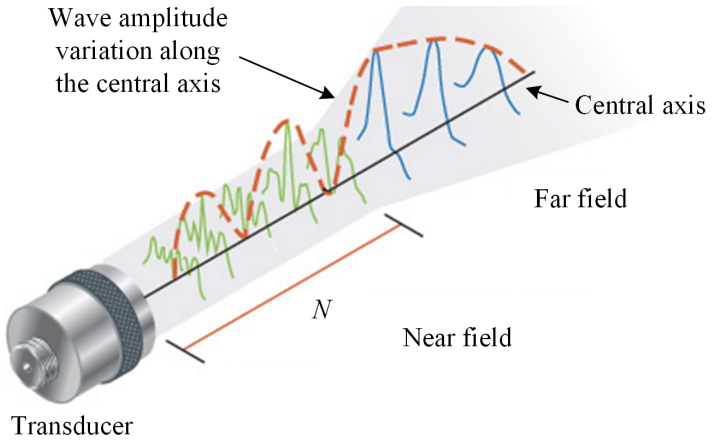

Figure 2.11 Example of a circular transducer with its near and far field representation (figure adapted from [134])

$$N = \frac{r^2}{\lambda} \tag{2.18}$$

Directivity of the ultrasonic beam resulting from the emission of a transducer is typically provided in the far field region only. Directivity of a circular transducer in a specific medium is function of the wavelength and radius of the source. Figure 2.12 shows an example of such radiation patterns, given in the form of a polar plot, in term of displacement in the radial direction only. In this example, a circular source of radius 0.7 cm is emitting compressional stress waves in a semi-infinite elastic medium having a longitudinal velocity of 6400 m/s and a shear wave velocity of 3100 m/s [189]. The radiation pattern is assumed symmetrical around its longitudinal axis. Each curve corresponds to a different r/λ ratio. As observed on figure 2.12, smaller r/λ ratios result in a beam that is less directive with more spreading in space. Alternatively, larger r/λ ratios result in a very directive beam with all the energy concentrated in front of source. Notice that at lower r/λ, the source is almost a point-source with a wave front radiating spherically. As an example, a source of radius 25.4 mm, emitting a waveform having a centered frequency of 450 kHz in an elastic medium having a longitudinal wave velocity of 6100 m/s, the corresponding r/λ is 1.87.

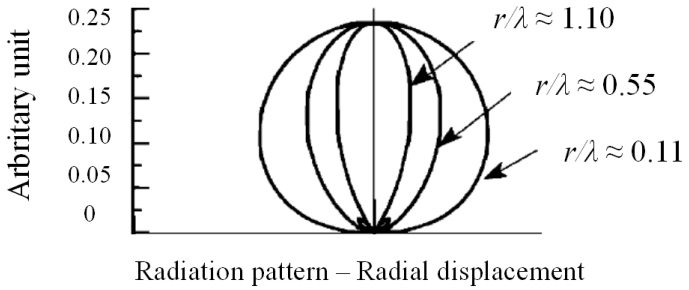

Figure 2.12 Polar plot showing directivity patterns associated with a circular source emitting in a semi-infinite elastic solid as function of the r/λ ratio (figure adapted from Tang *et al.* [189])

A more realistic example is presented in figure 2.13, where a circular source is in contact with the free surface of a semi-infinite elastic medium. Let assume that the source is a transducer, that it can only emit compressional stress waves normal to the free surface of the medium and that the emission surface is uniform. Figure 2.13 shows an example of the wave propagation pattern at four different time intervals [91]. In this example, the r/λ ratio is about 2. Therefore, the source is assumed to be directional. These results were obtained from simulating the propagation of a short duration pulse. Results are supposed to show the distribution of the displacement vectors (direction and magnitude), but the scale of the image doesn't allow for visualization of the vectors. Still, it is interesting to note

the presence of different wavefronts traveling in the medium. The first one corresponds to the compression wave that is traveling at the longitudinal wave velocity. The second one, radiating from the transducer edge, corresponds to the shear wave front traveling at the shear wave velocity. As observed, such problem can become rapidly complex due to the geometry of the source, the type of waveform and the medium properties. In this example, the compressional wave emission results in the propagation of compression and shear waves in the semi-infinite medium. Amplitude of these waves varies according the distance from the source and angular position relative to the transducer main axis. In addition, surface waves (not shown in the this example) can also be present and propagate along the free surface [83]. An analytical solution can be obtained for simple problem where the source is considered harmonic and where the solution is evaluated in the far field only. More complex problems are usually solved using finite element analysis.

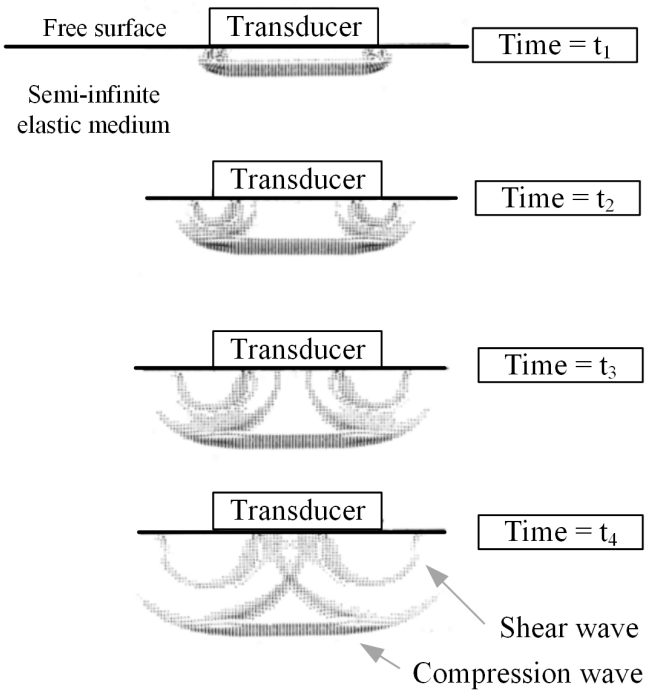

Figure 2.13 Example of a circular transducer emitting in an semi-infinite elastic medium (figure adapted from Ilan and Weight [91])

In summary, it was described that wave propagation analysis is usually performed in the far field where the wave amplitude decays as the wave is moving away from the source. The directivity pattern of a circular source emitting compressional waves in an elastic solid was also presented for different r/λ ratios. It was shown that the higher the r/λ ratio is, the more directive the source is. Lastly, it was showed that multiple propagating waves can result from the emission of a compressional transducer positioned at the surface of a

semi-infinite elastic solid.

2.3.4 Wave focalization

In the proposed CTO crossing system, different methods were used to increase the amplitude of the waves as they are traveling in a solid medium. One of these methods consists to use of a spatial concentrator to combine the emitted waves from multiple discrete piezoelectric transducers. This subsection presents a summary of different methods that can be used to focalize waves in various media. The following presents a non-exhaustive list of such methods:

- Focalized transducer
- Acoustic lens
- Phased array
- Time reversal mirror
- Parabolic reflector mirror

A focalized transducer can be used for emission in a solid [39]. For this, the surface of the elastic solid shall have the same shape as the transducer and proper coupling should be obtained. For reference, the theoretical focalization gain G_f obtained from a focalized source in a fluid is described by equation 2.19, where r is the radius of the source, d is the geometrical focal length and λ is the wavelength [31, 114]. A fluid medium can be seen as a simplified case of a solid medium where only one wave type can travel. Indeed, a shear wave cannot usually travel in a fluid. It is sometimes useful to refer and learn from wave propagation theories in fluids and then extrapolate these in solids. Referring to equation 2.19, in theory and in perfect conditions, the maximal focalization gain G_f is achieved when the radius of the source is equal to its geometrical focus. This is achieved with a hemispherical transducer focusing at its center. Interestingly, the r/λ ratio appears in this equation, meaning that the directivity pattern of the source is also taken into consideration to achieve high focalization gain.

$$G_f = \frac{\pi r^2}{\lambda d} \tag{2.19}$$

An acoustic lens can be shaped between two different media. This acoustic lens takes advantage of the refraction principle, described in section 2.3.2, to focus an incident plane wave into the transmitted medium. This method is derived from the field of optics. The refraction index and Snell law can also be applied to wave propagation in solids.

A transducer in the form of a phased array can also be used [11]. Such transducer is composed of many emitting elements that can be driven independently. By changing the relative phase between each element, a spherical wave front can be generated and focus in the elastic solid. This method is already largely used in the field of non-destructive testing and in medical imaging with ultrasound, but it requires a precise control strategy to be optimal [164].

The time reversal principle can be used in combination with a reverberant elastic solid and one or more transducers attached to it [67, 125, 185]. This method was developed based on the principle that in a non-dissipative medium, the wave equation specifies that for every burst of wave diverging from a source, there exist a set of waves that can precisely retrace the path back to the source. As described by Puckett [147], the time reversal mirror experiment consists of three steps. First, the source emits a waveform into the medium. Waves are traveling down the medium and are altered by it (e.g. boundary conditions, heterogeneity, dispersion, etc.). The altered waves are recorded at the opposite end of the medium by the receiver. Second, the recorded waves are reversed in time. Third, the time reversed waves are emitted by the receiver. The time reversed waves travel back in the medium and are recorded by the source. If the system is perfect (i.e. without loss), the new waveform should be the same as the original one. This method has been demonstrated to be very robust and work even in heterogeneous and dissipative medium, but with some degradation in the reconstructed signals [67]. When the number of receivers is increased or when the time reversed signal is amplified before emission, wave focalization can be achieved [125].

Another way to focalize waves is by using a parabolic reflector mirror. Use of parabolic reflector for radio application was introduced in the early 20th century [203]. Parabolic antennas were already used in the field of optics to focus light. Nowadays, parabolic antennas are everywhere and are mainly used for the transmission of information using high frequency waves in air (electromagnetic waves). More recently, it was proposed to use a parabolic mirror to focalize waves traveling are the surface of an elastic solid in the context of energy harvesting [194]. Parabolic reflectors are also used in the field of extracorporeal shock wave lithotripsy by electromagnetic lithotripters [176]. In this system, an electromagnetic source (located outside the patient) is used to create a plane wave in water that is reflected by a parabolic mirror toward a focal point (within the patient) near the location of the kidney stone to break. Figure 2.14 shows a representation of an extracorporeal electromagnetic lithotripter system.

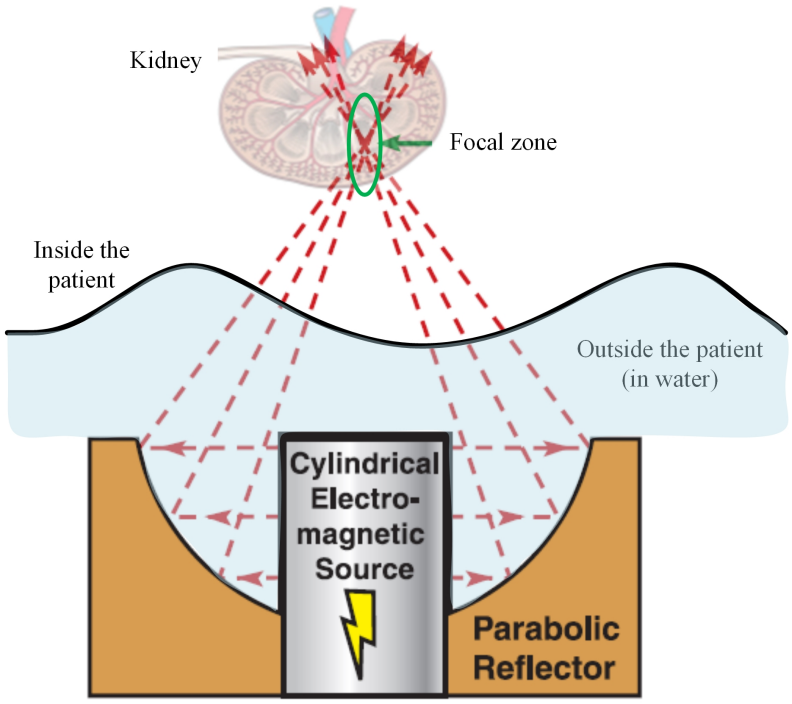

Figure 2.14 Illustration of an electromagnetic lithotripter and its parabolic reflector having its focal zone inside the patient (figure adapted from Smith [176])

In summary, different methods were described to focalize waves inside an elastic solid or a fluid. It is understood that more than one method can be combined to further improve the amplification factor.

2.3.5 Wave dispersion

Another mean used by the proposed CTO system to amplify mechanical waves is by exploiting the dispersion properties of a solid cylindrical rod along. When the conditions are such to allow dispersion, the velocity at which the wave travels is no longer constant and is now function of both the frequency and the mode of propagation. Dispersion can be attributed to the medium of propagation or the geometry of the structure in which the waves are traveling (commonly refers as a waveguide).

When dispersion is associated with the medium, one or more of its elastic properties vary over the distance of propagation and cause the signal to change shape. This can be observed in medium having a composite structure like cement-based materials [92]. When an acoustic signal is traveling in an elastic waveguide made from a non-dispersive material, geometrical dispersion may also be observed. This happens when the wavelength is within the same order as the thickness of the waveguide [99]. For example, a longitudinal wave

traveling in a cylindrical rod where the wavelength is similar to its diameter will generate lateral motion within the waveguide. This lateral motion creates a non-uniform stress distribution and the original waveform is distorted as it travels.

In ultrasonic non-destructive testing, dispersion is usually considered a detrimental effect of the measure as it can veil the effect of material attenuation and crack location in the medium. Work was performed in that field to find ways to compensate the effect of dispersion in a waveguide [147]. Other research work showed that waveguide dispersion can be used advantageously in combination with time reversal (refer to subsection 2.3.4) to amplify a specific waveform [59].

A more inclusive equation associated with the propagation of waves in an isotropic, infinite and elastic rod of constant radius in vacuum (free surface) was provided by Pochhammer and Chree. This equation, also called the frequency equation, is presented by relation 2.20 for the longitudinal modes. This equation is particularly important for solving problems where the wavelength of the signal has the same order as the lateral dimension of the waveguide. In equation 2.20, r is the rod radius, J_0 is the Bessel function of the first kind of order zero, J_1 is the Bessel function of the first kind of order one, k is the wave number, p is given by equation 2.21, q is given by equation 2.22. In these later equations, ω is the circular frequency, c_l is the longitudinal wave velocity and c_s is the shear wave velocity. Due to its complexity, this equation was only solved many years after it was first proposed with the help of numerical methods. The Pocchammer-Chree equation is valid for compressional, flexural and torsional waves. When solving the equation, it is observed that an infinite number of modes for each wave type can travel in a waveguide [202]. Each mode has a characteristic shape defined by its stress distribution along the radius of the waveguide.

$$\frac{2p}{r}(q^2+k^2)J_1(pa)J_1(qr) - (q^2+k^2)J_0(pr)J_1(qr) - 4k^2pqJ_1(pr)J_0(qr) = 0 \tag{2.20}$$

$$p^2 = \frac{\omega^2}{{c_l}^2} - k^2 \tag{2.21}$$

$$q^2 = \frac{\omega^2}{{c_s}^2} - k^2 \tag{2.22}$$

When solving the frequency equation, it is seen that the phase velocity is function of both the propagating mode and frequency of the wave. Notice here that the term phase velocity

is used instead of the wave velocity as it is more appropriate in the context of dispersive waves. Results from the frequency equation can be illustrated by the phase velocity plotted versus the frequency or the frequency times the radius. Such plot is typically referred as dispersion curves. An example of dispersion curves associated with a circular titanium rod of radius 3.18 mm in vacuum and without attenuation are presented in figure 2.15. Dispersion curves for the first three longitudinal modes (L(0,1), L(0,2) and L(0,3)) and the first three shear modes (F(1,1), F(1,2) and F(1,3)) are presented. From figure 2.15, it is seen that only the first longitudinal mode and the first shear mode can travel over the full frequency spectrum. Indeed, the other modes have a cutoff frequency below which they cannot propagate. Also, at very low frequencies or for very large waveguides, the first longitudinal traveling mode is dominating and is almost non-dispersive (i.e. phase velocity is constant). At low frequency-radius values, the L(0,1) almost corresponds to a pure extensional mode with no lateral motion [141]. Also, the phase velocity of the L(0,1) mode at low frequency-radius values corresponds to the wave velocity c_0 of longitudinal wave in a rod. Alternatively, at high frequency-radius values, the phase velocity corresponds to the wave velocity c_R of surface wave. The associated mode shape can be traced at every points on the dispersion curve as described by Pavlakovic [141]. Examples of different mode shapes associated with figure 2.15 are presented in figure 2.16. Notice that the mode shapes are amplified to facilitate understanding. From figure 2.16, it is seen how the frequency-radius value impacts the lateral motion of the L(0,1) mode.

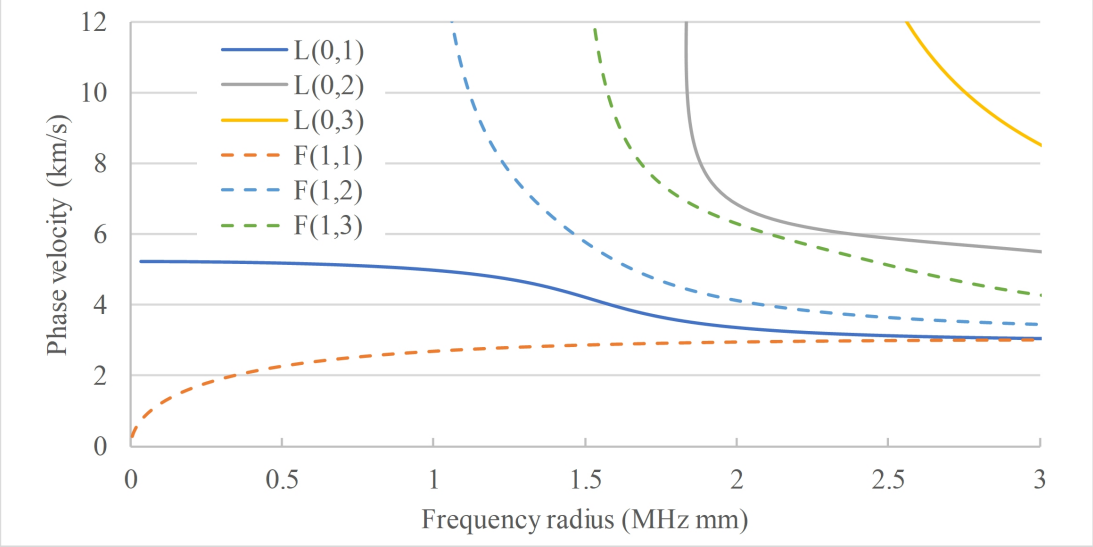

Figure 2.15 Dispersion curves associated with a titanium rod of radius 3.18 mm in vacuum for the first three longitudinal modes (L(0,1), L(0,2) and L(0,3)) and the first three shear modes (F(1,1), F(1,2) and F(1,3))

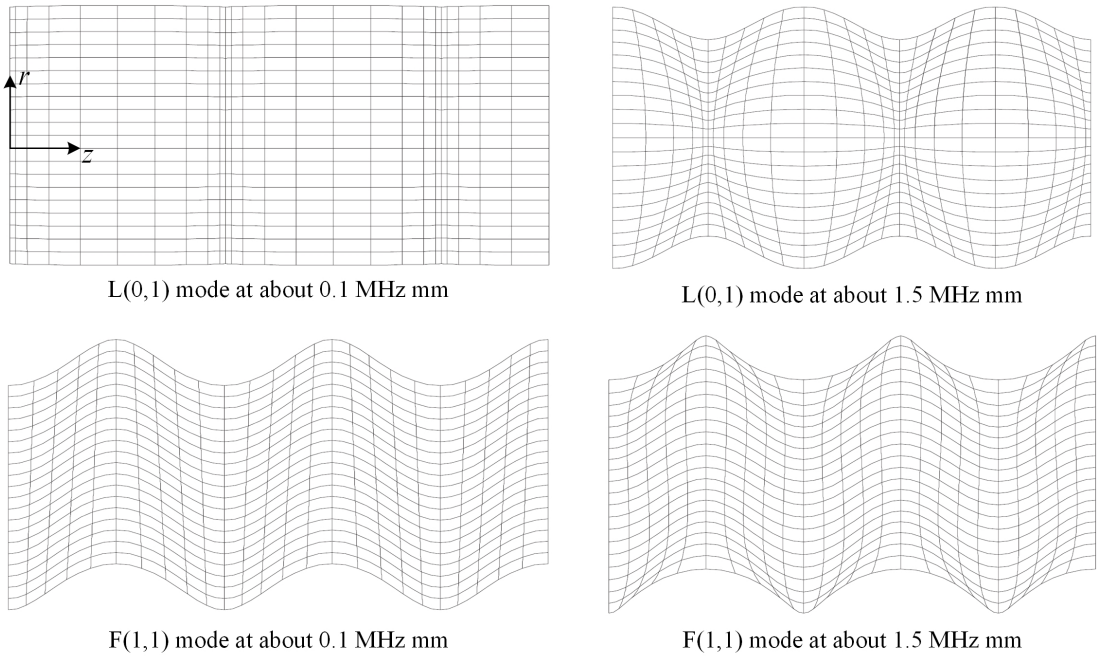

Figure 2.16 Mode shape associated with the different wave types and frequencies from figure 2.15 (where r is the radial direction and z is the longitudinal direction) (not to scale)

Dispersion curves from figure 2.15 and mode shapes from figure 2.16 were obtained from the DISPERSE software version 2.0.2b (demo version). This program was developed by Mike Lowe and Brian Pavlakovic as part of their research about guided wave propagation in multilayered embedded structures [141]. This tool is particularly useful to plot the dispersion curves, mode shapes and attenuation curves for multilayered or embedded waveguides.

To maximize the wave dispersion (i.e. spreading in time) of a waveform emitted at one end of the waveguide, its bandwidth should ideally cover the frequency range where the slope of the dispersive curve is the most abrupt. In addition, the source should be able to mimic as best as possible the shape of the target mode to favor its propagation. This is easily achieved with a compressional transducer for the L(0,1) mode or a shear transducer for the F(1,1) mode. In both instances, it is even better if the transducer is covering the whole cross-section of the waveguide. As an example, and referring to figure 2.15, dispersion is maximized when a broadband compresionnal transducer is used to emit in a titanium rod where the combined frequency-radius value is around 1.5 MHz mm. In addition, it was shown that the elastic properties of the waveguide (Young's Modulus and Poisson coefficient), its density, its geometry (radius and length) and the waveform bandwidth can

all influence the resulting dispersive properties [60]. It was also proposed that there exists a specific combination of these properties that could maximize dispersion.

In summary, it was shown that when the wavelength of the emitted signal is within the same order of magnitude as the thickness of the waveguide, the one-dimensional theory for wave propagation is no longer valid. When this is the case, the Pochhammer-Chree equation can be solved and it is observed that the velocity at which the waveform travels is not constant, but rather depends on the frequency and propagating mode. This is known as wave dispersion and is function of the waveguide elastic properties and its geometry.

2.3.6 Wave attenuation

Up to now, wave propagation theories were considered under the hypothesis of a lossless medium. However, some level of loss is observed when a wave is traveling in an elastic solid. These losses can become very important, especially when a waveform having a high frequency content is propagated over long distance [165]. These losses can be caused by the material itself (absorption and scattering) or by its boundary conditions (leakage into the surrounding medium) [99, 104, 141, 165]. These two categories are sometimes confused in the literature. For clarity, they are referred here as intrinsic loss and extrinsic loss, respectively, and are treated independently. Attenuation is usually given in dB/m or Np/m which are both logarithmic scales (1 Np $\approx$ 8.69 dB). When presenting attenuation values, it is also useful to refer to which frequency and for which material condition it was measured as these parameters can influence the attenuation level.

Absorption intrinsic loss is due to the conversion of mechanical energy into heat. This can be caused by inertial friction, viscous effect and/or mechanical relaxation within the medium. Behavior of intrinsic losses in solids is very complex and vary according to the nature of the solids [99]. No exact theory exists to predict intrinsic loss in solid. However, many experiments were performed as an attempt to characterize these losses in various conditions. As an example, intrinsic loss in solids was shown to vary based on the amount of cold work and heat treatment, which all impact its microstructure [121]. Similarly, the solid composition and crystal geometry can also influence the attenuation coefficient of a material. For the special case of intrinsic loss caused by scattering in a polycrystalline elastic solid, a unified theory was proposed by Stanke and Kino [180]. More recently, experiment performed on titanium alloy Ti-6Al-3Mo-1.2Zr-0.3Si confirmed that there is a relationship between its microstructure (following solution heat treatment) and ultrasonic parameters such as longitudinal wave velocity and intrinsic attenuation [3]. Nicholson *et al.* [128] showed that intrinsic attenuation of cold worked 1 mm diameter stainless steel

wire is reduced after a short 2 min heat treatment, but that it is increased after longer heat treatment (30 and 60 min). It is mentioned that short heat treatment allows for internal strains and stresses to release without grain growth. Generally, the larger the grain size is, the more scattering there is and attenuation increases [4, 121, 128, 138]. When the signal wavelength is much larger than the grain size, scattering is referred as the Rayleigh type and attenuation is proportional to the fourth power of the frequency [62, 165, 180].

When an elastic waveguide is in vacuum, extrinsic losses are null [141]. However, when the waveguide is embedded in another medium, waves traveling in the waveguide may leak into the surrounding. For a circular solid waveguide, the amount of energy that is lost in the surrounding depends on its propagating mode, frequency and the properties of both media. The extrinsic attenuation can be plotted with the help of the DISPERSE software [141]. Example of attenuation curves are presented in figure 2.17 for a titanium waveguide of radius 3.18 mm embedded in motor car oil [2]. When looking at figure 2.17, the same cutoff frequencies are observed for the higher level modes. It is also noted that attenuation increases rapidly with an increasing frequency-radius value. Looking specifically at L(0,1) mode on figure 2.17, the attenuation is low when the mode shape is almost one-dimensional, at low frequency-radius values (refer to figure 2.16). However, when the lateral motion of L(0,1) mode becomes important, coupling with the surrounding medium is high and attenuation resulting from leakage is high. For example, using the L(0,1) curve on figure 2.17, the attenuation values at a frequency-radius of 0.1 MHz mm and 1.5 MHz mm are respectively of about 0.07 dB/m and about 313 dB/m.

In summary, wave attenuation plays an important role when the traveled distance is long and/or when the frequency content of the waveform is high. Two types of attenuation were described: intrinsic loss and extrinsic loss. The intrinsic attenuation is associated to the medium itself and is caused by the conversion of mechanical energy into heat. Scattering of the incident wave with the medium microstructure can also cause intrinsic attenuation. When the waveguide is embedded in another medium, propagating wave may leaked into the surrounding. Extrinsic attenuation is function of the two mediums properties, the propagating mode, the waveguide geometry and the frequency.

2. Considering that the demo version of DISPERSE software is used, only limited materials can be selected. The only fluid material available in the library is motor car oil. It is believed that similar results would be obtainedfl for the same waveguide, but embedded in water.

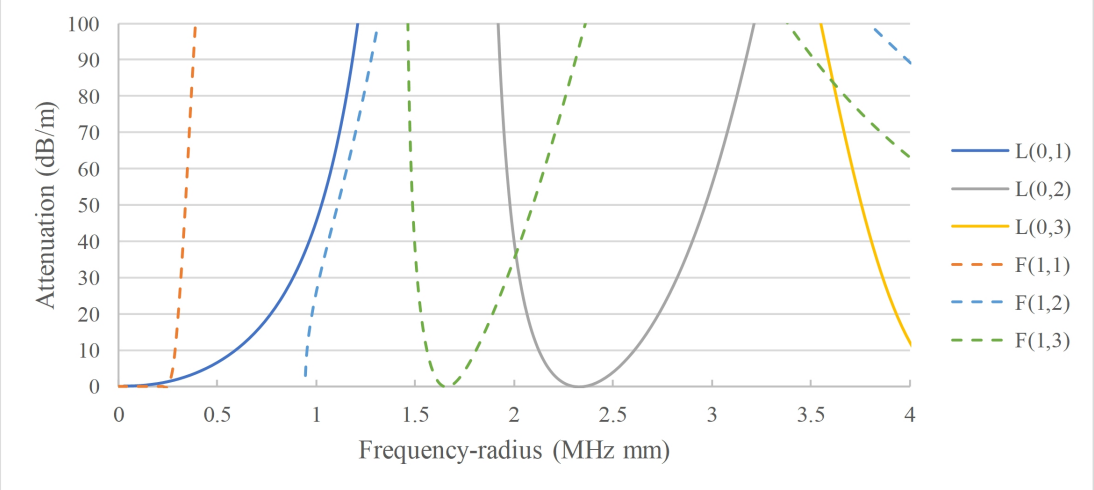

Figure 2.17 Attenuation curves of the first three longitudinal modes and the first three shear modes associated with a titanium rod of 3.18 mm radius embedded in motor car oil

2.3.7 Nonlinearity

So far, it was assumed that the stress amplitude was small enough so that the strain-stress relation was linear. However, in some special situations, this assumption may not hold. This is the case when the stress applied by the source is sufficiently high to deform the medium above its elastic limit (plastic deformation) or, in some viscoelastic media, when the strain-stress relationship is more complex [99]. In simplified cases, nonlinear wave propagation in an elastic solid can be treated similar to nonlinear wave propagation in fluids [198]. A shock wave is formed when a waveform is distorted so much such that its stress-time slope becomes near infinite. This is more easily achieved when the waveform has a high amplitude and a short duration (pulse), like for extracorporeal shock wave lithotripters or in the case of a flyer plate impact experiment [64, 170]. Waveform distortion happens when the traveling velocity depends of the local compression of the medium [176]. When this is the case, the waveform becomes more and more steep t as it travels. In theory, any waves could eventually lead to a shock wave if it propagates over a long enough distance. In practice, shock wave distance-formations are very large such that absorption and loss mechanisms take over and prevent a shock wave to be formed. For a sinusoidal wave traveling in a lossless fluid, the shock wave formation distance d_{sw} is given by equation 2.23, where ρ_a is the fluid density at rest, c_a is the wave velocity of the fluid at rest, β is the nonlinear coefficient, p_m is the peak pressure and f is the wave frequency [31, 176].

$$d_{sw} = \frac{\rho_a c_a^3}{\beta p_m 2\pi f} \tag{2.23}$$

For example, let's assume a sinusoidal wave with a frequency of 450 kHz and an amplitude of 1 MPa traveling without loss in water with a density of 1000 kg/m^3, a wave velocity of 1500 m/s and a nonlinear coefficient of about 5 [209]. For this example, the corresponding shock wave formation distance calculated from equation 2.23 is about 7 cm. In a solid, the stress level required to produce a shock wave is usually far beyond its elastic limits and a large deposition of energy in a short amount of time is necessary (explosion, laser and high velocity projectile impact) [51, 170, 215].

2.3.8 Acoustic properties

Table 2.2 is presented for reference only and lists the properties, wave velocities and specific impedance of various media that are of interest in the context of this research work.

Table 2.2 Acoustic properties of various materials [135]

Medium	E (GPa)	ρ (kg/m^3)	c_l (m/s)	c_s (m/s)	c_0 (m/s)	Z_l (MRayls)
Air at 20°C	–	1	331	–	–	0.0004
Water at 25°C	–	998	1497	–	–	1.49
Aluminum	69	2700	6042	3040	5060	17.3
Ti-6Al-4V	114	4480	6100	3100	5040	27.3
Ti-11.5Mo-6Zr-4.5Sn*	79	5060	5100	2400	3950	25.9
Stainless steel 304V	193	7890	5800	3100	4950	45.7
Lead	14	11200	2200	700	1120	24.6
Quartz	70	2200	5500	3750	5640	12.1

E is the Young's Modulus,
ρ is the density,
c_l is the longitudinal wave velocity in an infinite solid or in a fluid,
c_s is the shear wave velocity in an infinite solid,
c_0 is the longitudinal wave velocity in a solid rod and
Z_l is the specific acoustic impedance calculated from the longitudinal wave velocity
*Calculated based on its elastic properties [13]

CHAPTER 3

METHOD

This chapter is divided in two main sections. The first section presents the method used for the design of the proposed CTO crossing system. The second section describes the experimental methods associated with the different tests that were planned to evaluate the system performances.

3.1 Design strategy

The following subsections present the method and guidelines that were used to design the proposed CTO crossing system. These subsections will describe the experimental iterative process and the finite element analysis (FEA) model that were used.

3.1.1 Experimental trial and error iterative process

One of the key steps in the development process of the proposed CTO crossing system consisted of defining the geometry and material of its key components. As it will be described in section 4.1, the two main sub-systems of the shock wave generator are the spatial and temporal concentrators. These are used to amplify the mechanical waves, emitted from piezoelectric transducers. The geometry of these two sub-systems, relative to the system wavelength, will dictate the performance of the overall system. In addition, the section reducer, core wire and its grind profile also constitute key components of the design of the proposed CTO crossing system.

The development of the proposed CTO crossing system was mainly based on an experimental iterative process. Considering that such design method can be time consuming and costly, past experiences, theories about wave propagation and finite element simulations were all used during design to limit the number of iterations. One advantage of the proposed method is that new knowledge is obtained sooner in the development process. Generally, each iterative phase starts by making an assumption based on past experiences and the associated theories. Then, specifications of the prototype are drafted and, optionally, different FEA simulations are performed. Specifications can be refined based on the results from the simulations and a prototype is built. The prototype is tested and the

hypothesis is confirmed or not. Knowledge from this iterative phase is then transferred into the next one.

As mentioned previously, past experiences with such design was obtained during my Master's research project. For example, understanding of wave propagation in solids, and experience with piezoelectric transducers and associated equipment were acquired [152]. For example, in my Master project, it was demonstrated that mechanical waves emitted from transducers and amplified while traveling in solid structures can reach amplitudes high enough to break an aluminum rod [152]. Theories associated with wave propagation in solids were summarized in section 2.3 and were used during the design process. From these, it was learned that parameters like wavelength, waveform bandwidth, boundary conditions and attenuation from the medium are key elements to consider. The FEA model used for simulations is presented and discussed in more details in section 3.1.2.

Different prototypes were built during the development process. For example, many prototypes of the spatial concentrator, temporal concentrator, section reducer and core wire were built. These sub-systems of the proposed CTO crossing system will be described in section 4.1. On occasion, smaller and more cost-effective versions of the different sub-systems were prototyped. For example, the first prototypes of the spatial concentrator were smaller and used only three transducers instead of nine, as in the final design. Similarly, a straight rod of 1.8 m long was used at first instead of the final 15 m long temporal concentrator. For some tests, more than one sub-system was assembled.

When testing prototypes in the experimental iterative phase, different test methods were used and relative results were compared. The most common test method used is the one described in section 3.2.1. This method consists of using one or more piezoelectric transducers to emit mechanical waves in the tested sub-system and to use a hydrophone to measure the output pressure pulse in water at the opposite end. Alternatively, the output pressure waveform could be measured with a contact transducer instead of the hydrophone. This transducer was typically the same as one of the emitting transducer. Indeed, one unique feature of piezoelectric transducers is that they can be used both as an emitter and a receiver. A similar acquisition system as the one described in section 3.2.1 was used with the contact transducer. This technique was favored when the surface area at the measuring end was sufficiently large to receive the flat contact sensor. In some circumstances, a special holder was necessary to position the contact transducer, but most of the time, the transducer was hand held.

3.1.2 Finite element analysis model

A similar finite element model as the one developed during my Master's research work was used here [152]. The proposed FEA model is described below. PZFlex software (Cupertino, United States) was used to build the model, to create the mesh and to solve the different problems. PZFlex is commonly used by the industry for the design of piezoelectric transducers and sensors, for non-destructive testing and for medical ultrasound diagnostic imaging. PZFlex uses a time domain finite-element-method (FEM) solver. Version 2.3 of PZflex was used.

Many different geometries, conditions and problems were simulated. For simplicity, only a two-dimensional axisymmetric model of a titanium rod is presented here. This model is shown on figure 3.1. The following properties were used in the model for the titanium material: Young's Modulus of 110 GPa, density of 4480 kg/m^3, Poisson coefficient of 0.3, longitudinal wave speed of 6100 m/s, shear wave speed of 3300 m/s and without attenuation. In the proposed FEA model, both extremities of the rod have absorbing conditions and an axisymmetric condition was applied on the central axis of the rod (bottom). Therefore, the y axis corresponds to the radius of the rod and the z axis corresponds to its length. The top surface of the rod was free and considered to be in contact with void. In this model, the emitting surface was on the left and the receiving surface was on the right. Even though PZFlex can be used to simulate piezoelectric transducer emission, such feature was not used in the current model for simplicity. A predefined stress condition was applied simultaneously to each individual element along the emission face. Any waveforms can be loaded for the excitation. For example, typical output waveforms from a transducer or a gaussian pulse of similar shape were used. The resulting waveform at the receiving end of the model was measured by averaging all elements of the receiving face. To mimic a slip condition between the transducers and the rod, only the z longitudinal stress component was considered for emission and reception. However, it should be noted that the model can account for other kinds of propagating modes (i.e. torsion and flexural). Typically, 60 elements per center wavelength (i.e. wavelength associated with the center frequency of the waveform) was used for the simulations, which is in accordance with other similar works [2, 148]. Rectangular elements were using during meshing with maximum aspect ratio of 1:2.

The FEA model presented above was validated against analytical calculation and experimental testing as described in my Master's thesis [152]. It was found that this model could appropriately simulate the dispersive effect resulting from the propagation of a gaussian

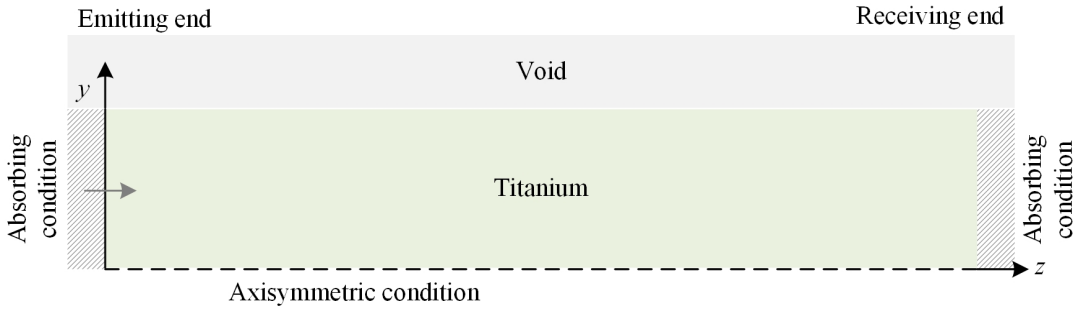

Figure 3.1 Two-dimensional model of a rod used during FEA simulation

pulse through a solid rod at the frequency range of interest.

3.2 Experimental methods

The next subsections present the different experimental methods used to evaluate the preliminary performance of the proposed CTO crossing system. First, the method used to measure the output pressure pulse near the distal tip of the active guidewire is presented. Second, the development and selection of a CTO surrogate material are described, followed by the associated crossing method. Third, the protocol used to obtain ex-vivo CTOs from amputation is presented followed by a description of the ex-vivo CTOs crossing method. Fourth, the protocol used to evaluate endothelial cell viability after exposition to shock wave is presented. Lastly, the protocol associated with an acute healthy animal study in which the proposed CTO crossing system was used is outlined.

3.2.1 Pressure measurement method and equipment

Characterizing the CTO crossing system performance can be very challenging. The size of the active guidewire, amplitude of its tip displacement and the pulse duration limit the kind of technology that can be used to measure the output pressure waveform. One method proposed to characterize the system performance was by measuring the resulting pressure waveform propagating in water near the active guidewire distal tip. Pressure measurement was done with a hydrophone sensor immersed in water and placed in front of the distal tip of the active guidewire. Different hydrophone sensors were used. Two of the most common sensors were (i) the fiber optic hydrophone and (ii) the needle hydrophone. Both sensor technologies were used in the context of this research. A fiber-optic pressure measurement system from Precision Acoustics (Dorchester, United Kingdom) and a 2 mm diameter needle hydrophone system (including a DC coupler and a submersible preamplifier) from the same company were used. Their principal characteristics are summarized in table 3.1.

Table 3.1 Comparison between the fiber-optic and needle hydrophones

Characteristics	**Fiber-optic** [145]	**Needle (2 mm)** [144]
Manufacturer	Precision acoustics	Precision acoustics
Sensing diameter (mm)	0.01	2
Typical sensitivity (V/MPa)	0.1-0.15 (at 3 MHz)	3.5 (averaged over 0.5-8 MHz)
Sensitivity tolerance	±3 dB	±3 dB
Sensitivity frequency response	Vary by a factor of 5 to 10* [110]	flat (±2 dB) from 0.4 to 6 MHz
Min. pressure (MPa)	0.01	0.001
Max. pressure (MPa)	15	20
Usable frequency range (MPa)	0.25-50	0.1-10

*frequency response of this sensor is not flat and deconvolution is needed in case of wideband signal

One advantage of the fiber optic hydrophone is that it can measure temperature. However, it was found that probe to probe durability and repeatability were less with the fiber optic system compared to the needle system. The fiber optic system is also more expensive. Even though the needle hydrophone is more sensitive, its size limits precise three-dimensional pressure mapping and makes its more directional [25]. However, because of its higher sensitivity, signal-to-noise ratio is improved with the needle hydrophone. In comparison, averaging is usually necessary when the fiber optic hydrophone was used, which increases pressure measurement time and reduces sensor durability. Another advantage of the needle hydrophone sensor is that it can be used with a submersible attenuator or a booster amplifier to allow measurement of larger or smaller signal levels.

The method of use for both sensors is similar except for the specific technology components. For simplicity, only the pressure measurement method using the needle hydrophone is presented. The objective of the pressure measurement is twofold: (i) calibrate the system as described in section 4.1.3 and (ii) characterize its performance. Both objectives can be achieved with the same sensor and jig.

Figure 3.2 shows the pressure measurement jig along with the reference axis. Here, the z-axis is taken along the length of the active guidewire. The referential origin is located at the tip of the active guidewire. It is supposed that the pressure field is symmetrical around the z-axis and therefore the x-axis and y-axis directions are less relevant. A water tank is used to immerse the sensor and the tip of the active guidewire. Tap water at room temperature was used. Precaution should be taken to limit the presence of air bubbles

near the sensor and the test device. A custom holder is used to hold the sensor in position. The length of the active guidewire can be in air or inserted through a catheter flushed with water to better represent clinical conditions. Sharp bends should be avoided. The distal tip of the active guidewire is positioned within a tube and through a silicone sleeve attached at its bottom. This sleeve is less than 1 mm thick and is used to secure the active guidewire in position using friction. The active guidewire holder is fixed to a three-dimensional (3D) micro-positioner which facilitate alignment of the active guidewire with the pressure sensor. Also, two digital microscopes are be used to facilitate the positioning. For reference, a 3D micro-positioner from Thorlabs and two digital microscopes from Dino-Lite were used.

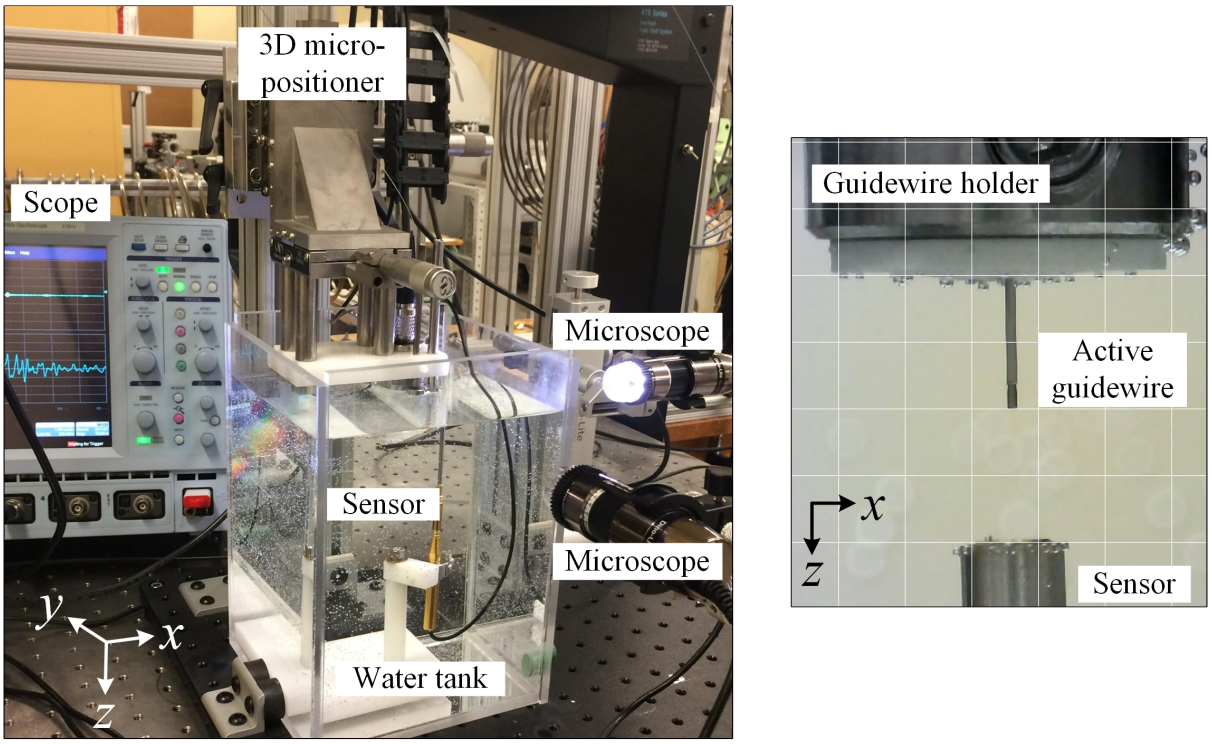

Figure 3.2 Pressure measurement setup

The 2 mm needle hydrophone is plugged to a submersible preamplifier which is connected to the DC coupler. The DC coupler is connected to a measurement system (i.e. an oscilloscope). Desktop oscilloscope like model HDO4034 from Teledyne LeCroy (Chestnut Ridge, United States) or oscilloscope card model PXI-5105 from National Instruments (Austin, United States) can be used. When the scope card is used, it is interfaced with a computer and Labview. Optionally, an attenuator can be used between the sensor and its preamplifier. Alternatively, a booster amplifier can be used between the DC coupler and the scope.

The following steps describe the pressure measurement procedure:

1. Mount the needle hydrophone sensor in its holder.
2. Connect the needle sensor, as described above.
3. Position the needle hydrophone in the tank.
4. Fill the tank with water and let rest until the air bubbles disappear.
5. Connect the active guidewire to the shock wave generator.
6. Set the shock wave generator to the appropriate parameters.
7. Flush the catheter (optional).
8. Insert the active guidewire inside a catheter (optional).
9. Insert the tip of the active guidewire through the tube holder and silicone sleeve.
10. Center the active guidewire relative the needle hydrophone sensor.
11. Position the distal tip of the active guidewire at the appropriate distance above the sensor.
12. Set the appropriate acquisition parameters on the scope.
13. Activate the CTO crossing system and record the waveform.

To account for connection and setup variability, each measurement is averaged over at least two different connections and installations. Similarly, to reduce noise from the signal, each pressure measurement could be averaged over about 30 acquisitions.

Test devices, console settings and specific test conditions are presented in section 4.2.1 along with the associated results.

3.2.2 Surrogate material development

Cadavers, amputation specimens and/or animals are typically used to verify the performance of new medical technology, especially in the field of CTO crossing. However, accessibility to cadavers and amputation specimens can be complex, long and unreliable. Limited availability and heterogeneity among the different specimens makes it also difficult to compare the performance of various prototypes. Different animal models for CTOs have been proposed using ligature constriction, collagenase injection, thermal injury and polymer, copper stent or ground bone implantation in the coronary arteries [186, 187]. However, none of these animal models have gained wide adoption. Moreover, such animal models are expensive and the mortality rate during the CTO implantation procedure remains high (about 50%). Therefore, there is a need for a surrogate material that can mimic the properties of a CTO and that can be used in a repeatable manner, on the bench and at low cost.

To the author's knowledge, such surrogate model does not exist. Therefore, in the context of this thesis, it was proposed to create a CTO surrogate model. For simplicity and knowing that calcified CTOs are the most difficult to cross (refer to sections 1.1 and 2.1), the proposed surrogate was intended to mimic only the calcified component of a CTO. This surrogate development work was previously published and only a summary is provided here [153].

The goals of this surrogate study were to characterize the mechanical properties of calcified plaques retrieved from human femoral arteries and to recommend an artificial analogue that can mimic those plaques. To find the proper analogue, the elemental composition, micro-structure, density, porosity, hardness, ultimate compressive strength, nanoindentation properties and resistance to erosion from cavitation were characterized on calcified plaques and several potential analogues.

Three superficial femoral arteries were retrieved from above the knee lower limb amputations of three different subjects. The research protocol used for this experiment was approved by the institutional board and ethics committee from the Centre de recherche du Centre hospitalier universitaire de Sherbrooke (Sherbrooke, Quebec) (#13-026). The femoral arteries were retrieved within one hour following the amputation surgery and were stored in a saline solution or a Krebs solution with 10% DMSO (wt/wt) before being frozen at -20°. Before testing, the arteries were thawed at 4°C for a maximum of 24 hours. The arteries were then dissected to isolate only the calcified areas. The calcified plaques were identified by palpation, observation and confirmed by SkyScan 1172 micro-tomography imaging (Kartuizersweg, Belgium). Figure 3.3 illustrates an example of a 4 cm long segment of a proximal femoral artery at different stages of dissection and using different imaging techniques. As observed in figure 3.3, the artery segment is irregular and highly heterogeneous with a mix of soft and hard tissues.

Figure 3.4 presents some examples of medial calcified plaque samples retrieved from the femoral arteries after dissection and cleaning. The calcified samples were then dried at room temperature for 24 hours before mechanical characterization. The geometry of these plaques is related to a portion of a cylinder and their average dimensions are the following: thickness of 1.7 $\pm$ 0.4 mm, width of 3.6 $\pm$ 0.9 mm and length of 5.7 $\pm$ 1.2 mm.

The mechanical properties of four potential analogues were studied against the ones from the calcified plaques. Three of the potential surrogates were plaster-based materials (plaster of Paris, Ultracal-30 and Begostone) and one was bone cement, hydroxyapatite. The three plaster materials were selected based on the premise that they are already used

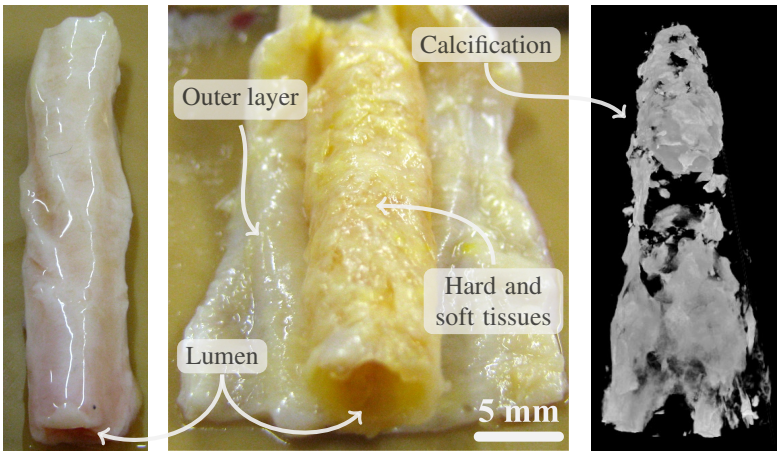

Figure 3.3 Femoral artery segment (left: unaltered segment, middle: same segment during dissection, right: same segment under micro-tomography)

Figure 3.4 Calcified plaque samples retrieved after dissection and cleaning

as kidney stone analogues [65, 89, 111]. Because kidney stones represent calcification deposits [111], it is hypothesized that their artificial counterpart can as well be used to mimic atherosclerotic calcified plaques. Following the same rational and knowing that vascular calcification resembles bone [26, 55, 63, 106], bone cement, hydroxyapatite was also selected as a potential analogue.

All four potential surrogate materials and the medial calcified plaques were characterized for their mechanical properties. Microscopic analysis was performed on two calcified plaques casted in epoxy (Buehler EpoxyCure 2) (Lake Bluff, United States), ground, polished and metallized with gold. A Hitachi S-4700 scanning electron microscope (SEM) (Tokyo, Japan) equipped with an energy dispersive x-ray spectrometer (EDS) was used to observe the sample under high magnification and to determine its elemental composition. Average scan measurements were used to assess the elemental composition and the Ca/P ratio (calcium/phosphorus). This ratio is useful to compare these calcified plaques with bone.

The density and porosity were calculated by measuring the dry weight, wet weight and volume of the different samples [10]. The mean density and porosity index were calculated based on a minimum of three (3) samples for each analogue material and ten (10) samples of the calcified plaques.

Micro-hardness was measured with a Buehler Micromet I hardness tester (Lake Bluff, United States). A minimum of five indentations per sample were performed. The average micro-hardness was calculated using one (1) specimen per analogue material and eight (8) calcified plaques.

Compression strength was measured using a TA.XT Plus machine from Texture Analyzer (Hamilton, United States). As shown on figure 3.5, samples were compressed between two plates and the peak force was recorded. Cylindrical samples of ⌀ varying from 3 mm to 6.35 mm and a height varying from 6 mm to 12.7 mm were used for the potential analogue materials. To form the calcified plaque cylindrical samples, they were first casted in larger epoxy pellet. Then, they were carefully machined to remove excess epoxy and to reach a uniform cylindrical shape with a diameter of $\approx$ 2 mm and a thickness of $\approx$ 1.2 mm. The size, geometry and the non-uniformity of the plaque samples limited the dimensions and the number of useful test cylinders. Compressive testing was performed on dry calcified plaques and no difference was made between the axial and radial directions. A minimum of three samples (3) per analogue material and eleven (11) calcified plaque cylinders were tested. Outlier results for the calcified plaque samples were removed from the data. These outliers were detected when the compressive strength or the elastic response obtained were similar to the one of the epoxy alone. Considering this, only five (5) compressive test results were kept for the calcified plaques.

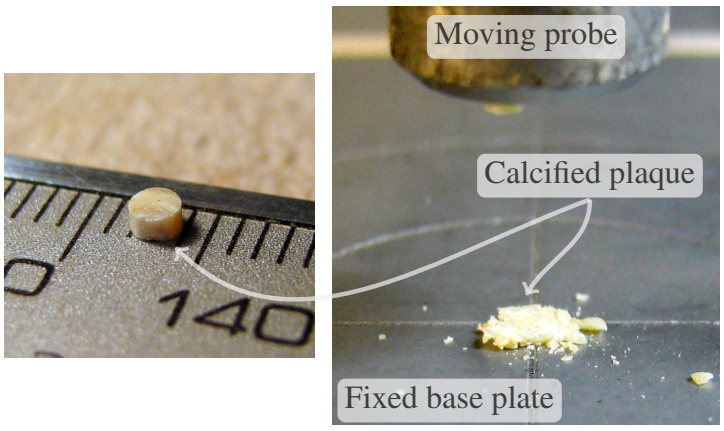

Figure 3.5 A calcified plaque cylinder sample before (left) and after (right) a compressive test (dimensions in mm)

Resistance to cavitation erosion was measured as the sample mass removal rate. For this test, the samples were immersed in water and positioned at about 5 mm below a CPX130PB ultrasonic probe having a 3.18 mm diameter from Cole-Parmer (Vernon Hills, United States), as shown on figure 3.6. Once activated, the ultrasonic probe was creating cavitation and streaming effects which eroded the surface of the sample. For the analogue materials, blocks of ≈5×5×5 mm^3 were used while calcified plaques were used as is after dissection. Six (6) specimens of calcified plaques and five (5) specimens of each analogue were used.

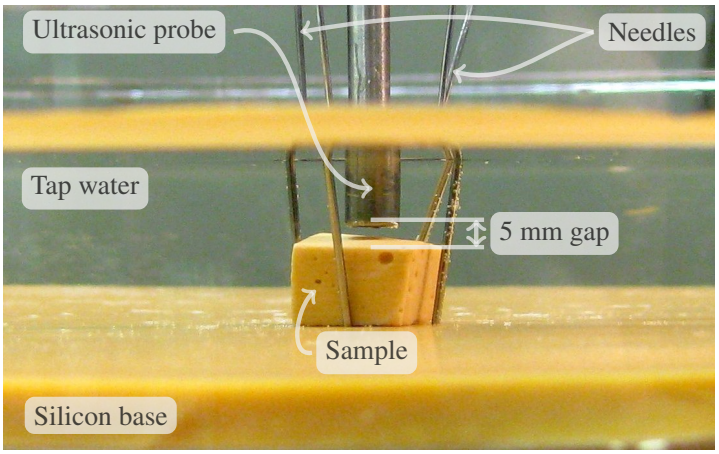

Figure 3.6 Cavitation erosion bench test

The elastic-plastic nano-hardness nH and reduced Young's modulus E_r of the calcified plaques were evaluated by depth-sensing nanoindentation. A TriboIndenter Hysitron TI-950 (Kartuizersweg, Belgium) was used along with a Berkovich diamond indenter. A trapezoid load function with a maximal force of 4000 μN was applied. The load and unload periods were of 5 s each and a constant force was maintained for 2 s. Before launching the test sequence, the tip geometry and system compliance were calibrated using a fused quartz sample. Thermal drifting was also measured and compensated for during the tests. The reduced modulus E_r was obtained using 3.1 where S is the stiffness calculated at the upper portion of the unloading phase of the experimental force-displacement curve and A_p is the projected contact area between the indenter and the sample at maximum load [133]. The Young's modulus of the sample E is calculated using 3.2 where subscript i refers to the indenter material, subscript s refers to the sample and ν is the Poisson's ratio. The diamond indenter used had the following properties: $E_i = 1140$ GPa and $\nu_i = 0.07$. It was assumed that the Poisson's ratio ν_s of the sample is similar to bone and can be approximated to 0.3 [216].

$$E_r = \frac{S\sqrt{\pi}}{2\sqrt{A_p}} \tag{3.1}$$

$$\frac{1}{E_r} = \frac{(1-\nu_i^2)}{E_i} + \frac{(1-\nu_s^2)}{E} \tag{3.2}$$

Calcified plaque samples previously cast in epoxy were reused for nanoindentation investigation. Before testing, they were polished down to 0.05 μm using diamond and alumina suspensions along with polishing cloths. Nanoindentation was performed at room temperature, with dry samples, and in both the axial and the radial direction relative to the physiological orientation of the calcified plaques. Figure 3.7 presents the calcified plaque sample that was indented axially. The zoom selection shows the position of the 10 investigated zones (black square markers). Each zone is spaced by $\approx$ 200 μm. Each zone also represents an array of 3 $\times$ 3 with a spacing of 20 μm between each indentation. A total of 90 indentations were realized on this sample. Outlier measures observed from tip slippage on the force-penetration curve were removed from the data set. Between five and nine indentations per zone were kept. It was not possible to characterize the potential analogue materials using this method as the very low surface roughness required could not be obtained.

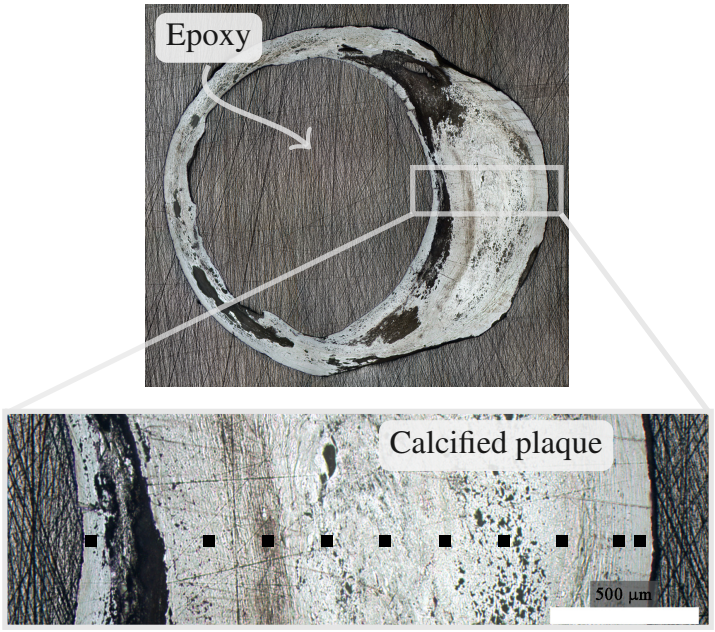

Figure 3.7 Calcified plaque indented axially (through the page) and zoom in the section of interest (black square markers indicate the nanoindentation zones)

Figure 3.8 shows an example of the micro-structure arrangement of a calcified plaque. At a zoom of 30000× the micro-structure looks like nodular aggregates. The main fundamental elements (>98 atomic% of the composition) of these samples were calcium (Ca), oxygen (O), phosphorus (P) and carbon (C). The average specific Ca/P ratio (atomic%) was 1.50 on both samples which is comparable with bone and pathological calcification [106].

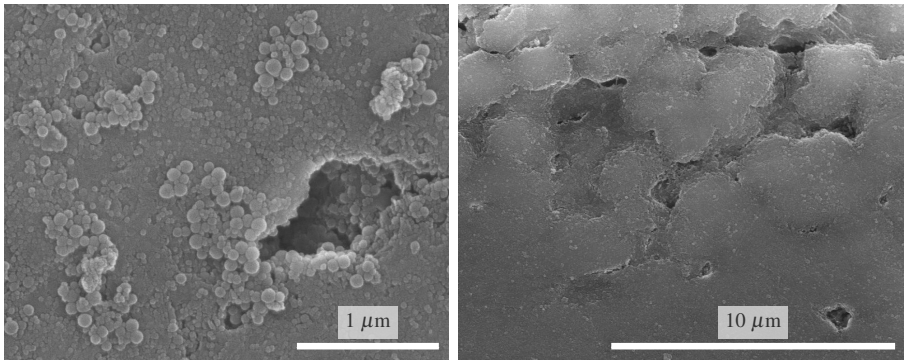

Figure 3.8 SEM images of calcified plaque micro-structure (magnification level: left = 30000× and right = 5000×)

Table 3.2 and figure 3.9 presents a summary of the mechanical properties for each potential surrogate material and for the calcified plaque. Average values are presented along with the standard deviation. Young's Modulus for the three plaster-based materials was reported from the literature as nanoindentation was not possible to obtain [65, 90, 111]. The micro-hardness of the plaster of Paris could not be measured since its porosity was too large to allow proper indentation. Resistance to cavitation erosion of hydroxyapatite was not significant enough and was then considered null at the level of intensity tested. The ultimate compressive strength of hydroxyapatite was also too large for the TA.XT system and was estimated to be >50 MPa. The ultimate compressive strength of the calcified plaques presents considerable variability. This could be caused by the low number of test samples and the presence of natural micro-cracks and residual epoxy within the samples. Also, one of the calcified plaques demonstrated a more important resistance to cavitation erosion compared to the other. After investigation, the mass loss was attributed to soft tissue that was not properly removed from the plaque before testing. This value was thus removed from the data set. Nanoindentation results between the radial and axial direction were about the same with only a 10% decrease in the radial group. Therefore, only the axial results are presented. The micro-hardness of calcified plaque was about 30% less compared its nano-hardness results. This is consistent with results from the literature [149]. Therefore, only the micro-hardness results were presented for comparison.

Table 3.2 Mechanical properties of calcified plaque and potential analogue materials

Material	μH (MPa)	S_{max} (MPa)	Density (kg/m^3)	Porosity (%)	Cavitation (mg/min)	E (GPa)
PP	≈ 200	6.4 ± 0.2	1176 ± 12	41 ± 2	18.6 ± 2.3	9 - 10
U-30	706 ± 255	36 ± 5	1542 ± 38	19 ± 2	9.4 ± 0.7	15
Bego	676 ± 186	58 ± 18	1928 ± 9	4 ± 1	4.5 ± 0.4	27-30
HA	4567 ± 872	> 50	2619 ± 7	1 ± 0.1	≈ 0	–
CP	597 ± 158	62 ± 27	1632 ± 176	14 ± 6	0.2 ± 0.25	22

Micro-hardness (μH), ultimate compressive strength (S_{max}), Young's modulus (E), plaster of Paris (PP), Ultracal-30 (U-30), Begostone (Bego), hydroxyapatite (HA) and calcified plaque (CP)

From results presented in table 3.2 no candidate stands out as the perfect match for medical calcified plaque. The commercial hydroxyapatite specimen chosen for this study was too dense and much too hard to represent a proper analogue. As highlighted in the left radar chart from figure 3.9, plaster of Paris is too porous, not dense enough, and not stiff enough when compared to calcified plaque. Nonetheless, many similarities can be observed between Ultracal-30, Begostone and calcified plaque, as shown in the right radar chart from figure 3.9. Apart from the resistance to cavitation erosion, all other properties are within the same range.

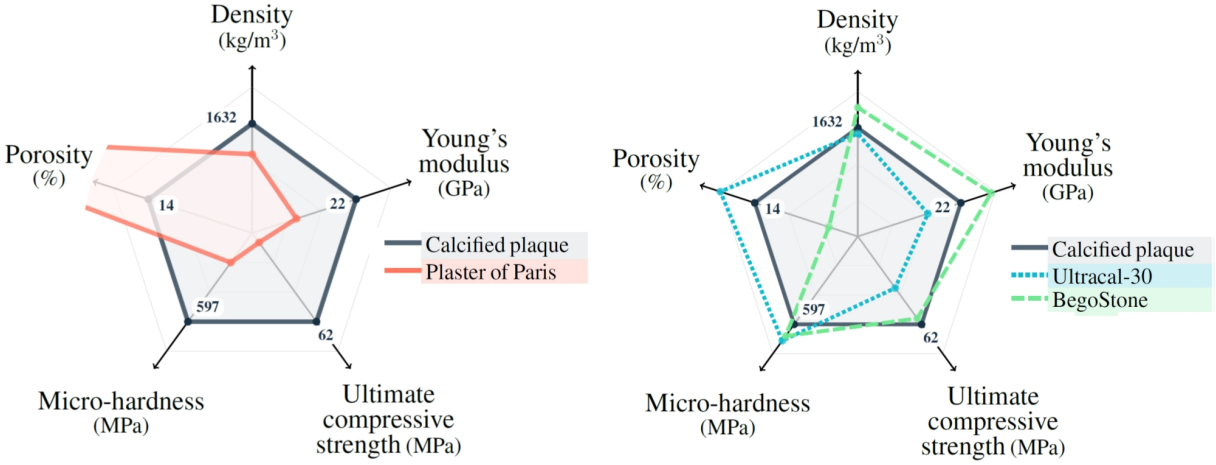

Figure 3.9 Radar charts comparing the mechanical properties of calcified plaque with Plaster of Paris (left), and Begostone and Ultracal-30 (right)

It is understood that other potential surrogate materials for calcified plaque may exist. Also, a mixture of more than one material could also be interesting to try. However, in the context of this research work and based on the provided evidences, it is suggested

that both Ultracal-30 and Begostone represent good surrogate materials to mimic medial calcified plaque.

3.2.3 Method for crossing surrogate material

The goal of this experiment was to demonstrate that the proposed CTO crossing system can drill through material having mechanical properties like calcified plaques found in CTOs. As described in the previous subsection, two kinds of plaster-based materials were proposed as surrogates for medical calcified plaque. For this specific test, Begostone Plus (ref #54812) from Bego (Germany) was selected. Instructions for use from the vendor were followed for its preparation [27]. The instruction basically consists of mixing the Begostone powder with water and letting it dry for about 2 hours or more. It is important to note that changing the plaster-water ratio may alter the properties the resulting material. Therefore, it is important to follow the same preparation method every time a new batch is processed.

Custom molds were used to produce material having the same geometry and thickness. The molds consist of a thin (0.5 mm to 1.5 mm) silicon sheet in which circles of about 6.4 mm in diameter were punched. During sample preparation, the plaster-water mix was poured into the circle cavities of the mold, a thin plastic sheet was layered over and squeezed using a clamp. Once the Begostone cylindrical samples start to set, the clamps and the plastic sheet ere removed to complete the curing process in air.

Figure 3.10 shows an example of the bench test setup used for the surrogate crossing experiment. For this experiment, a vascular model with different tortuosity levels can be used and plugged to a custom water tank which is used to immerse the surrogate. The tortuous model can mimic the coronary or the peripheral vasculature as needed. Alternatively, a straight model configuration can also be used. The surrogate holder can be used optionally with a load cell to measure the forward push force applied to the surrogate. The surrogate holder allows to position the surrogate when it is drilled by the active guidewire. When applicable, the Omega RFC03-5 load cell with Omega display DFG-RS5 (or similar) are typically used for this test. A catheter can also be used to support and position the active guidewire close to the surrogate. Different catheters can be used depending on the active guidewire configuration. When a catheter is used, it should always be flushed with water before inserting the active guidewire in to better simulate clinical conditions. Optionally, a microscope can be used over the surrogate to monitor and record the crossing experiment. When this is the case, a Dino-Lite digital microscope (Taiwan) is typically used.

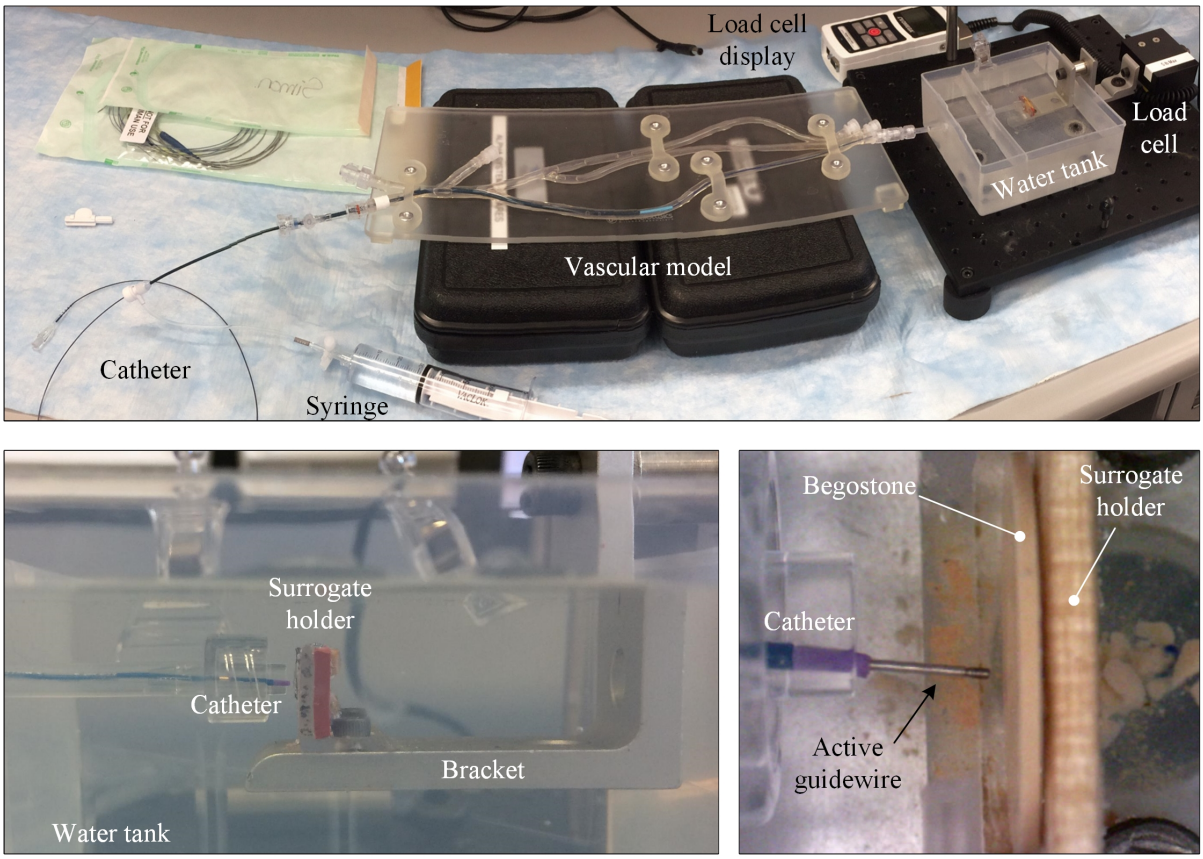

Figure 3.10 Bench test setup used for crossing surrogate

Water at room temperature was used in this experiment to simulate an in-vivo environment. Water and blood have similar properties, especially about their density, speed of sound and surface tension [44]. The main difference between blood and water is related to their viscosity; blood is about four times more viscous then water. Other fluids could have been used, like soap or glycerin, to even better mimic blood. However, these are less convenient to use and more difficult to clean in between tests. It is believed that the effect of the selected fluid on the test results is minimal as long as only relative results are used.

This experiment was used to evaluate the crossing ability of different active guidewire configurations, in different test conditions and at various shock wave generator parameters. The crossing rate can be reported in different units based on need (e.g. mm/s, mm^3/s or mm^3/pulse). When presented in mm/min, the thickness of the surrogate is used. When presented in mm^3/min, both the thickness and the surface area of the resulting drilled hole are used. This may be more convenient when comparing prototypes having different tip size. Specific test conditions will be presented in section 4.2.2, along with the associated results.

3.2.4 Ex-vivo human CTO accessibility and preparation

The objective of this study was to demonstrate the crossing ability of the proposed CTO crossing system in simulated conditions. The study was reviewed and approved by the institutional research board and ethics committee of the Centre de recherche du Centre Hospitalier Univertaire de Sherbrooke (Sherbrooke, Quebec) (#13-026). This protocol allowed for the extraction of CTOs from fresh amputated lower limbs. Subjects with a documented CTO were screened and recruited. Typically, within one hour after the amputation, the vascular surgeon dissected the diseased amputated leg, retrieved the occluded vascular tree and stored it in a phosphate buffered saline (PBS) solution at 4°C. An example of a dissected arterial tree is shown on figure 3.11.

Figure 3.11 Example of a dissected arterial tree extracted from an amputated leg

Within 24 hours, the sample was recovered and frozen at -20°C. This preservation method is believed to minimize the degradation of the mechanical properties of the artery samples [57, 182]. Before the crossing experiment, the arterial tree was thawed at room temperature for 2-5 hours. The position of the occlusion was identified by carefully inserting a commercial guidewire through the artery true lumen. Occluded portions were sectioned in segments between 1 cm to 5 cm long. Excess soft tissues around the vessel (muscle, nerves and fat) were removed. When not used immediately, each CTO segment was stored at -20° in a 50 ml test tube filled with PBS solution. The position of the artery segment in the leg was not recorded at that time.

3.2.5 Method for crossing ex-vivo human CTO

Before proceeding with the crossing procedure, the short CTO segment was mounted on a custom holder as shown on figure 3.12. This holder was used to pin the occluded segment and to facilitate the positioning of a catheter. A silicone pad was used to fix the artery

with needles. These were positioned on both sides of the artery, in the soft tissue region. This custom holder is also designed to fit inside a 50 ml test tube so that the occluded segment could be immersed in a fluid (water or PBS) to better mimic clinical conditions.

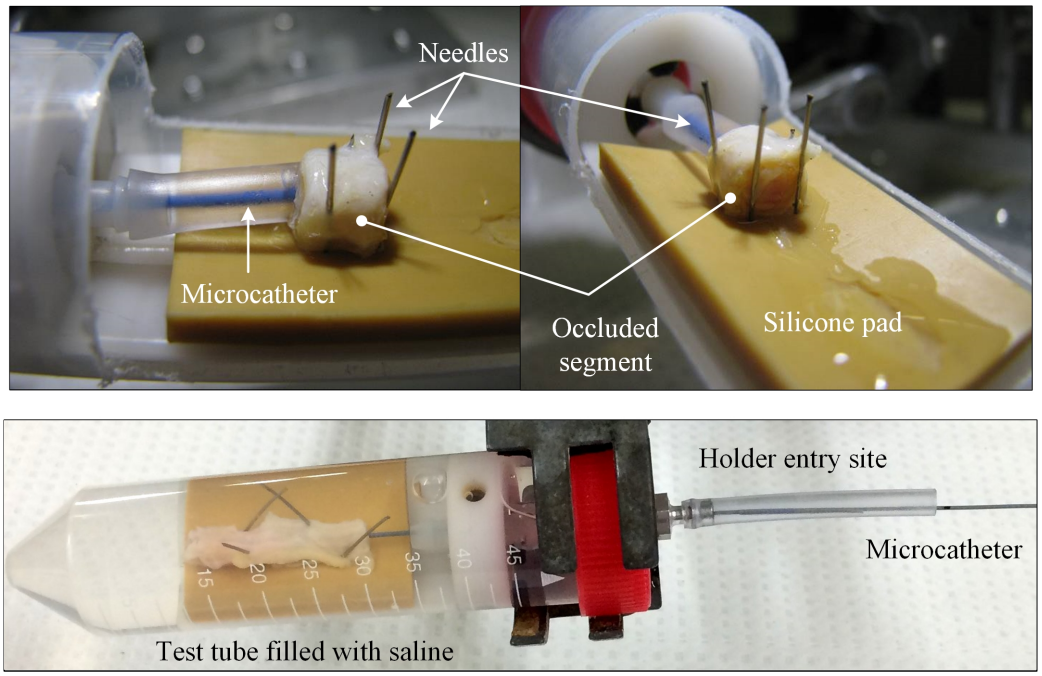

Figure 3.12 Holder used to position the occluded artery segment during the simulated recanalization intervention

Once the occluded artery was pinned to the holder, a catheter was positioned through the holder lumen and up to the proximal end of the occlusion inside the vessel. The catheter length was usually 135 cm, except for few rare occasions where shorter catheters were used to facilitate manipulation. The catheter was always flushed with water. Upstream of the occlusion and outside the artery holder, the support catheter could be curved and bent in various geometries to better represent human vascular tortuosity. In some cases, the catheter could be replaced by an over-the-wire balloon catheter to increase support.

The crossing procedure is described by the following steps:

1. Insert a commercial guidewire and attempt to cross the occlusion. If successful, discard specimen and start with a new one.
2. If not successful, exchange the commercial guidewire for the active guidewire.
3. Try crossing the CTO using the active guidewire without shock wave energy delivery. If successful, discard specimen and start with a new one.

4. If not successful, try crossing the CTO using the active guidewire with shock wave energy delivery. If required, vary the output power level. Record the crossing rate and observations.
5. Once across the CTO, try advancing the support catheter over the active guidewire and through the CTO and record observations.

After the crossing procedure, the CTO segment was dissected for further analysis. This step was used to better assess the composition of the occlusion and the recanalization path. At the end of the procedure, all biological tissues were discarded according to standard method for biohazard materials.

3.2.6 Endothelial cell viability study protocol

The objective of this study was to evaluate the effect of delivering shock waves inside live ex-vivo healthy pig arteries. Safety was assessed by evaluating endothelial cell viability and arterial wall damage. A commercial CTO guidewire was also used as the control article for comparison. This research was approved by the animal ethics committee of the Sherbrooke University Hospital (CHUS).

Fresh coronary (N=6) and carotid (N=8) arteries segments (about 10 mm in length) were sampled from two pigs within 20 minutes of animal sacrifice. The arteries were kept alive and preserved on ice in a Dulbecco's Modified Eagle Medium (DMEM) solution with 10% fetal bovine serum (FBS) and 1X penicillin streptomycin (Pen/Strep). Coronary arteries were randomly harvested from the three main coronary arteries (left circumflex, left anterior descending or right coronary) without distinction. Carotid arteries were harvested from one of the common carotid arteries.

The control guidewire was a MiracleBros 12 from Abbott Vascular (Santa Clara, United States). Active guidewire configuration and console generator settings are described in section 4.2. Three test groups were randomly created among the artery samples:

- group I was exposed to the control guidewire (N=1 coronary and N=2 carotid segments);
- group II was exposed to the active guidewire and shock waves energy delivery. The active guidewire was positioned in the vessel lumen (N=2 coronary and N=4 carotid segments);
- group III was exposed to the active guidewire and shock waves energy delivery. The active guidewire was positioned against the vessel wall (N=1 coronary and N=2 carotid segments).

Within one to two hours after harvesting the arteries, each segment was exposed to either the test or the control device for about 4.2 min (about 2500 pulses at a repetition rate of 10 Hz). Figure 3.13 shows the custom bench setup used for this test. The setup consists of a small tank having a silicon rubber pad in the bottom. This pad was used to fix the artery samples with needles. The outer wall of the artery was pinned to minimize vessel trauma. The tank was then filled with the DMEM solution. Two grooves were added on the wall of the tank to insert and secure two devices during testing. The test and control articles were inserted inside a pre-positioned short introducer. Most of the device length was in air. The devices were slowly introduced inside the artery segment and their distal tip was positioned at about mid-length of the vessel. During exposure, the distal tip of the devices was slowly moved back and forth by about 2-3 mm. In group III, in order to expose the active guidewire to the arterial wall, a bend (between 30° and 45°) was created when pinning the artery. This is shown with the left artery segment on the bottom image of figure 3.13. The active guidewire and commercial guidewire were cleaned with 70% isopropanol pre-soaked wipes in between each artery samples to avoid cross-contamination.

After exposure, the artery segments were incubated at 37°C with 5% CO_2 for a period of 6 hours. Following that period, they were preserved in 10% formaldehyde solution. Dr Sirois and Dr Tanguay's histology laboratory processed the artery samples according to standard procedures. Using common methods, the artery cross-sections were stained with Hematoxylin and Eosin (H&E) and marked for platelet endothelial cell adhesion molecule (PECAM-1), also known as cluster differentiation 31 (CD31), using immunohistochemical staining. The lumen circumference and the total length of the luminal border staining positively for PECAM-1 expression were measured for each cross-section. Vessel wall damage (dissection) was also evaluated. Endothelial cells viability was evaluated as the percentage of vascular lumen covered by endothelial cell staining positively for PECAM-1 relative to the vessel lumen circumference [47].

3.2.7 Acute healthy animal study protocol

The goal of this study was to assess the feasibility to deliver shock waves via the active guidewire in-vivo in coronary arteries. Preliminary data about handling performance of the active guidewire and acute safety were also documented as part of this acute healthy animal study. This study was performed at the Montreal Hearth Institute (MHI) and its animal ethics committee approved this study.

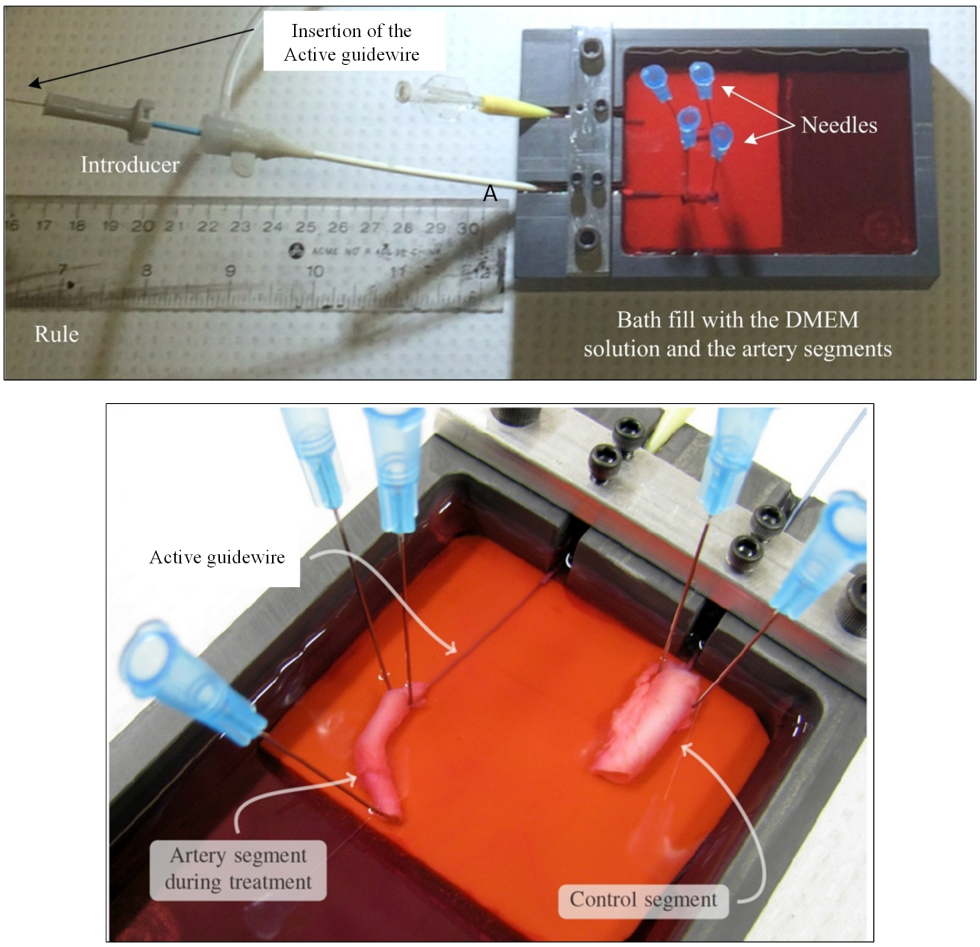

Figure 3.13 Custom bench test setup used to pin the artery segments and insert the test and control devices (bottom image left segment is part of group III and bottom image right segment is part of group I)

Feasibility was evaluated by the ability of the device to reach the target vessel within the coronary arteries and to deliver shock waves with no or minimal effect on the health of the animal. Handling performance was assessed by evaluating the active guidewire compatibility with the support catheter and its visibility under fluoroscopy. Acute safety of the device was evaluated in-vivo. During the procedure, cardiac events assessed on ECG, perforation visible on angiography and any other adverse events were documented. In addition, a method using acetylcholine (Ach) injection followed by quantitative coronary angiography (QCA) was used to evaluate, in-vivo, potential damage caused to endothelial cells exposed to shock waves energy [46]. It was hypothesized that vasoconstriction response of the vessel relative to various acetylcholine concentrations may be used to assess in-vivo damage to the endothelium [201]. Acute vessel injury was also assessed by histopathology on the treated vessels harvested following animal sacrifice. Figure 3.14 shows the catheterization lab from the MHI's research center used during this animal study.

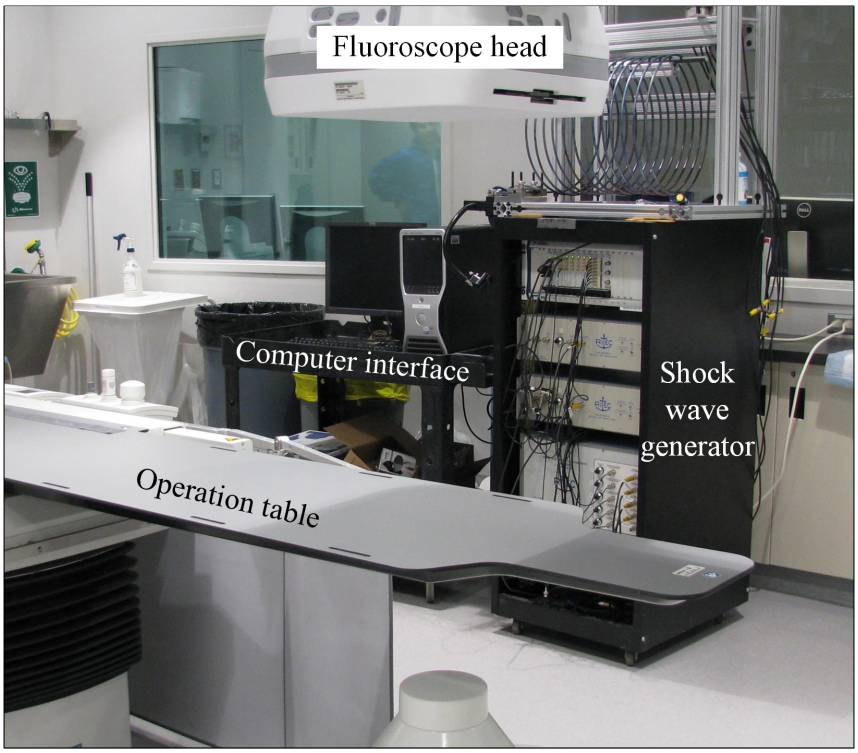

Figure 3.14 Catheterization lab used during the animal study

Three (N=3) healthy juvenile farm pigs (about 3 months of age and about 25 kg) were used for this study. A non-atherosclerotic swine model was chosen because such model has been used extensively for angioplasty and related device evaluation studies, and because of its correlation to human vascular response [69, 166].

Twelve hours prior the procedure, the animals were pre-treated with Aspirin 320 mg x 1 dose and Nifedipine 30 mg x 1 dose. Fifteen minutes prior to general anesthesia, Telazol (6 mg/kg) and Atropine (0.05 mg/kg) were administered intra-muscular (IM). During the procedure, the animals were maintained under general anesthesia with isoflurane 3%. Continuous hemodynamic monitoring (blood pressure, heart rate and electrocardiograms) was performed during the procedure. Temperature was measured at different time points to prevent hypothermia. A bolus of 300 mg/kg of lidocaine and 300 U/kg NH heparin were administered and the ACT was maintained >300 s during the procedure.

Two access sites, one per femoral artery, were created. The right coronary artery (RCA) was cannulated with a guiding Judkins right type 4 (JR4) 6 Fr. The left coronary artery was cannulated with a guiding Amplatz right type 2 (AR2). Each guide catheter was introduced through either femoral artery. Coronary angiograms were performed with an Artis zee machine from Siemens (Germany) while injecting of 5-10 cc of intracoronary

contrast (Visipaque, GE Healthcare). Angiograms were saved when needed at different procedure steps.

A Balance Middleweight (BMW) guidewire from Abbott Vascular (Santa Clara, United States) was used to selectively access the coronary artery to be tested. A single-lumen over-the-wire Maverick balloon 1.5 mm diameter catheter from Boston Scientific (Marlborough, United States) was advanced over the BMW guidewire. Then, the BMW guidewire was exchanged for the active guidewire. The single-lumen balloon catheter was pulled back by 10-20 mm in the coronary artery, leaving the tip of the active guidewire exposed in the lumen of the artery. In some cases, the active guidewire was axially moved within the artery, while in other cases the active guidewire remained stationary. Different shock wave amplitude levels were delivered by the active guidewire at different locations of the coronary arteries and at a repetition rate of 10 Hz for about 4 min (2500 pulses). Treatment sites in the coronary artery were identified using anatomical landmarks (e.g. side branches). Active guidewires with different tip geometries (round versus square) were also used. Table 3.3 summarizes the different treatment sites per animal, along with the tip geometry, tip movement condition and shock wave amplitude level. A total of twelve (N=12) artery segments were treated or used for evaluation. Detailed active guidewire configuration and shock wave generator settings are described in section 4.2. Observations were recorded along the procedure about the technical handling performance of the active guidewire and about the device safety. The procedure was performed by Dr Tanguay, an experienced PCI operator.

After treatment and before the selective injection of Ach, the guidewire was pulled out of balloon catheter. Ach was injected through the single-lumen balloon catheter at various concentrations (10^{-7} mol/l, 10^{-6} mol/l, 10^{-5} mol/l and 10^{-4} mol/l) for 3 min each at a rate of 1 ml/min [46]. Immediately after injection of the highest concentration of Ach, 100 μg of nitroglycerin (nitro) was administered via the balloon catheter. QCA was performed to measure the vessel diameter at baseline, between each injection of Ach and after injection of nitroglycerin with the same protocol performed for all treatment sites. QCA was performed with Artis Syngo software from Siemens (Germany). Each segment measurement was performed in end-diastolic frames.

Following the procedure, the animals were sacrificed under general anesthesia. Gross necropsy of the heart was performed. All treated segments of the coronary artery were explanted, as well as the side branches. Tissue sections of 5 mm were placed into formalin, followed by paraffin embedding. Slices of 6 μm thickness were prepared and stained with H&E and CD31 (endothelial cell immunostaining). The lumen circumference and

Table 3.3 Active guidewire configuration and console level used per treated artery

Animal	Artery	Tip movement	Tip shape	Console level (%)
1	LAD - Mid	Yes	Square	100
1	LCx - Mid	Yes	Square	100
1	RCA - Mid		(control artery)	
2	LAD - Prox	No	Square	75
2	LAD - Mid	No	Square	0
2	LAD - Distal	No	Square	0
2	LCx - Mid	No	Square	75
2	RCA - Prox	No	Square	50
2	RCA - Mid	No	Square	0
2	RCA - Distal	No	Square	0
3	LAD - Distal	No	Round	75
3	LCx - Mid	No	Round	75
3	LCx - Distal	No	Round	0

LAD = left anterior descending artery,
LCx = left circumflex artery,
RCA = right coronary artery,
Mid = middle and
Prox = proximal

the luminal border staining positively were measured for each cross-section. Histology processing and evaluation were performed by the laboratory of Dr Sirois and Dr Tanguay. The percentage of endothelial cells expression (i.e. cell viability) was calculated as the ratio of cells staining positively against the lumen circumference.

CHAPTER 4

RESULTS

This chapter presents the final design of the proposed CTO crossing system, its different components and its principle of operation. Following that, preliminary efficacy and safety performance results that were obtained with the proposed CTO crossing system are presented.

4.1 CTO crossing system

The design philosophy behind the proposed CTO crossing system was the following: (i) generate, (ii) amplify and (iii) deliver large amplitude mechanical waves (shock waves) up to the diseased vessel. The proposed CTO crossing system has two main components: (i) the shock wave generator (also called the console) and (ii) the active guidewire. The console is used to generate and amplify the mechanical waves, while the active guidewire is used to transmit and deliver these waves at the CTO. One way to produce these mechanical wave, within the console, consists of exploiting the dispersive property of a solid cylindrical waveguide (rod) and the time reversal technique [43]. To do so, it is appropriate to use a broadband piezoelectric transducer. However, such a transducer is usually limited in term of displacement amplitude and energy output. Therefore, it was proposed to combine the effect of multiple discrete broadband piezoelectric transducers. To do so, the concept of a spatial concentrator, an acoustic mirror shaped with a parabolic surface, was added prior to the dispersive waveguide. Figure 4.1 shows a flowchart with the associated components of the shock wave generator. To deliver the resulting shock waves at the CTO, it was proposed to use an elongated and flexible metallic wire, called the active guidewire, that is compatible with current endovascular equipment and technique.

Within the shock wave generator, digitized waveforms are first loaded via a computer interface. These waveforms are obtained from a system calibration procedure that is done only once prior to emission. [redacted]. A digital-to-analog converter (waveform generator) is used to convert the digitized waveform into analog signals. The low voltage analog signals are amplified using electrical amplifiers. The resulting high voltage signals are used to drive the piezoelectric transducers. These piezoelectric transducers convert the electrical energy into mechanical energy. The result-

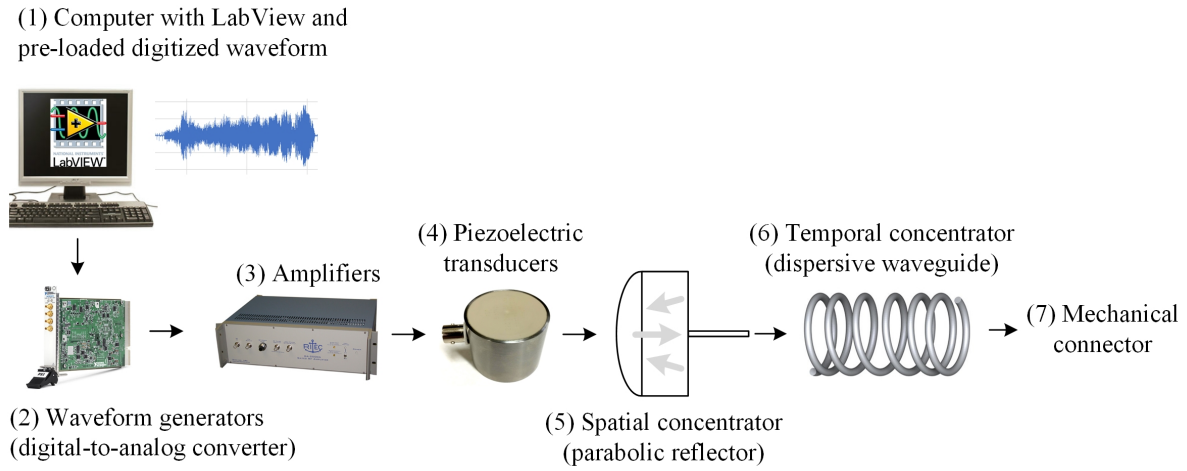

Figure 4.1 Flowchart representation of the shock wave generator

ing train of mechanical waves travel inside the parabolic reflector (spatial concentrator) to be spatially combined near the proximal end of the dispersive waveguide. The spatially combined train of waves travels within the dispersive waveguide (temporal concentrator) and is temporally compressed to form one single large amplitude and short duration mechanical wave (i.e. shock wave) at the opposite end. The dispersive waveguide is a rod that is coiled to reduce its footprint. A mechanical connector is used between the console and the active guidewire to ensure transmission of the shock wave. Figure 4.2 shows an overview of the actual shock wave generator.

At the proximal end of the active guidewire, a part called the section reducer, is used to ensure proper coupling between the dispersive waveguide and the core wire. A laser weld is used to join the section reducer to the core wire. The core wire is small, flexible and long enough to fit into a commercial support catheter. The active guidewire was designed to mimic current commercial guidewires. To achieve this, the core wire is ground near its distal end which increases its flexibility and provide a less traumatic tip. A radiopaque marker is added at the distal tip of the active guidewire to provide visibility under fluoroscopy. One or more coatings may be added over the core wire and the radiopaque marker to improve lubricity when advancing the active guidewire inside the support catheter and the artery. Examples of such coatings are polytetrafluoroethylene (PTFE) and hydrophilic coating. Figure 4.3 presents an overview of the actual active guidewire.

The next subsections present in greater detail each of the sub-systems introduced above.

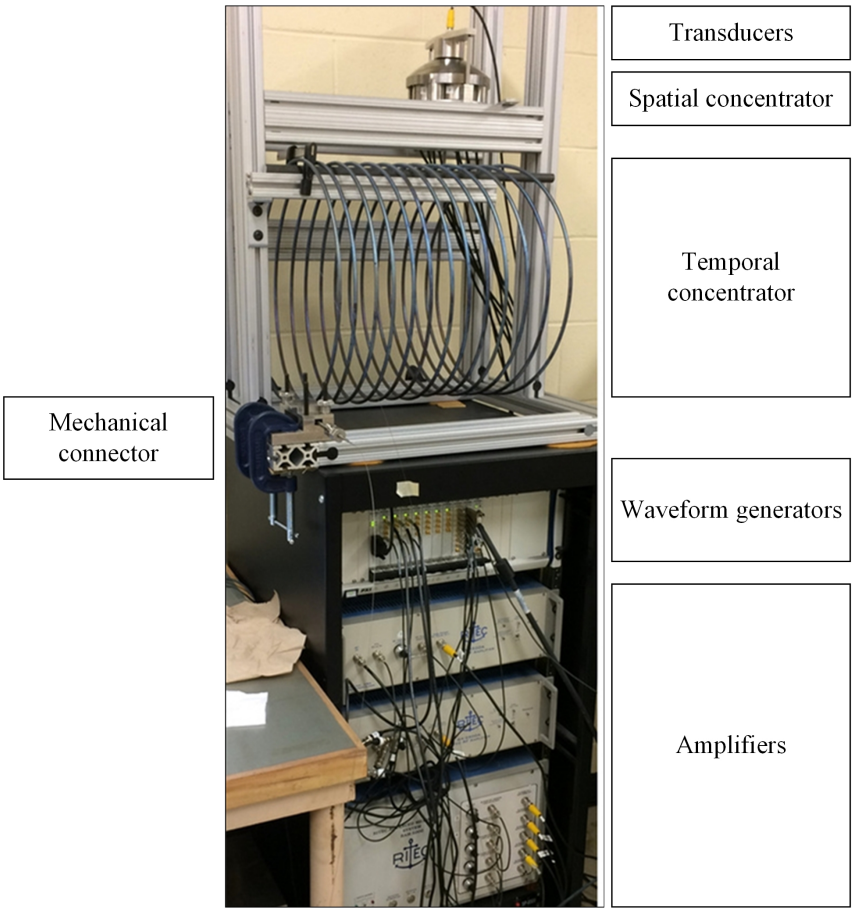

Figure 4.2 Overview of the shock wave generator (computer interface not shown)

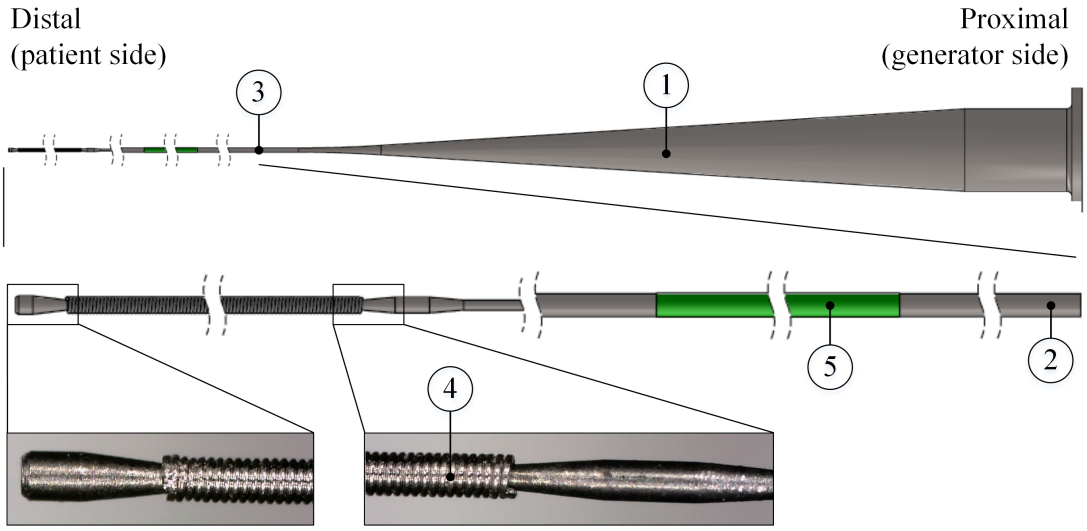

Figure 4.3 Active guidewire overview (1: section reducer, 2: core wire, 3: laser weld, 4: radiopaque marker and 5: coating(s))

4.1.1 Shock wave generator (console)

The following paragraphs describe the different components of the shock wave generator. Their order of appearance is associated with the design strategy that was adopted. For example, it is important to select the transducer key properties (center frequency and bandwidth) before designing the dispersive waveguide or selecting the driving electronics. In the proposed design, a total of nine (9) piezoelectric transducers are used in combination with a seven (7) channels power amplifier and three (3) waveform generators, as shown in the schematic on figure 4.4. Such a configuration was proposed since it takes advantage of the system's geometry and the size of the different transducers for optimal performance.

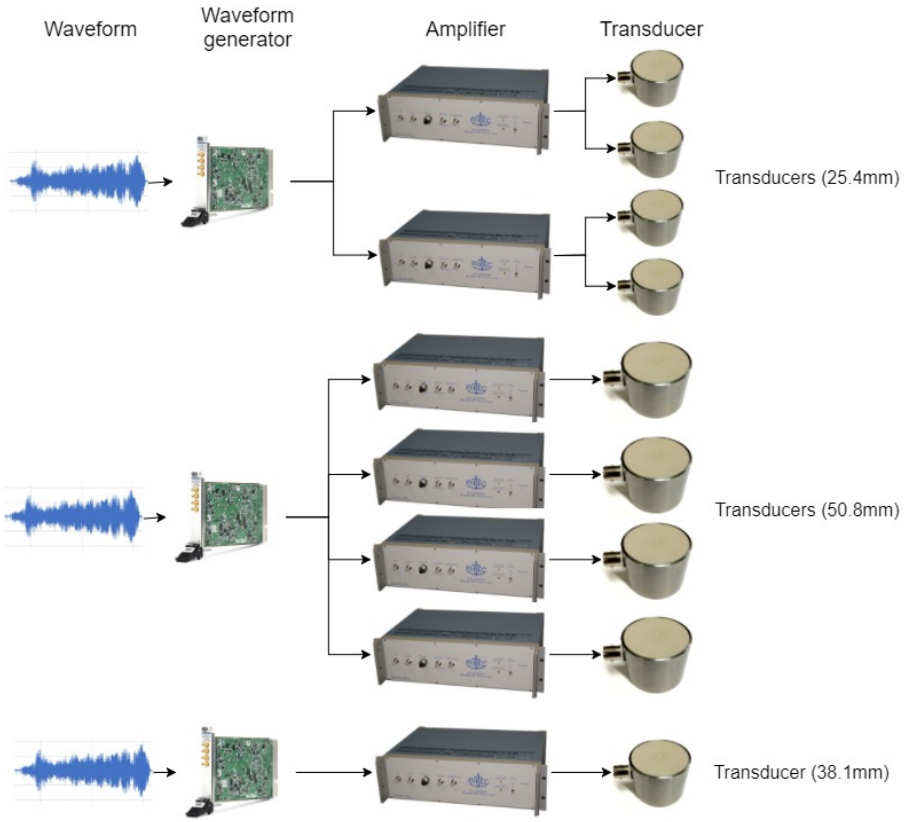

Figure 4.4 Shock wave generator wiring diagram

Piezoelectric transducer

The optimal design would consists of using one single large and focalized transducer to create the mechanical waves. However, such a custom made transducer can be expensive and difficult to mechanically couple to the solid dispersive waveguide. Instead, nine (9) off-the-shelf circular and flat gas matrix piezoelectric (GMP) transducers from Ultran Group (Houserville, United States) were used in the proposed system. Such configuration is less complex to design, fabricate and is less expensive. Also, in case of failure, it is

easier to replace one small inexpensive transducer instead of one large expensive focalized transducer. Moreover, flat transducers most likely excite compressional (longitudinal) modes. This is important since this is the kind of mode exploited by the dispersive waveguide.

GMP transducers are composed of many small piezoelectric pillars that are surrounded by gas [32]. These are similar in design to piezocomposite transducers, but instead of using epoxy in between a piezoelectric pillars, gas is used. As with other transducers, the thickness of these pillar dictates the center frequency of the transducer. The pillars are bounded by two electrodes (one at the bottom and the other on top). A backing (epoxy doped with dense particle material) can be added on the non emitting face and one or more coupling materials can be added on the emitting face.

In the proposed design, each transducer has a center frequency of about [redacted] and a bandwidth of about [redacted], defined as the frequency bounded by the -6 dB region relative to the center frequency. These transducers have a titanium coupling face, a stainless steel casing and a BNC connector (on the side or at the top). Transducers of different sizes were used: four 25.4 mm in diameter, four 50.8 mm in diameter and one 38.1 mm in diameter. The number and size of transducers were selected such as to optimize the active surface coverage over the parabolic reflector (see section below). An example of such a transducer is shown on figure 4.5.

Figure 4.5 Example of a 50.8 mm diameter Ultran transducer

Advantages of a GMP transducer are its low acoustic impedance, large bandwidth and high conversion efficiency. The acoustic impedance of the transducer is an important property to consider in order to improve transmission efficiency in the target medium (parabolic reflector). The closer the acoustic impedance of the transducer is to the target medium, the higher the transmission level will be. As mentioned before, considering the use of the time reversal method with a dispersive waveguide, large bandwidth waveforms are required to achieve high amplification gain. Indeed, the larger the

bandwidth, the more frequency components can be dispersed and the more mechanical waves can be added up during emission. Conversion efficiency of different piezoelectric transducers was assessed in a pulse and catch test. In this experiment, it was demonstrated that a GMP transducer produced a higher amplitude signal when compared to a piezocomposite (PCO) and a piezoceramic (PCE) transducer of the same size and of the same centered frequency. For this test, a center frequency of 1 MHz was used. A block of aluminum was used between the emitting and the receiving transducer.

This test was realized by Ultran Group and is summarized in table 4.1 [200]. For these reasons, GMP transducers were favored for this system.

Table 4.1 Pulse and catch tests comparing different transducer technologies in an aluminum block (GMP = gas matrix piezoelectric, PCO = piezocomposite and PCE = piezoceramic)

Emitter	**Receiver**	**Receiving peak-to-peak amplitude** (V)
GMP	PCE	3.09
PCO	PCE	1.84
PCE	PCE	2.03
PCE	GMP	2.17
PCE	PCO	1.70
PCE	PCE	1.58

Temporal concentrator (dispersive waveguide)

The dispersive waveguide consists of an elongated metallic rod. One end is connected by a weld to the spatial concentrator and the second end is connected to the mechanical connector. Its diameter and material are selected in order to optimize dispersion. A rod made of titanium alloy Ti-6Al-4V and with a radius of about [redacted] was used for the temporal concentrator. This alloy was selected for the following reasons: (i) biocompatibility, (ii) mechanical strength, (iii) accessibility and (iv) acoustic transmission properties. Even though the dispersive waveguide is not in direct contact with the human body, it is understood that the ideal situation is to use the same material across the dispersive waveguide, parabolic reflector and active guidewire in order to minimize losses from acoustic impedance mismatch. Mechanical strength is also important since the resulting shock waves may reach amplitudes high enough to break the transmission material (e.g. by fatigue).

Using, as reference, the center frequency of the GMP transducers; [redacted] (refer to section 4.1.1), and assuming a longitudinal wave velocity c_0 in a rod of about 5040 m/s for titanium Ti-Al-4V (refer to table 2.2), the corresponding wavelength λ_0 is about [redacted]. This gives a frequency-radius combination of about [redacted], which is within the ideal range proposed in section 2.3.5. Referring to section 2.3.5 and more specifically to figure 2.15, it is seen that at this frequency-radius combination, the first and second longitudinal modes (L(0,1)and L(0,2)) along with the first flexural mode (F(1,1)) will propagate in the waveguide.

The dispersive waveguide final length is about [redacted]. The waveguide is coiled to obtain a final radius of curvature of about [redacted]. Figure 4.6 shows an example of the dispersive waveguide. The temporal concentrator was coiled to reduce its footprint and for assembly convenience. In vacuum (or in air), when the radius of curvature is large compared to the center wavelength of the waveform, its effect on wave propagation is negligible [202]. In the proposed design, the radius of curvature is about 20x the wavelength. The length of the dispersive waveguide was selected to provide the best compromise between the dispersive gain and the dissipation losses. Indeed, above a certain length, the dissipation lost from the medium overcome the dispersive gain. The optimal length was found experimentally to be around [redacted] for the proposed system.

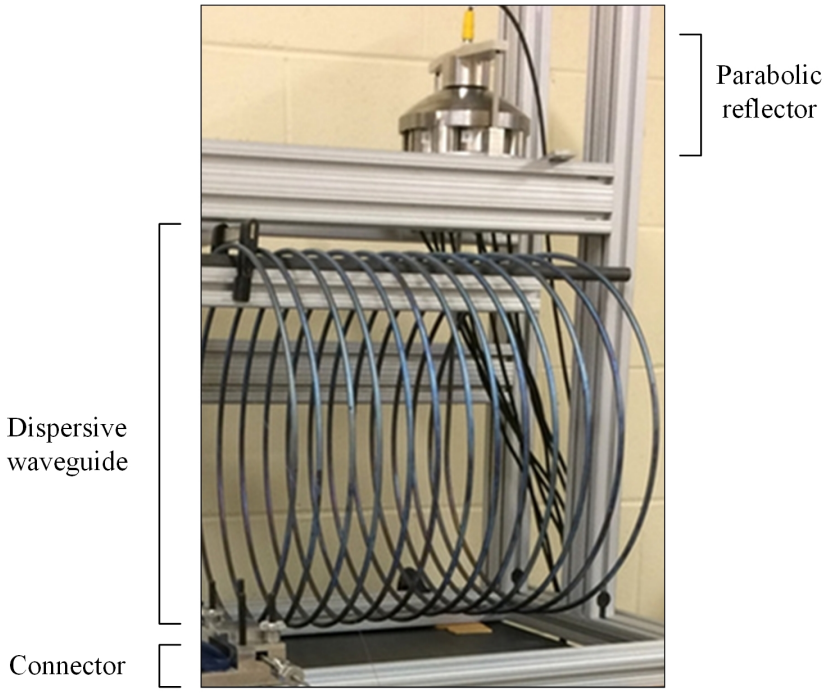

Figure 4.6 Temporal concentrator (dispersive waveguide)

Considering the complexity to supply a single [redacted] long rod, the dispersive waveguide was made from [redacted] rods, each having a length of about [redacted]. Each rod was individually bent to obtain a final radius of curvature of about [redacted]. A straight segment was kept on the first and last rods to facilitate assembly with the spatial concentrator and the connector. The bent rods were TIG welded together using a custom-made jig and welding process. The welding process was developed to ensure a sound weld free of contaminants and defects. For example, argon gas shielding is crucial when welding titanium to avoid any oxidation which may weaken the weld. On the connector side of the dispersive waveguide, a short rod with a flange was welded. Following welding and coiling, a stress-relief heat treatment was applied to the dispersive waveguide. The stress-relief heat treatment consists of heating the coiled and welded rods in a furnace at around 600°C for 1-2 hours followed by slow air cooling [61]. This heat treatment was applied to relief stresses from the cold work and welding.

The waves traveling in the dispersive waveguide are highly sensitive to boundary conditions. Any contact on the surface of the waveguide can impact the traveling waves (reflection, absorption, leakage, etc.). To avoid potential loss, the dispersive waveguide must be lightly secured in place. This is better achieved by supporting the temporal concentrator with few small contact points. For example, in figure 4.6, the dispersive waveguide is mostly free and its weight is supported by a horizontal beam.

Spatial concentrator (parabolic reflector)

The concept of a spatial concentrator was implemented to combine the output from multiple discrete piezoelectric transducers. At first, different configurations were proposed, simulated and tested. For example, a phased array, a hemispherical solid medium with discrete transducers and an acoustic lens configurations were simulated or tried to combine and focus the train of waves from many transducers. At the end, the concept of a parabolic reflector was selected for the reasons listed below.

The proposed design of the parabolic acoustic mirror is shown on figure 4.7. On the images, the circular piezoelectric transducers are mounted on the top face and arranged such as to optimize the active surface coverage. For easier understanding, only two 50.8 mm and two 25.4 mm transducers positioned on the top face are shown on the left picture of figure 4.7. At the bottom of the parabolic reflector, a parabolic shape is machined. Additionally, one extra transducer (38.1 mm) is mounted on the bottom face. This transducer is aiming directly toward the focal point of the parabolic reflector. The thick arrows on the left image of figure 4.7 illustrate the path followed by the emitting waves. The key is to have

all these waves converging toward the geometrical focus of the parabolic reflector at the same time. The transducer on the bottom surface was added to improve the overall gain of the parabolic reflector. Indeed, looking at the simulation results, it was found that the center region of the parabolic surface was not significantly contributing to reflect the incoming waves from the top eight transducers. It was later confirmed experimentally that the bottom transducer improved the overall performance of the parabolic reflector. The right panel of figure 4.7 shows the actual parabolic reflector with the piezoelectric transducers mounted on it.

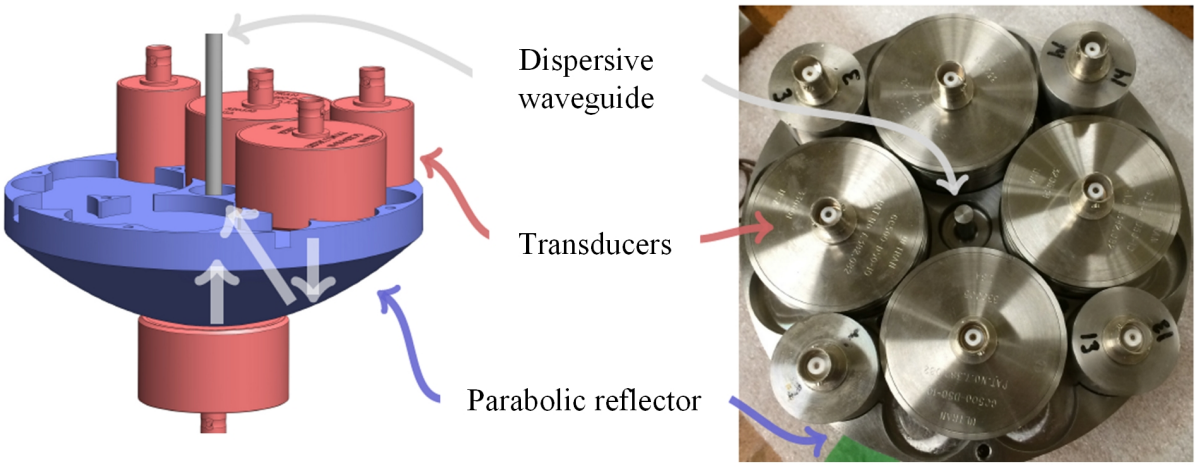

Figure 4.7 Parabolic reflector concept

The proposed design offers the best compromise between spatial concentration gain, system complexity and ease of fabrication. For example, a parabolic reflector allows the use of many flat off-the-shelf transducers instead of a complex custom focalized transducer or annular transducers required by other configurations. Also, because of its symmetry, the same driving signal can be used for more than one transducer, reducing the need for additional amplifiers and waveform generators. Such configuration is also compact and allows easy access to the transducers.

High concentration gain can be obtained with a parabolic reflector configuration. For that, the following parameters must be take into consideration during design:

- transducer distribution and surface coverage;
- wavelength;
- distance traveled by the waves;
- reflection angle at the parabolic surface.

Ideally, the surface covered by the transducer should be as large as possible, the wavelength should be as small as possible to limit diffraction, the travel distance should be as short

as possible to reduce intrinsic attenuation, and the reflection angle should be such to limit mode conversion into shear waves (refer to section 2.3.2). It is understood that some of these parameters are in opposition and/or are already fixed by other components of the shock wave generator. For example, the thickness of the parabolic reflector will impact both the traveled distance and the reflection angle, but in opposite ways (i.e. a thinner reflector will minimize the wave traveled distance, but will increase the reflection angle). Another example concerns the wavelength which is imposed by the choice of transducer and the medium for the dispersive waveguide and parabolic reflector. To find the optimal parabolic reflector geometry, many finite element simulations were performed and many prototypes were tested experimentally.

The main dimensions of the final parabolic reflector are shown in figure 4.8. The parabolic reflector is made from the same titanium alloy as the dispersive waveguide (Ti-6Al-4V). Both parts were TIG welded together to ensure optimal transmission of the acoustic waves. The same welding process as for the dispersive waveguide was used to join these parts. The transducers are mounted on the parabolic reflector using a system of brackets (not shown). A coupling medium ([redacted]) is added between the transducers and the parabolic reflector during assembly to ensure optimal acoustic transmission. This coupling medium helps create a uniform surface, free of air, between the components.

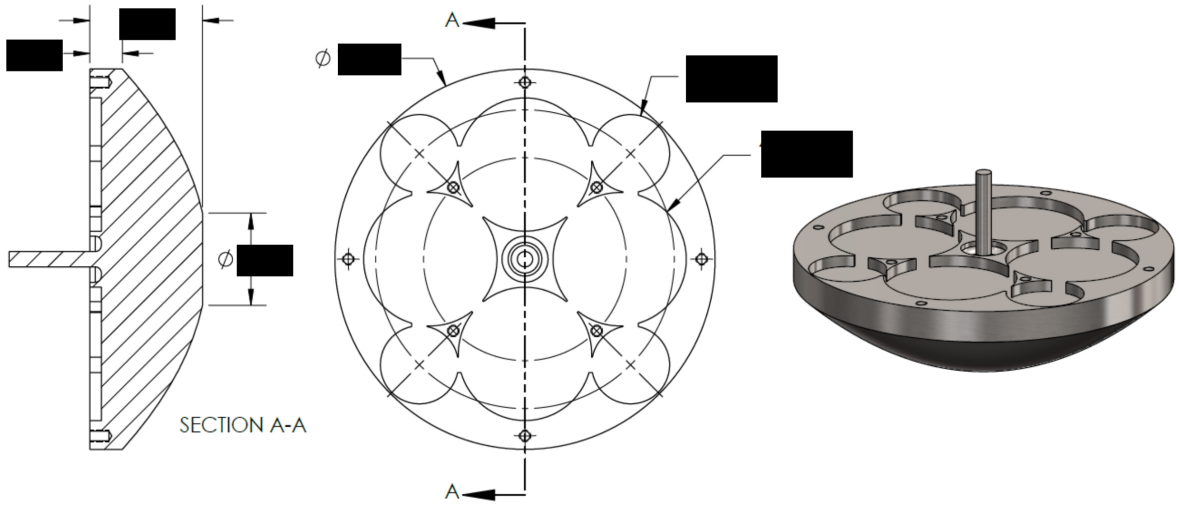

Figure 4.8 Parabolic reflector main dimensions (cm)

Electronics

A computer with LabView is used to control the console. Three pre-loaded digitized waveform are converted to analog signal using PXI-5412 waveform generators from National Instruments (NI) (Austin, United States). The PXI-412 waveform generator (showed in

figure 4.9) has a maximum bandwidth of 20 MHz, a maximum update rate of 100 MS/s, an analogue output resolution of 14 bits, an analog output voltage range of ±6 V and has only one output channel. This waveform generator model was chosen because of its availability, bandwidth and resolution.

Electrical amplifiers are used to amplifier the analog driving signals. Three off-the-shelf high power amplifiers model GA-2500A from Ritec (Warwick, United States) are used. Two of these amplifiers have one output channel while the third has five output channels, for a total of seven channels, as highlighted in figure 4.4. Figure 4.10 shows an example of a Ritec amplifier. Each channel can deliver a maximum of 400 W. Its bandwidth ranges from 40 kHz to 15 MHz. These amplifiers have a 2 % duty cycle and work with an external TTL level gate. The duty cycle limits the repetition rate at which the shock wave generator can be used. These amplifiers use standard 120 V and 50-60 Hz electrical outlet. Maximum output of 1440 V peak-to-peak can be reached, but typical peak-to-peak voltage of 700 V was used to maintain the durability of the transducers. This value corresponds to the 100% console power level referred later. These amplifiers were selected considering their power output level, duty cycle, cost, bandwidth and availability.

Figure 4.9 PXI-5412 waveform generators (from NI website)

Figure 4.10 GA-2500A electrical amplifiers (from Ritec website)

Mechanical connector

The mechanical connector is used to mechanically join the distal end of the dispersive waveguide to the proximal end of the active guidewire (section reducer) using a hollow screw and a nut. As mentioned earlier, a short rod with a flange was TIG welded at the free extremity of the dispersive waveguide. A similar flange is also present at the proximal end of the active guidewire; on the section reducer part. To minimize losses due to contact on the outer surface of the dispersive waveguide, only the flanges are touched during the connection.

Figure 4.11 shows the mechanical connector and its different components. The hollow screw and its bushing were inserted over the dispersive waveguide before welding the flanged part. The nut and its bushing can be slipped over the active guidewire. The bushings are used to facilitate centering of the parts, minimize wear of the mechanical components and reduce acoustic loss. The flanges have a diameter of about [redacted] and a thickness of about [redacted]. The thickness of the flanges is kept as small as possible to avoid loss by diffraction toward the outer diameter. A coupling medium ([redacted]) is added in small quantity between the two flanges during connection to improve transmission. To obtain a good and repeatable connection, a torque wrench with a torque set to about [redacted] is applied during the connection. Considering the design of the mechanical connector, only longitudinal waves can be transmitted across this joint. Flexural waves cannot be transmitted because of the slip condition. Therefore, the flexural waves will be reflected and trapped inside the dispersive waveguide. Since the longitudinal waves are mostly favored in the system, it is not believed that such condition at the connector would impact performance.

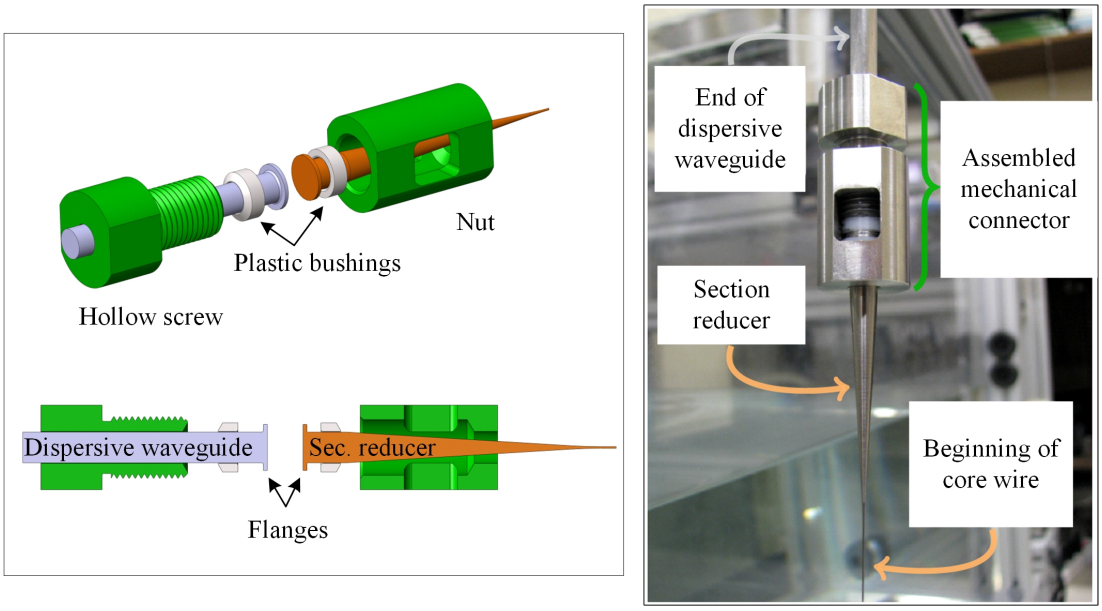

Figure 4.11 Mechanical connector

4.1.2 Active guidewire

The design and construction of the active guidewire are similar to commercial guidewires used in endovascular procedure. The main difference is the fact that the active guidewire can transmit mechanical waves from one end to the other end. This requirement affects the material selection and the arrangement of the various components. Also, contrary to

many commercial guidewires, the active guidewire has a core wire extending up to the very distal tip. As for the dispersive waveguide, the transmission of mechanical waves across the active guidewire is impacted by its boundary condition. Therefore, special design considerations were taken to minimize loss as described below.

Figure 4.3, shown previously, presented the proposed active guidewire design. Its main components are: (i) section reducer, (ii) core wire, (iii) laser weld between the core and the reducer, (iv) radiopaque marker and (v) coating(s). Many design configurations were used for performance testing presented in section 4.2. For example, active guidewires without the radiopaque marker and/or without coating were used. Specific designs will be described for each test. The following sections present each components of the active guidewire listed in figure 4.3.

Section reducer

The section reducer component is used to connect the active guidewire to the console as it was proven to be too complex to connect directly onto the core wire. This component also helps to funnel the acoustic waves from the large dispersive waveguide to the small core wire. Figure 4.12 shows the design of the section reducer. The second larger diameter has the same dimension as the diameter of the dispersive waveguide ([redacted]). In this specific representation, the small extremity has a diameter of about 0.43 mm to be compatible with a core wire of the same size. It is understood that other designs can exist with larger or smaller diameter without significantly impacting the overall section reducer design and performance. The section reducer is made of the same titanium alloy (Ti-6Al-4V) to avoid any acoustic impedance mismatch with the dispersive waveguide.

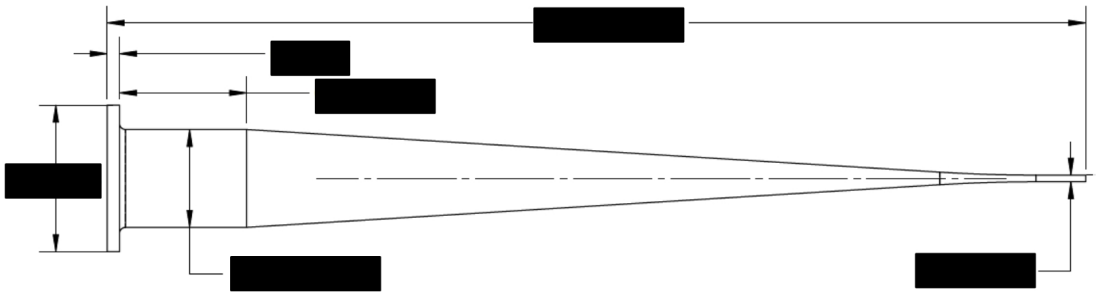

Figure 4.12 Section reducer design and dimensions (in cm)

The section reducer length is [redacted]. A section reducer that is too short will produce a stepper tapering angle and will reflect part of the incoming waves instead of funneling them. A section reducer that is too long will be difficult to machine and does not significantly improve performance. The shape of the tapering section may also affect its ability

to transmit the waves. The proposed length and shape was found based on simulations and experiments, and offered the best compromise between performance and manufacturability.

Core wire material

The core wire material is a critical component of the active guidewire. To select the core wire material, the following criteria were considered:

- biocompatibility;
- acoustic transmission;
- acoustic impedance;
- weldability;
- shapeability;
- resistant to corrosion;
- mechanical properties such as Young's modulus, tensile strength and fatigue resistance.

For reference, table 4.2 lists key mechanical properties of various potential core wire materials. Note that the yield tensile strength property can vary greatly and depends on the amount of cold work and heat treatment applied to the material. Also, Nitinol material is not usually characterized by its Young's Modulus since this parameter varies according to the temperature and strain at which it is tested. However, since it is considered a super-elastic material, it is anticipated that its Young's Modulus is the smallest of the group.

Table 4.2 Mechanical properties of potential core wire materials

Material	**Young's Modulus** (GPa)	**Yield tensile strength** (MPa)	**Reference**
Ti-6Al-4V (grade 5)	114	$\approx$ 880	[118]
Ti-11.5Mo-6Zr-4.5Sn (Beta III) (grade 10)	79	725 - 1600	[13]
Stainless steel 304V	193	330 - 1900	[75]
Nitinol (Ni-46Ti)	Not defined	>1400	[74]

The Ti-6Al-4V alloy was first tried as a potential core wire material. Even though wave transmission was acceptable for short wire length, the intrinsic attenuation was too high for length over 150 cm and mechanical resistance was not sufficient as demonstrated experimentally.

Another option was to use one of the material typically used for commercial guidewires: stainless steel 304V and Nitinol (refer to section 2.2). These materials are biocompatible and offer a good balance between flexibility and mechanical resistance. When tested for wave transmission, intrinsic attenuation in Nitinol was unacceptably high. Nitinol was also found to be more difficult to weld and was discarded from the potential core wire material list [214]. Alternatively, stainless steel showed good wave transmission properties. Stainless steel, as shown in table 4.2, has the highest Young's modulus among the list. This characteristic is important when considering flexibility performance at the distal tip of the core wire, as described later in this section. To achieve similar tip flexibility, the diameter of a stainless steel wire has to be thinner than the to other potential core wire material. This probably explains why conventional guidewires made from stainless steel don't have a core extending up to the distal tip [45]. Moreover, stainless steel has an acoustic impedance that is higher than titanium. This would decrease transmission efficacy between the console and the active guidewire. For these reasons, stainless steel was also discarded from the list of potential core wire materials.

The material selected for the core wire was titanium alloy Ti-11.5Mo-6Zr-4.5Sn, commonly referred as Beta III. This alloy is mainly used in orthodontic appliances [129, 205]. Beta III was proposed as a potential core wire material because it offers mechanical properties between those of stainless steel and Nitinol. Beta III material was originally designed to replace Nitinol with a nickel-free alloy having similar mechanical properties. Biocompatibility of Beta III was not demonstrated, but was assumed based on its specific composition and previous uses. Ultimately, formal biocompatibility tests shall be performed in accordance with the ISO 10993-1 standard and following the recommendations from the associated FDA guidance document [71, 93]. Beta III wire with a diameter of 0.43 mm was ordered from Fort Wayne (Fort Wayne, United States) and tested for wave transmission. Good weldability was achieved (see section below) and good acoustic transmission was demonstrated through experimental tests over length of 300 cm. Since this alloy is mainly composed of titanium, its acoustic impedance is assumed to be similar to Ti-6Al-4V. Using the appropriate amount of cold work and heat treatment, Beta III alloy could reach high values of tensile and ultimate tensile strength. It was also demonstrated that it can be ground using centerless grinding and coated with PTFE and hydrophilic coatings.

Core wire geometry

With the core wire material identified, the next step was to determine the core wire geometry. Key specifications to establish were the following: (i) length, (ii) core diameter, (iii) grind profile and (iv) distal tip geometry. Some of the FDA guidance documents and the

ISO 11070 standard provide useful information about performance handling requirements of guidewires [68, 70, 94]. These requirements were used as guideline for the design of the active guidewire. The following summarizes the key performance requirements that shall be evaluated as specified in these documents:

- joint strength;
- torque strength (defined as the number of turns before failure when the distal tip is being fixed and the proximal end is rotated);
- torqueability (defined as the correlation between rotation of the proximal end and the corresponding rotation of the distal end);
- tip flexibility;
- kink resistance;
- fatigue;
- compatibility with support devices (for example catheter and balloon).

The length of the proposed core wire was fixed at 300 cm. This allows enough length to reach chronic total occlusions located in the peripheral extremities or in the heart while being connected to the console next to the operating table. To fit inside commercial delivery devices, the active guidewire is designed to have the same diameter as conventional guidewires (refer to section 2.2). Therefore, the larger diameter of the core wire was fixed at 0.33 mm and 0.43 mm, depending on the indication for use. These diameters were selected to leave enough room to add coating(s) on it. Interestingly, at these diameters, the active guidewire can be considered almost non-dispersive (i.e. the waveform is not distorted temporally as it is traveling along wire length). Referring to figure 2.15 from subsection 2.3.5 and considering a frequency-radius value of about [redacted] for the active guidewire ([redacted]), it is observed that the waveform is in a region of the dispersion curve where the slope is almost zero, confirming the limited dispersion property.

To gain better insight about how the grind profile and properties of the core wire may affect its handling performance, the following equations are provided and explained.

Torsion of a rod of radius r and length l is defined by equation 4.1, where T is the applied torque, ϕ is the twist angle, G is the shear modulus and I is the second moment of inertia [24]. For a circular rod, the second moment of inertia is equal to $\pi r^4/2$. This formula provides useful indications about the torque response and torsion strength of a wire subjected to a torsional load. For example, the applied torque and twist angle ratio is proportional to the fourth power of the radius. Therefore, a slight increase in wire radius

has a large impact on torque transmission and torsion resistance. Also, the length of the smaller cross-section area shall be kept as short as possible to avoid torque build-up.

$$T = G\frac{I\phi}{l} = \frac{G\pi}{2}\frac{\phi r^4}{l} \tag{4.1}$$

Buckling of a rod of radius r and free length l happens when a critical force F is applied. Such a condition is defined by equation 4.2, where E is the Young's modulus, I is the second moment of inertia and n is a constant defined by the end conditions [24]. This equation provides useful information about the tip flexibility (also referred as tip load or tip stiffness) of a guidewire. A typical tip load test is presented in figure 4.13. Such test is commonly used by the industry to characterize the tip load of a guidewire. The industry uses a standard free distance of 10 mm to measure tip load. Looking at equation 4.2, the required force to produce the buckling of a wire is proportional to the fourth power of the radius. Therefore, a slight increase in diameter greatly increase the tip stiffness of the wire.

$$F = n\pi^2\frac{EI}{l^2} = \frac{nE\pi^3}{2}\frac{r^4}{l^2} \tag{4.2}$$

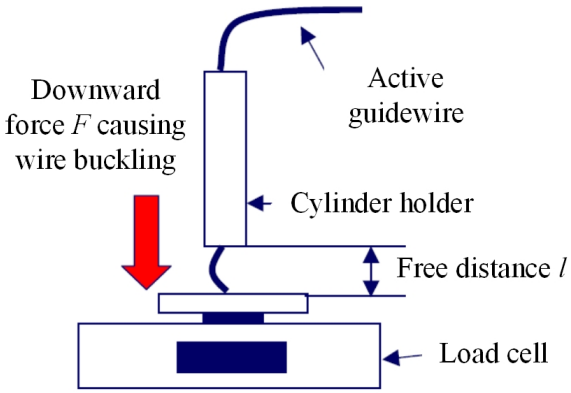

Figure 4.13 Method used to measure guidewire tip load (figure adapted from Asahi [8])

A rod subjected to a three-point bend test, as shown on figure 4.14, will behave as described by equation 4.3, where F is the applied force, w_0 is the downward displacement of the rod at the force application point, l is the distance between the two base supports, E is the Young's modulus, I is the second moment of inertia and r is the rod radius [157]. This equation is similar to equation 4.2 in the sense that both provide insight about the flexural rigidity of a circular beam. However, equation 4.3 is more suitable when evaluating the

overall flexibility profile of the active guidewire as this test may be repeated at different length increments. Again, in equation 4.3, the force to displacement ratio is proportional to the fourth power of the radius. Therefore, a slight change in diameter greatly affects the flexural rigidity profile of the active guidewire. Also, a smaller wire radius will allow larger flexural displacement for the same applied force, which is important for kink resistance.

$$F = \frac{w_0 48EI}{l^3} = 24E\pi\frac{w_0 r^4}{l^3} \tag{4.3}$$

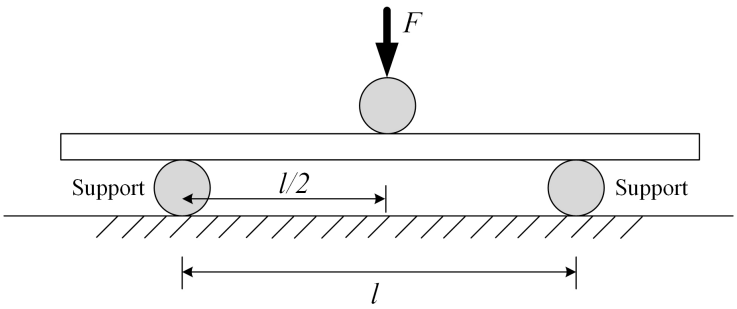

Figure 4.14 Three-point bend test representation

The yield tensile strength σ_y of a rod of cross-section A is defined as the maximum tensile force F it can sustain per surface area before plastic deformation. Equation 4.4 describes this relationship, where r is the radius [24]. The yield tensile strength is defined by the material selection. Therefore, a large radius wire will be able to sustain larger load before plastic deformation.

$$F = \sigma_y A = \sigma_y \pi r^2 \tag{4.4}$$

Looking back at equations 4.1, 4.2, 4.3 and 4.4, it can be observed that to improve torque transmission, torsion resistance, flexural rigidity and tensile strength, a larger wire radius is needed. Also, the larger the distal tip is, the larger the resulting drilled hole will be. Inversely, to improve flexibility and kink resistance, a smaller wire radius is needed. As it is often the case in engineering, these requirements are conflicting and a compromise must be established. To help in the design of the active guidewire, reference CTO crossing devices were studied. In addition to that, multiple iterations were built and feedback from physicians was gathered.

Considering the difference in the vascular beds (vessel size and tortuosity) and compatibility with specialized support devices, a grind profile specific to coronary indication and

another one specific to peripheral indication were proposed. Figure 4.15 and Table 4.3 present the key dimensional characteristics for both active guidewire designs. The specific tapering profile is not shown for simplicity. The coronary and peripheral active guidewires have similar diameters and lengths. The coronary active guidewire has a smaller core wire diameter and a smaller minimal cross-section area near its distal tip. Its ground section length is also longer to accommodate the coronary tortuosity.

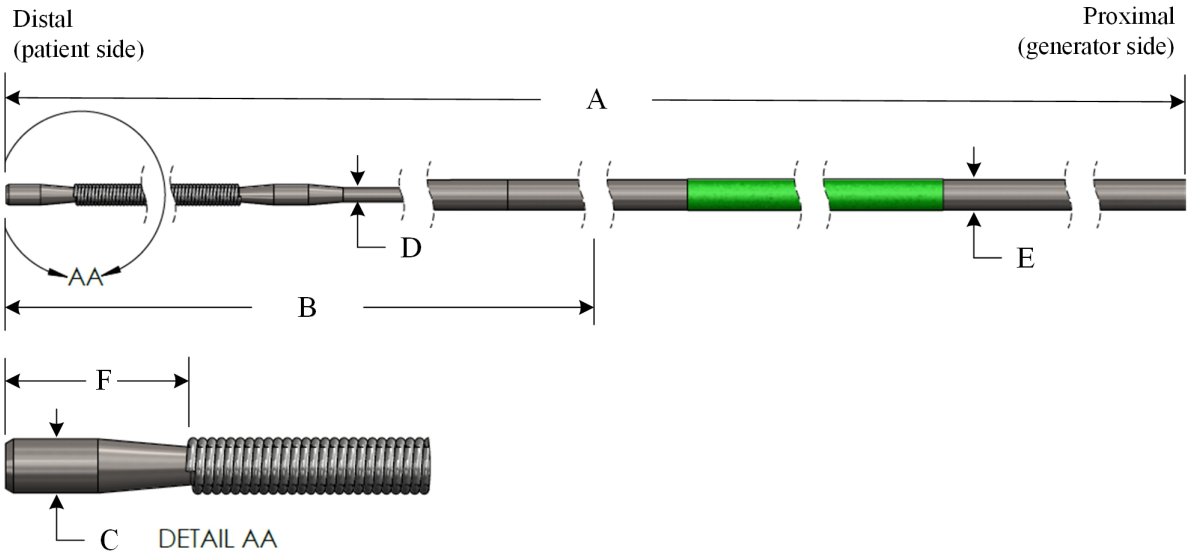

Figure 4.15 Active guidewire grind profile (dimensional information are provided in table 4.3)

Table 4.3 Active guidewire key dimensions per configuration (see figure 4.15 for reference)

Dimensions	Coronary	Peripheral
A: Working length (cm)	300	300
B: Ground section length (cm)	39	15
C: Distal tip diameter (mm)	0.27	0.29
D: Smallest diameter (mm)	0.14	0.20
E: Core wire diameter (mm)	0.33	0.43
F: Length distal to the marker (mm)	0.75	1.00

As shown on figure 4.15, the distal geometry is flat with a small chamfer on the outer edge to be less traumatic on the artery and the support device when advancing the active guidewire. The effect of the tip geometry on performance was not evaluated. Alternative geometries could potentially be used (tapered or round tip). Another key feature of the grind profile is related to the two bumps that are ground in the distal tip region (proximal

and distal to the radiopaque marker). These features are unique to the active guidewire and were added to constrain the radiopaque marker in the axial position. This will be further described in the following subsection. To reduce the likelihood of core wire failure under repetitive activation, the surface roughness of the ground section must be as low as possible and abrupt cross-section variations must be avoided.

Section reducer to core wire laser weld

For optimal transmission of the mechanical waves between the section reducer and the core wire, a weld joint is used. Other mechanical means were envisioned, but none could provide enough joint strength while minimizing loss from the extra boundary condition. Laser welding method was selected over other welding methods (for example electron beam and TIG welding) based on literature review and accessibility [15, 77, 195]. Indeed, laser welding of Ti-6Al-4V introduces less heat and creates faster cooling rate which produces a finer grain structure that is ideal to maintain good mechanical resistance properties.

To the author's knowledge, this represents the first reported case of laser welding Ti-6Al-4V (section reducer) to Ti-11.5Mo-6Zr-4.5Sn (core wire). Different suppliers were subcontracted to produce this weld. Similar results were achieved between all suppliers. None of the suppliers accepted to share their laser welding parameters. Depending on the supplier, laser welding was done with or without addition of a filler material. Both methods provided equivalent results. When filler material was added, Ti-6Al-4V was used as the filler. Figure 4.16 shows an example of the laser weld between the section reducer and the core wire, without addition of a filler material. This picture was taken with a scanning electron microscope (SEM) at a power of 20 kV and a magnification level of 150X. The laser spot welds can clearly be seen overlapping each other. The weld is uniform with almost no necking.

Ideally, contaminants, porosity and surface defects should be avoided during welding in order to produce a sound weld [195]. These could be avoided by using good part preparation procedure (cleaning), inert gas shielding during welding and the appropriate welding parameters (beam diameter, energy, etc.) [61]. Additionally, it was found that post-welding treatment such as mechanical polishing or electropolishing greatly improve fatigue resistance of the weld subjected to fatigue (cyclic load). This finding is still not well understood. It is hypothesized that this post-weld polishing process potentially removes surface defects, residual stresses or other defects, and therefore limits surface crack initiation. Multiple iterations were produced and tested until good weld parameters and post-treatment process were achieved.

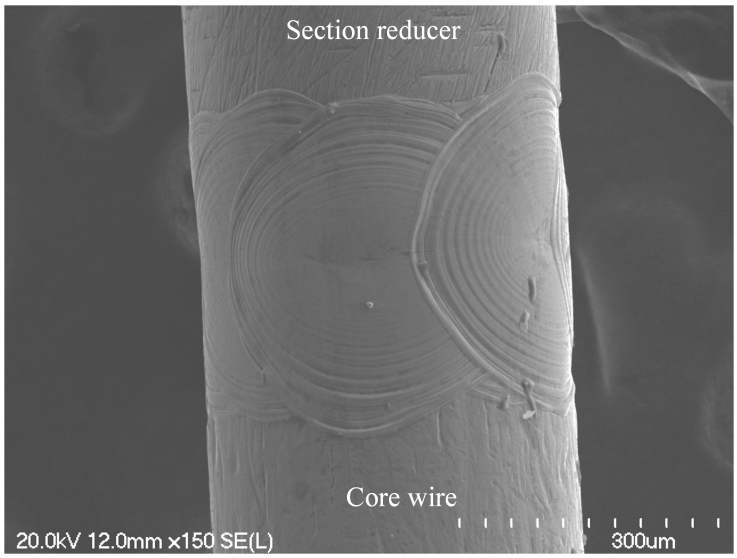

Figure 4.16 Scanning electron microscope image of the laser weld between the section reducer (top) and a 0.43 mm diameter core wire (bottom) (magnification level of 150X)

Radiopaque marker

Radiopacity represents the opacity of a structure to X-ray and is proportional to the thickness and density of the material [173]. For example, because of its density and size, the active guidewire core wire is not radiopaque enough under fluoroscopy to be visible. As it is usually the case with commercial guidewires, a radiopaque marker was added over the core wire distal region.

Typical radiopaque marker materials used by commercial endovascular devices are platinum, iridium, tungsten or gold. Typical radiopaque marker configurations are coil, band, jacket of polymer doped with radiopaque powder, plating and radiopaque ink. Most of these marker materials and configurations were tried for the active guidewire. The main outcome from these tests was that the resulting extrinsic wave attenuation was too large due to the change in boundary condition. However, one promising concept was the coil radiopaque marker. Such design was interesting since the contact area between the marker and the core wire is limited. However, as shown previously in figure 2.6, commercial guidewires usually have a tapering tip that can extend up to the distal end. In such design, a pre-fabricated coil is slipped over the core and is glued, brazed or spot welded in position. A solid distal cap is then welded to cover the distal end of the coil. However, in the case of the active guidewire, it is important that the core wire extends up to the very distal end and that it maintains a sufficiently large surface area to facilitate crossing.

Therefore, the active guidewire has a core wire distal tip that is larger than conventional guidewire, which restricts the possibility to slip a pre-fabricated coil over it.

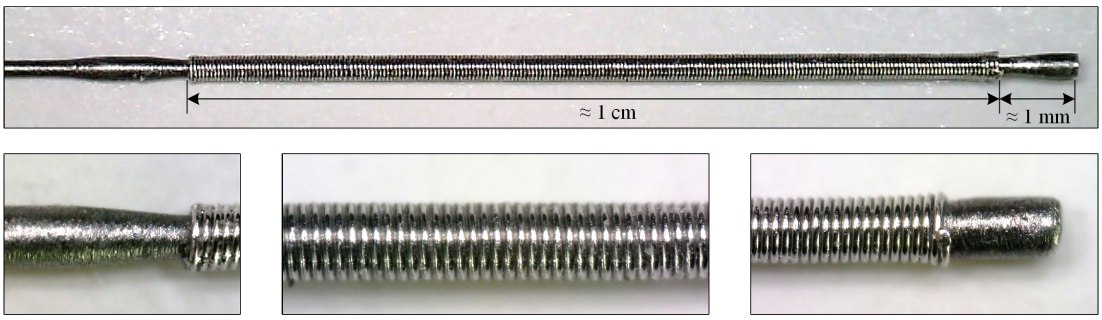

Figure 4.17 Radiopaque coiled over the core wire and betweenthe distal bumps

The proposed radiopaque marker is shown on figure 4.17. This marker is made from a platinum-iridium (90Pt-10Ir) wire having a diameter of 0.051 mm that is manually wound over the core of the active guidewire. A custom process was developed to achieve this operation. The radiopaque marker is coiled in between the two bumps on the core wire. The radiopaque marker length is about 1 cm. The radiopaque marker is free-floating over the core, but is constrained in the axial position by the bumps. To avoid unwinding during use, both extremities of the platinum-iridium wire are laser spot welded to the adjacent ring, as shown on figure 4.18. Radiopacity and durability of this radiopaque marker were demonstrated during simulated testing as described in section 4.2. One inconvenience of this concept is that the marker does not reach the very distal tip of the active guidewire. Therefore, the operate needs to take into consideration that there is about a 1 mm non-radiopaque length in front of the marker. This may be crucial, especially in coronary interventions, where the vessels are much smaller.

Coatings

The proposed active guidewire has two different coatings. Similarly to many commercially guidewires, the active guidewire has PTFE coating (hydrophobic) over most of the un-ground length and hydrophilic coating over the distal end, covering the ground section and the radiopaque marker only. These coatings were mainly added to improve lubricity. Figure 4.19 and table 4.4 present the coating length for each indication. The PTFE coating thickness is less than 25 μm while the hydrophilic coating thickness is about 1-2 μm. PTFE coating was applied by Precision Coating (Hudson, United States) and the hydrophilic coating was applied by SurModics (Eden Prairie, United States). Both companies used proprietary methods and formulation. Both coatings were previously tested and demonstrated to be biocompatible. Prior to coating, the device must be thoroughly

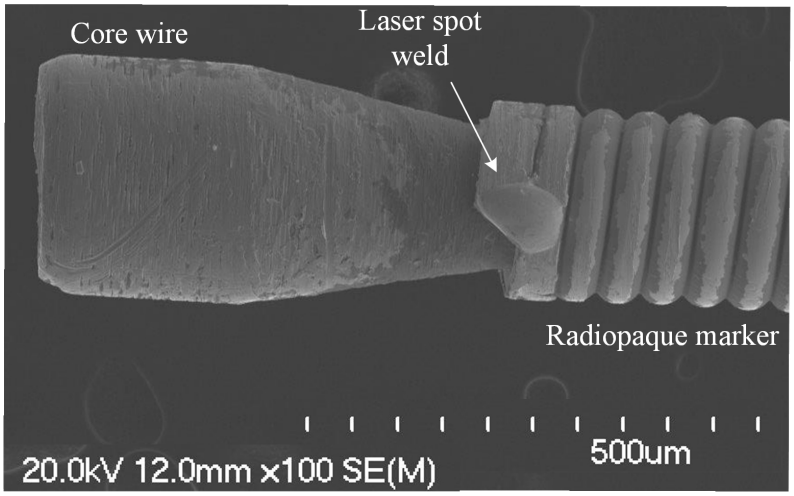

Figure 4.18 Scanning electron microscope picture of the radiopaque marker and distal tip of the core wire (magnification level of 100X)

cleaned. PTFE curing process was done at high temperature. It is important to note that when the curing process is done at temperature [redacted], the titanium alloy core will react with oxygen and create an oxide layer [61]. Hydrophilic coating was applied using a dipping process followed by UV light curing.

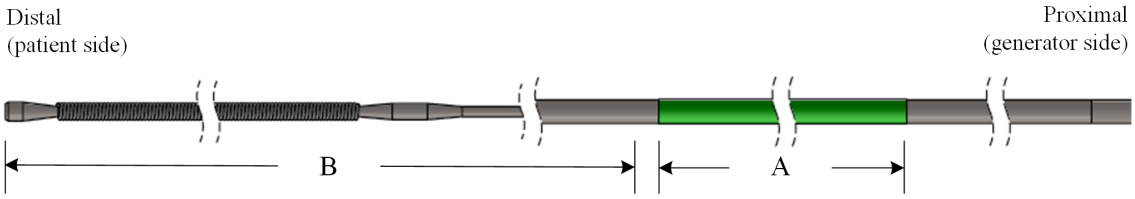

Figure 4.19 Active guidewire coating length (dimensional information are provided in table 4.4)

Table 4.4 Active guidewire coating length per configuration

Dimensions	Coronary	Peripheral
A: PTFE coating length (cm)	200	266
B: Hydrophilic coating length (cm)	39	15

In summary, the key components of the active guidewire are the section reducer, core wire, grind profile, coating(s) and radiopaque marker. The section reducer is used for the connection with the console. Its shape is such to maximize wave transmission from the console to the core wire. The core wire material is Beta III. This titanium alloys has good wave transmission and mechanical properties. The core wire is ground at its distal end to improve its flexibility profile. The core wire is laser welded to the section reducer

at its proximal end. A radiopaque marker is added at the distal end and over the core wire to improve visibility under X-ray. PTFE and hydrophilic coatings may also be added over the core wire and radiopaque marker to improve lubricity. Two designs of the active guidewire were proposed, one for coronary and the other for peripheral indication.

It important to note that at this point, the active guidewire was not cleaned, not sterilized and no packaging was defined. In addition, biocompatibility tests were not performed on the fully assembled devices. Therefore, the final design of the active guidewire may be impacted by the results of these processes and tests.

4.1.3 Operating principle

Figure 4.20 presents an overview of the operating principle of the proposed CTO crossing system. The operating principle is similar to the time-reversal technique, which was previously used in other applications for focusing sound waves through complex and heterogeneous media [67, 125, 185]. The objective of the time reversal technique is to identify which input waveform is needed to drive the transducers in order to create a desired output waveform at the distal tip of the active guidewire. The proposed operating principle has three main steps that are described in figure 4.20. These steps are summarized as the calibration, signal processing and emission.

The calibration step is only done once for a given system. If any components of the system change (for example a transducer), a new calibration is mandatory. The same calibration can be used for different active guidewire configurations as long as their design is similar. During calibration, a square pulse, or a similar waveform, is used to drive the transducers. Each channel from figure 4.4 is calibrated individually. The input signal should have a large bandwidth with a center frequency close to the one of the driving transducers. Considering this, a square pulse with a duration of about [redacted] was typically used to drive the transducers having a center frequency of [redacted]. The waveform emitted by the transducers travels through the system and the resulting dispersed signal is measured at the distal end of the active guidewire. The dispersed waveform is measured with a hydrophone positioned just in front of the tip of the active guidewire using the method described in section 3.2.1. Both the hydrophone and the distal tip of the active guidewire are immersed in water. Since the output pressure waveform measured in water is very weak, the hydrophone must be positioned very close ([redacted]) to the distal tip of the active guidewire. In addition, to remove noise from the dispersed waveform, the calibration procedure may be repeated many times while the dispersed waveform is averaged. A [redacted] recording period with averaging over [redacted] was used for the proposed system.

Figure 4.20 Crossing system operating principle (images are for illustrative purpose only and are not to scale)

The signal processing step is also performed only once for a given system. First, a time window is applied over the dispersed waveform to keep only the useful part of the signal. Typically, only [redacted] of the dispersed waveform is kept. Second, the waveform is time reversed. Optionally, the waveform can be clipped. The clipping process consists to saturate the waveform at a certain percentage of its maximum amplitude. It was experimentally demonstrated that clipping can further improve the amplification gain of the time reversal technique [59, 125, 152]. Clipping works by boosting the high frequency content which may also be detrimental to the transducer durability. Clipping also introduces noise into the signal. Therefore, clipping should be used appropriately. Typically, clipping between [redacted] was applied.

[redacted]

4.2 Performance verification

The safety and efficacy of any new medical technology must be verified. Depending on the medical device class, human clinical trial(s), bench testing and/or animal pre-clinical studies are necessary to support safety and efficacy. These tests are usually established based on predicate devices and applicable standards. Verification tests should also be performed with final devices. The experiments described in section 3.2, with results presented here, were proposed to demonstrate preliminary efficacy and safety of the proposed CTO crossing system. For example, the output pressure measured at the distal end of the active guidewire, crossing ability on surrogate material and on ex-vivo CTOs, viability of endothelial cell exposed to shock waves and results from an acute animal study are presented below. It should be noted that these tests are only meant to demonstrate proof-of-concept. These are not meant, whatsoever, to support any submission filings to any regulatory agencies.

4.2.1 Active guidewire output pressure waveform

The goal of this experiment was to characterize the performance of the system in term of pressure output measured in water near the distal tip of the active guidewire. Calibration waveforms were measured with the fiber optic hydrophone while the pulse waveforms were measured using a needle hydrophone. Method described in section 3.2.1 was followed. All the results presented in this subsection were obtained using the shock wave generator presented above (or similar) at a power level of 100%, unless otherwise mentioned.

The following pressure measurements were obtained using a 300 cm long peripheral active guidewire with a radiopaque marker and PTFE coating. Similar results were obtained with other active guidewire configurations, but are not presented here.

Figure 4.22 shows a typical pulse waveform that was measured at $z = 5$ mm in front of the active guidewire distal tip (at x and $y = 0$ mm). The bottom images shows different zooms of the principal pulse observed on the top image. The waveform was measured over a duration of 10 ms and the central peak was centered at 0 ms. The peak positive pressure p^+ is about 0.20 MPa, the peak negative pressure p^- is about -0.15 MPa and the peak-to-peak pressure is about 0.35 MPa. The duration t_p of the principal pulse and its oscillations is about 30 μs (bottom left image on figure 4.22). Looking at the bottom right image on figure 4.22, the peak pulse half cycle width t_{hc}, defined as the duration between the principal positive and negative peaks, is about 0.25 μs. The peak pulse width t_c,

Figure 4.21 Typical calibration waveform measured near the tip of an 0.43 mm diameter Beta III unground wire, without coating and with no radiopaque marker

defined as the duration between the principal positive peak and the following positive peak, is about 2.15 μs.

Oscillations next to the principal pulse are also observed. In addition, secondary pulses are seen on figure 4.22 at around -1.35 ms, 1.42 ms, 2.85 ms and 4.25 ms. It is hypothesized that these secondary pulses correspond to echoes within the active guidewire (i.e. between the connector and the active guidewire distal tip). Indeed, knowing the theoretical wave velocity in the active guidewire ($c_0 \approx 3950$ m/s, refer to table 2.2) and knowing the length of the active guidewire (about 3 m), the time for a pulse to travel back and forth the active guidewire is estimated to be about 1.51 ms. It is believed that this time delay is sufficiently close to the secondary pulses time delay, accounting for the experimental error and variation of the wave velocity. The first secondary pulse, on the left side of the principal pulse, was probably obtained as part of the calibration procedure described in section 4.1.3. It is suggested that the time duration used for the acquisition of the dispersed signal may be long enough so that it can be reflected at the distal tip of the active guidewire and at the connector interface. The secondary pulses on the right side of the main pulse are echos measured during the emission step. It is seen that their amplitude decreases echo after echo.

Figure 4.23 shows a typical peak-to-peak pressure scan along the z axis measured with the needle hydrophone. The sensor was centered in the xy plane relative to the distal tip

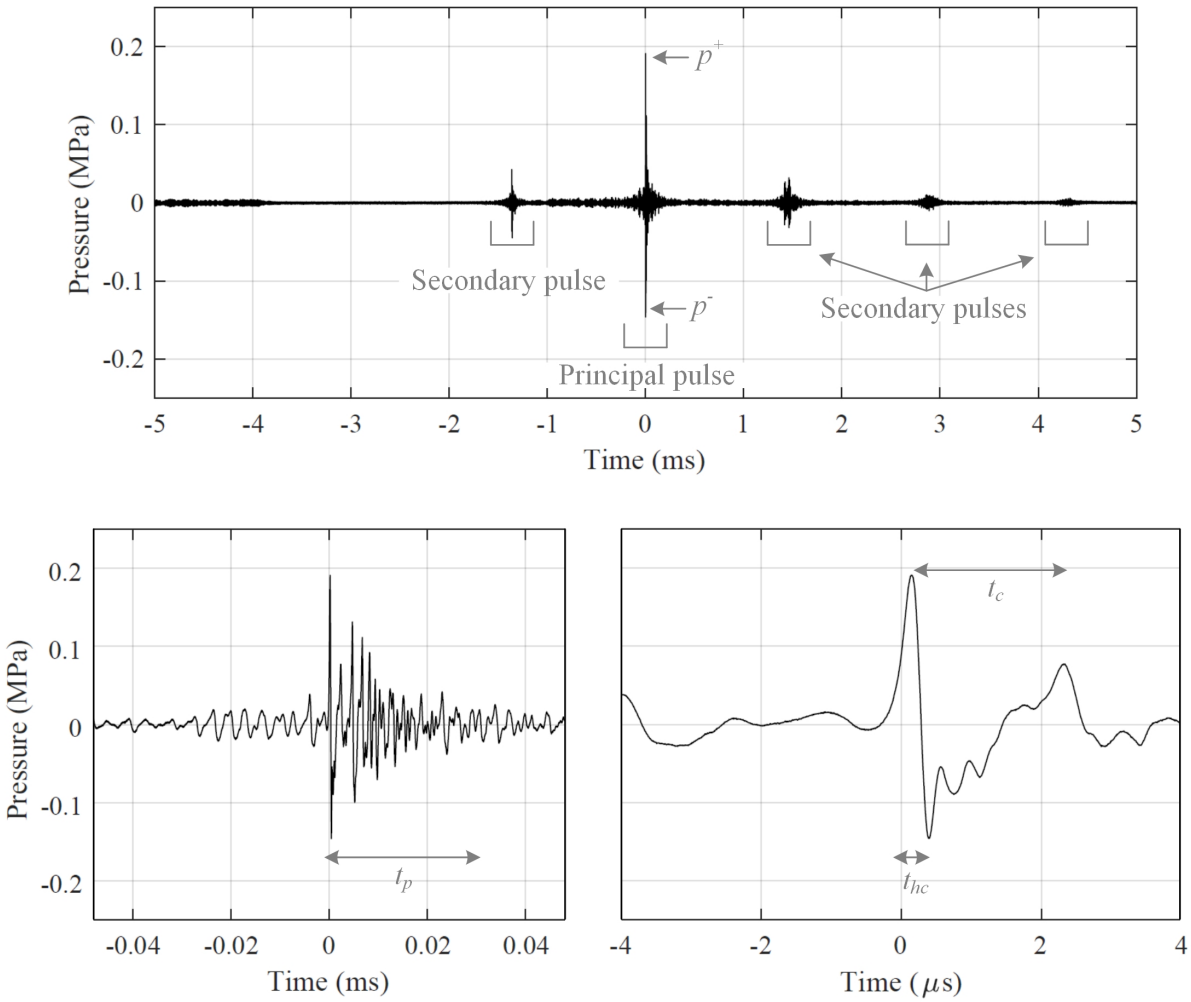

Figure 4.22 Typical pulse waveform measured in water at 5 mm from the distal tip of the active guidewire

of the active guidewire. Each point corresponds to the average of three installations and connections of the active guidewire. For each installation and connection, the average of about 30 measurements was recorded. The error bars represent the standard deviation between the three installations and connections. It is shown that the measurements were consistent and repeatable. Pressure measurement was not done closer to 2 mm since the sensor may be damaged at these distances. It is shown that the pressure is higher near the distal tip and lower as the distance increases from the tip. When adding a trendline to the plot of figure 4.23, it is found that the pressure drops following a distance law close to $1/z$ relationship. Based on that, it is difficult to estimate what is the true maximum peak-to-peak pressure near the tip. However, it is expected that the maximum pressure near the distal tip can reaches value above 1 MPa. In comparison, the pressure output

emitted by high-power low-frequency ultrasonic probe used for tissue fragmentation was estimated between 0.05 to 0.5 MPa [50, 116, 210].

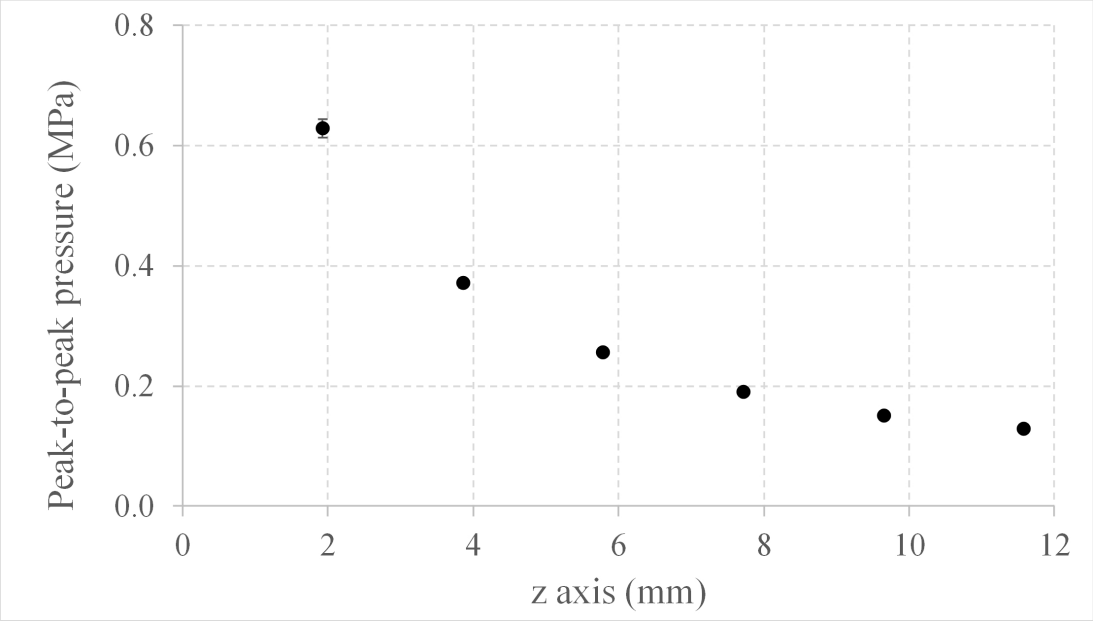

Figure 4.23 Typical peak-to-peak pressure measurement along the z axis ($x = 0$ mm and at $y = 0$ mm) (error bar = standard deviation)

Figure 4.24 shows a typical 2D pressure scan between $z = 4.0$ mm to $z = 11.5$ mm and between $x = \pm 6$ mm. An increment of 1.9 mm was used in both direction. A total of 21 points were used in this 2D scan. The surface plot shows the peak-to-peak values from the pressure waveform measured at each point. The distal tip of the active guidewire is located at (0,0). This 2D scan shows that the pressure distribution is almost symmetrical around the z axis. Also, the maximum pressure level is concentrated near the distal tip in both the z and x direction and decrease rapidly with distance.

4.2.2 Crossing surrogate material

The goal of this test was to demonstrate that the proposed CTO crossing system can drill through material having mechanical properties similar to calcified plaque found in CTOs. As described in section 3.2.2, Begostone plaster material was selected for this experiment. Material with a thickness of ≈ 1.5 mm was typically used for comparison. Performance was evaluated for different active guidewire configurations and different shock wave generator settings. Only a summary of these results is presented here.

Figure 4.25 shows, at different steps, the active guidewire crossing Begostone. For this example, a peripheral active guidewire prototype with a ground core wire, a radiopaque

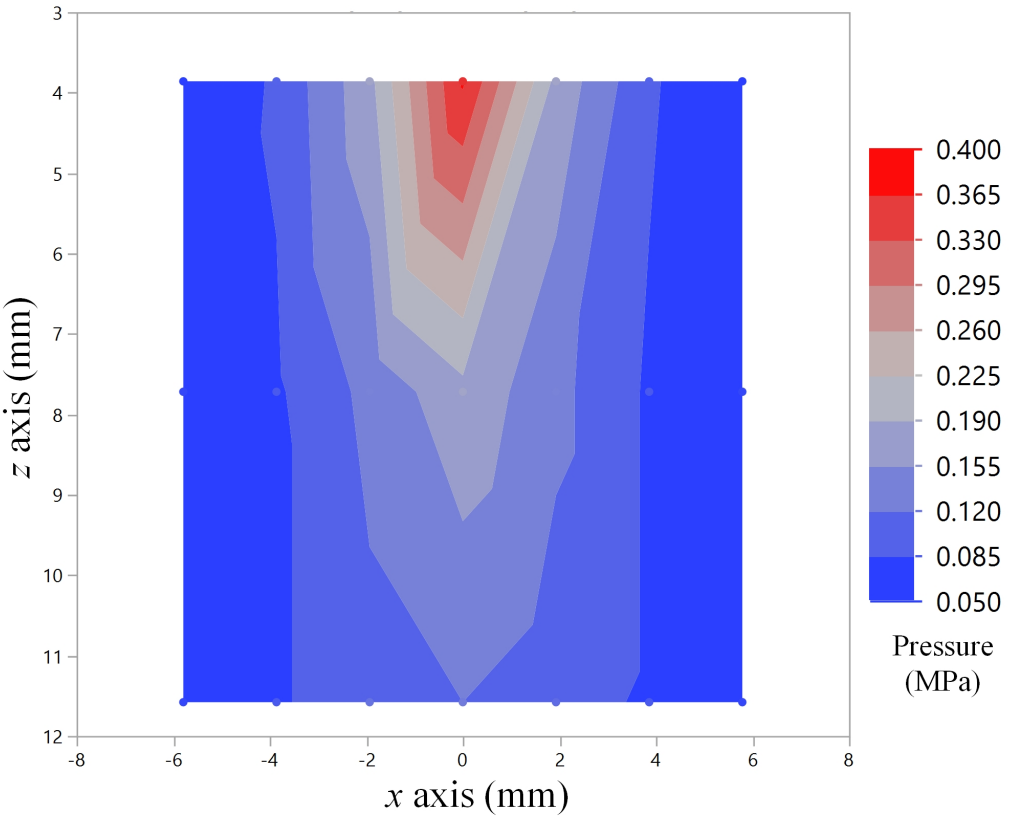

Figure 4.24 Typical 2D pressure scan (xz plan) (peak-to-peak pressure measurement)

marker, PTFE coating and hydrophilic coating was used to cross a Begostone sample. For this specific test, a support catheter was used in a straight path to position the active guidewire in front of the surrogate. The support catheter was flushed with water. The surrogate holder was also immersed in water to simulate clinical conditions. Tap water at room temperature was used.

Panel (a) shows the active guidewire in contact with the surrogate (Begostone) before activation. It was confirmed that without activation, crossing of this material was impossible. Panel (b) shows the active guidewire, with activation, crossing the Begostone. Material removal from the surrogate can be observed during the crossing procedure. The jack-hammering effect at the distal tip creates erosion on the surface of the surrogate while the resulting streaming motion pushes this material away. The specific mechanisms of action associated with this technology are further described in section 5.2. Slight back and forth movement can enhance this effect and facilitate drilling. Notice that the size of the particles removed is very small compared to the size of the wire tip. Panel (c) shows the active guidewire across the surrogate. Panel (d) shows the resulting hole through the

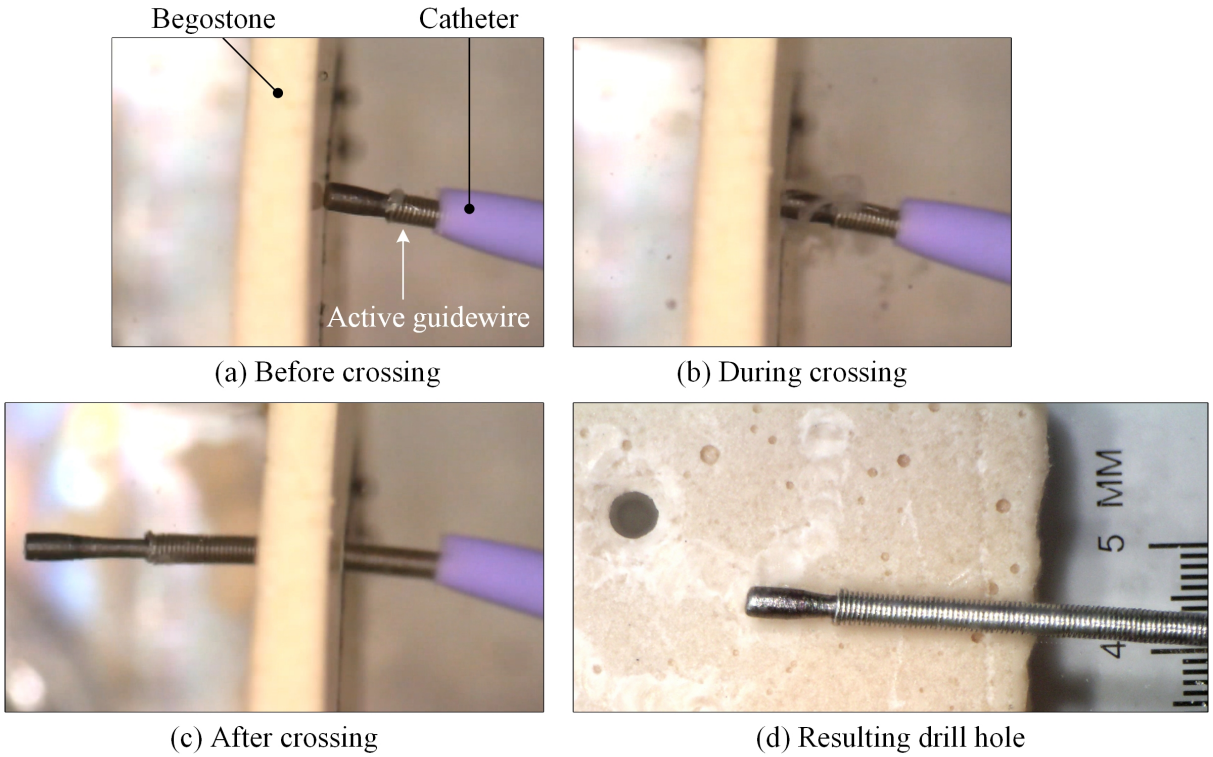

Figure 4.25 Example of a peripheral active guidewire crossing ≈0.5 mm thick Begostone material

Begostone created by the active guidewire. Notice the drilled hole diameter is about the same as the tip of the active guidewire distal tip. To increase the lumen size, more than one pass can be performed while changing the attack point at each pass. In this example, drilling took less than 30 s.

Figure 4.26 shows the average crossing rate obtained with a peripheral active guidewire at different console power levels and repetition rates. For this test, a bench test setup similar to the one presented in figure 3.10 was used in combination with a peripheral vascular model. A straight path configuration was used. A 90 cm long Bard Seeker support catheter was inserted inside the model to access the Begostone material. Begostone samples with an average thickness of 1.5 mm (ranging from 1.15 to 1.70 mm) were used. A ground peripheral active guidewire with a radiopaque marker and PTFE coating was used. The console power was varied between 50% and 100% and the repetition rate was varied between 5 Hz and 10 Hz. The crossing rate results were reported in mm^3/pulse to account for the different Begostone thicknesses. The volume removal rate was calculated as the surface of the tip of the active guidewire multiplied by the Begostone thickness. For each console setting, a total of five (N=5) Begostone samples were crossed. All crossing

experiments were performed by the same operator by applying small forward push on the active guidewire and with slow back and forth tip movement.

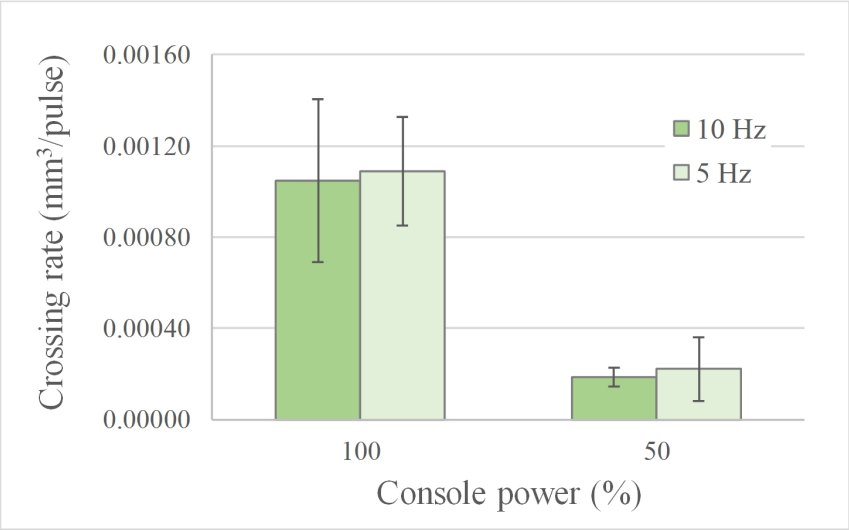

Figure 4.26 Crossing rate achieved with a ground peripheral active guidewire with radiopaque marker and PTFE coating (error bar = standard deviation)

Results from figure 4.26 show that a higher console power increases the crossing rate. However, the crossing rate does not seem to be proportional to the console power level (i.e. doubling the console power has not doubled the crossing time). Additional tests should be performed to evaluate the exact relationship between the console power and the crossing rate. Interestingly, the repetition rate does not impact the crossing rate when reported in mm^3/pulse. However, it is shown that doubling the repetition rate has doubled the crossing speed when reported in mm/s. Errors in the measurement can be attributed to the Begostone material which can vary from batch to batch and to the operator manipulations. However, results are still consistent and within expectations. The same experiment was performed, but not presented here, with a ground coronary active guidewire having a radiopaque marker and PTFE coating. Similar trends were observed at the various console power levels and repetition rates. However, the overall crossing rate performance was about one third of the crossing rate presented in figure 4.26 for the peripheral active guidewire. This may be explained by the smaller core wire diameter of the coronary active guidewire. It is suggested that higher energy loss and less efficient wave transmission from the console to the active guidewire may occur in the coronary active guidewire. Further investigation are needed to explain this observation.

4.2.3 Crossing ex-vivo human CTO specimens

The goal of this study was to demonstrate that shock waves delivered at the distal tip of the active guidewire can facilitate passage across a real human CTO. In this experiment, ex-vivo CTOs dissected from amputated lower limb where used. During the test procedure and under simulated conditions, a first attempt at crossing was tried using a commercial guidewire and the active guidewire without activation. Once it was confirmed that the occlusion was total and that it could not be crossed, the active guidewire was activated and crossing was re-attempted.

Figure 4.27 shows examples of the active guidewire crossing CTO specimens. For this series of tests, many different CTOs (about 15) and active guidewire prototypes (about 5) were used. For example, configurations with Ti-6Al-4V and Beta III core wire material, with and without PTFE coating, and with and without grind were used. None of the active guidewire had hydrophilic coating on it. Also, none of the active guidewire prototypes had a radiopaque marker since this experiment was performed on the bench and not in catheterization laboratory setting. The shock wave generator was used at power levels varying from 50% to 100% and with a repetition rate fixed at 10 Hz.

Panels (a) and (b) from figure 4.27 show a first example of a CTO being crossed by the active guidewire. Total crossing time was about 1 min. Panel (c) shows the same CTO dissected following the crossing procedure. The dissection confirmed the presence of a short blockage near the middle length of the artery segment. This blockage was formed by calcified nodules protruding in the vessel lumen. The rest of the artery was patent (free of occlusion). Panels (d) and (e) show a second example of a CTO being crossed by the active guidewire. This sample had a length of about 1 cm and was fully occluded by densely packed calcified nodules as shown on panel (f). Total crossing time for that CTO was about 1.5 min. At some occasions (not shown here), the active guidewire perforated the arterial wall and exited the vessel structure. Vessel tortuosity, absence of surrounding soft tissues to support the artery segment and absence of fluoroscopy to guide the active guidewire trajectory are believed to have contributed to such result.

Considering the small sample size, CTO heterogenicity and the use of multiple active guidewire configurations, additional testing will be needed to validate these preliminary efficacy results. Nonetheless, this experiment represented the first proof-of-concept of the proposed crossing system. This test showed that the transmission of shock waves via the active guidewire facilitates the crossing of chronic total occlusions. It must be emphasized that these CTOs were obtained from subjects for whom amputation was the only treat-

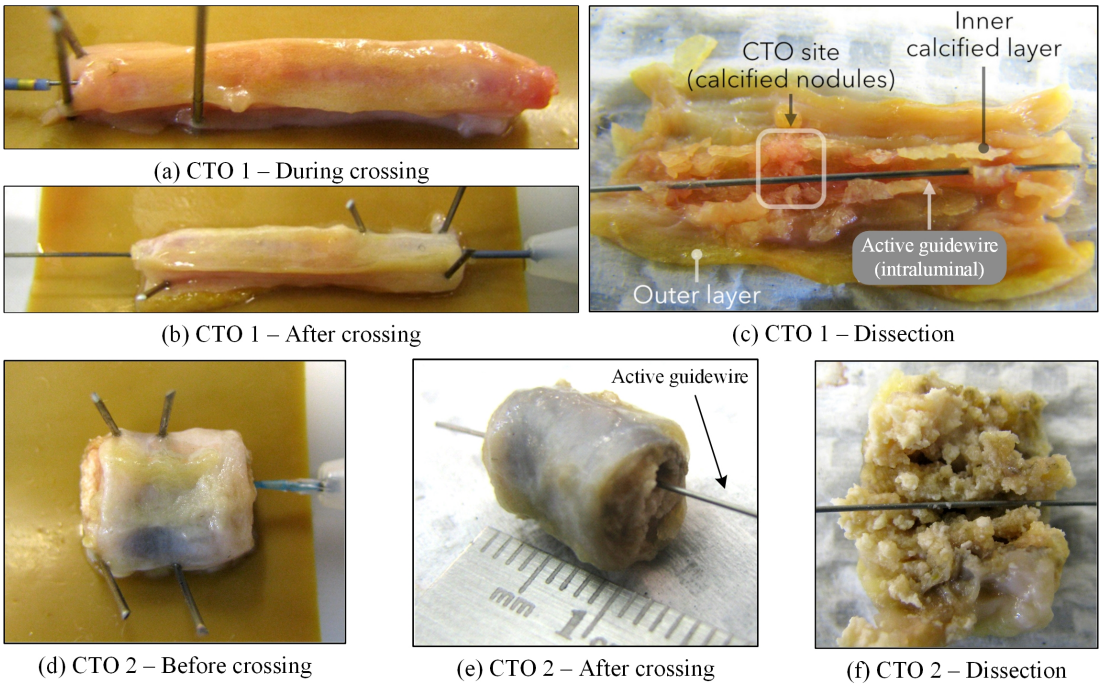

(a) CTO 1 – During crossing

(b) CTO 1 – After crossing

(c) CTO 1 – Dissection

(d) CTO 2 – Before crossing

(e) CTO 2 – After crossing

(f) CTO 2 – Dissection

Figure 4.27 Examples of an active guidewire crossing ex-vivo human CTOs

ment option. This highlights the need for such new technology and confirms its potential.

4.2.4 Endothelial cell viability study results

This experiment consisted of exposing the arterial lumen, and more specifically the endothelial cell, to shock waves energy delivered at the tip of an active guidewire. The goal was to assess the endothelial cell viability and arterial wall damage (dissection) after exposure to shock wave energy. A peripheral active guidewire was used for this experiment with no grind, no coatings and no radiopaque marker. The distal tip was squared and without a chamfer. For this test, most of the length of the active guidewire was in air. To account for the absence of loss resulting from the support catheter filled with water and the absence of coating, the console generator was used at a power level corresponding to anticipated clinical dosing. Therefore, the console power level was 40% and the repetition rate was fixed at 10 Hz.

It should be noted that these results were presented by the author in a poster session at the 2016 Canadian Cardiovascular Congress [154]. Results from this experiment are summarized below.

The percentage of endothelial cell expression (i.e. cell viability) was calculated as the percentage of cells staining positively for PECAM-1 by the lumen circumference of the

cross section. Arterial wall damage was also assessed by histology. Figure 4.28 shows an example of an artery cross-section marked for PECAM-1. This example presents a carotid artery from group III (active guidewire positioned against the vessel wall with shock wave energy delivery). The cross-section shows the vessel wall and lumen. The inner layer of cells, shown in brown, represents the endothelium. When endothelial cells were detached from the vessel wall, as shown in top right corner of figure 4.28, they were considered dead and they were excluded from the viability count.

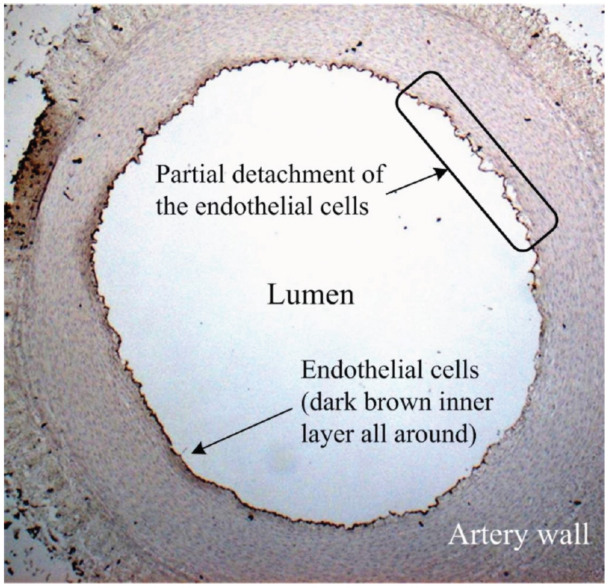

Figure 4.28 Example of a cross-section marked for PECAM-1 of a carotid artery from group III (magnification level 4X)

Figure 4.29 shows the cell viability percentage per test group and artery type. Within experiment error, cell viability was found to be similar, at around 80%, in all three groups and for both artery types. In addition, no arterial wall damage was observed in any samples even though a squared tip active guidewire was used. There was no significant difference between the arteries exposed to the control guidewire versus the ones exposed to the active guidewire. Interestingly, these results are consistent with the ones of Hallow *et al.* [86], where carotid arteries were exposed to ultrasound with the goal to evaluate intracellular drug uptake. It is hypothesized that the small size of the device and the rapid attenuation of the shock wave with distance limited endothelial cells and vessel wall damage.

One limitation from this study concerns its low sample size which limits advanced statistical evaluation of the results. Second, despite best efforts during dissection and manipulation of the artery segments, some samples may have been unintentionally damaged.

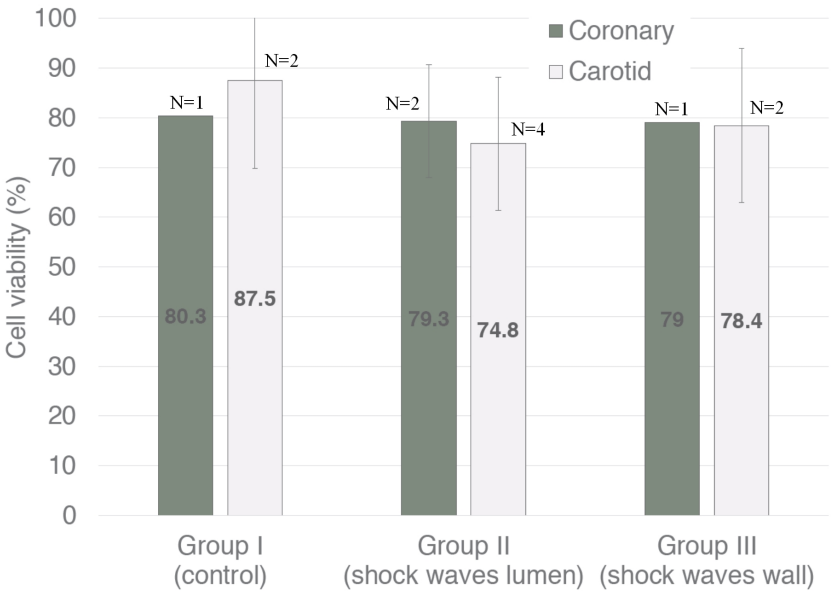

Figure 4.29 Cell viability for the various groups and artery types (error bar = standard deviation)

Nonetheless, exposure to shock waves transmitted at the tip of the active guidewire was found to have a similar safety profile as that of a commercial guidewire. Although further research will be needed to demonstrate safety, this study provided encouraging results.

4.2.5 Acute in-vivo healthy animal study results

The goal of this study was to assess the feasibility to deliver shock waves via the active guidewire in-vivo in coronary arteries. Preliminary data about handling performance of the active guidewire and safety were also documented as part of this an acute healthy animal study. Results of this study were presented in a poster session during the Montreal Intervention Cardiology summit [30].

The shock wave generator described in section 4.1.1 was used for this study along with two different configurations of the coronary active guidewire prototype. Both coronary active guidewires did not have hydrophilic coating and their radiopaque marker was not laser spot welded to itself. Wires were ground and had PTFE coating. The first active guidewire configuration had a square distal tip while the second one had a round distal tip. Also, the active guidewires were carefully shaped using standard tip-shaping practices before insertion in the animal (see figure 4.30). A total of three (3) active guidewires were used (one per animal). Devices were not cleaned and not sterilized for this acute study.

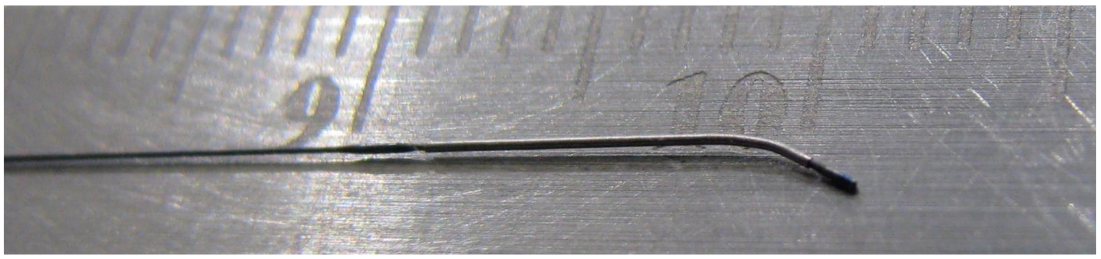

Figure 4.30 Active guidewire used in animal 3 during the acute healthy animal study and having a shaped dsital tip (scale in the background is in cm)

In all cases, the distal marker of the active guidewire was visible under fluoroscopy. All the active guidewires were compatible with the balloon catheter. Normal forces were necessary to push and pull device within the balloon catheter. The active guidewire was able to reach the distal target in tortuous coronary arteries without difficulty. There was no breakage or damage of the device during the procedure confirming its mechanical integrity and durability when used under simulated clinical conditions.

No cardiac events were observed during activation of the device. Heart rate and blood pressure also stayed normal. Out of the twelve treated arteries treated with the active guidewire, only one vessel perforation was observed angiographically in the LAD artery of animal #2. The perforation happened using a squared tip active guidewire configuration and with no shock wave energy delivery. The perforation resolved spontaneously without any treatment and the procedure was continued with no further observations. As for every CTO-PCI, perforation is a common anticipated complication [140]. It is believed that this event was related to the lack of familiarity of the operator with this device. As with every new technology, a learning curve is necessary. However, only limited training was provided before this study.

Figure 4.31 shows typical coronary angiograms at baseline, following injection of the different Ach concentrations and following nitroglycerin injection. These angiograms were taken on animal #1 after treatment with the console power level at 100% and with a squared tip active guidewire. Treatment site was in the LAD just after the first diagonal branch (D1) and was referred as mid position. On figure 4.31, vasoconstriction of the LAD is noticeable as the concentration of Ach progressively increases. At a concentration of 10^{-5} mol/l, the vessel was completely constricted as apparent by the absence of contrast flow. Injection of Ach at a concentration of 10^{-4} mol/l was skipped and nitroglycerin was injected per protocol. As observed on the bottom right frame, the nitro vaso-dilated the vessel near to its original diameter.

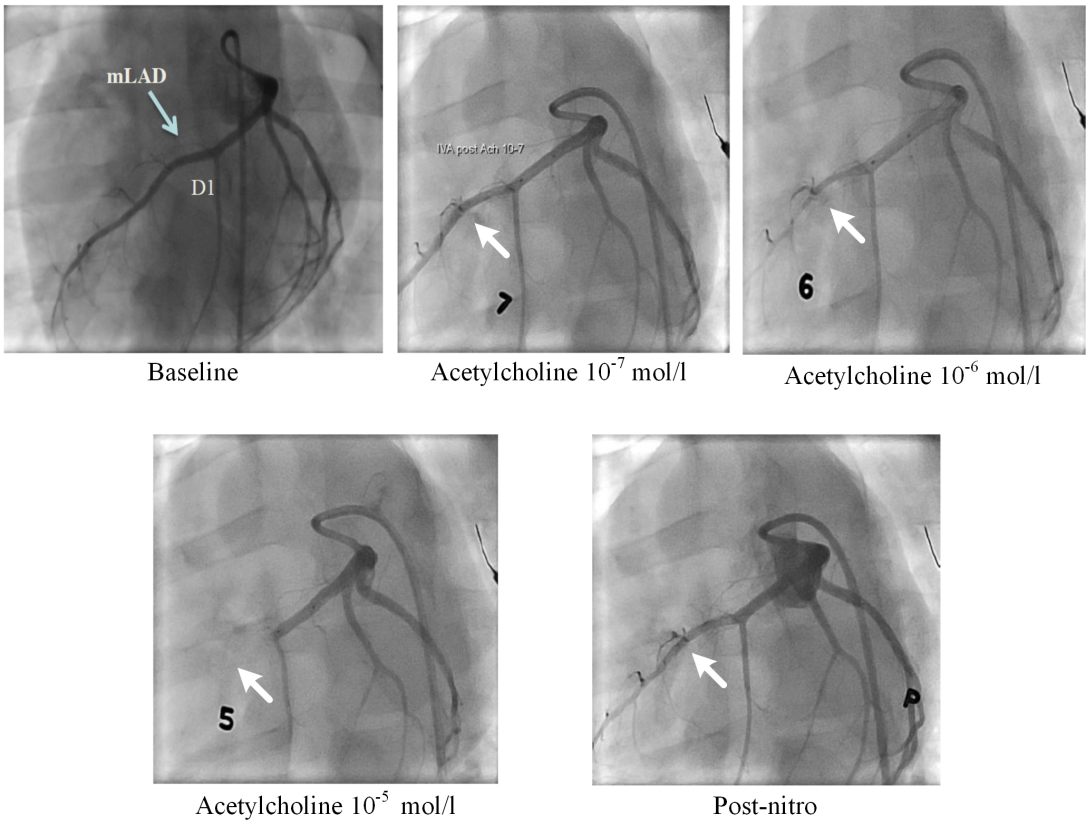

Figure 4.31 Representative coronary angiogram of the LAD showing the vessel vasoconstrictive response to intracoronary infusion of acetylcholine (arrow shows the treatment site)

Figure 4.32 shows the average lumen diameter results from the Ach injection procedure. The top graph shows the results summarized in a histogram. The error bars correspond to the standard deviation. The bottom graph illustrates the same results, but displayed with curves to facilitate understanding. Results are presented at the different console power levels (0%, 50%, 75% and 100%). Note that the sample size was not the same for all amplitude levels: 0% (N=5), 50% (N=1), 75% (N=4) and 100% (N=2). Considering this low sample size, no distinction was observed between the different active guidewire tip configurations and when the device was moved or not. As anticipated, vessel diameter decreases as the Ach concentration increases and returned to normal after nitro injection. However, no clear correlation between the console power level and the vessel diameter measured by QCA at the different Ach concentrations was found. For example, at a concentration of 10^{-6} mol/l, the smaller vessel diameter is observed at a console power level of 0%, followed by 75%, 100% and the larger vessel diameter is observed at a console power level of 50%. At a concentration of 10^{-5} mol/l, the sequence changes for 100%, 0%, 75% and 50% (smaller to larger vessel diameter). At a concentration of 10^{-4} mol/l,

the sequence changes again for 100%, 75%, 0% and 50% (smaller to larger vessel diameter). It is hypothesized that the low sample size and the multiple study variables (tip configuration, tip movement, console power level, etc.) may have influenced the results. In addition, the method of Ach injection to evaluate in-vivo endothelial cell damage was previously used in chronic studies, during a second catheterization procedure after the initial angioplasty procedure (i.e. four weeks to six months after), and not live (acute) as it was performed here [46, 201]. This could be of significant importance considering that regrowth of endothelial cells was observed in pigs as soon as four days following a PTCA intervention [181]. Therefore, it is unknown how relevant the results of the current Ach procedure are.

During injection of Ach in animal #3, the target vessel presented a severe, prolonged and diffuse spasm. Nitroglycerine was injected as a treatment, but it was not possible to restore the blood flow. Severe ischemia with ventricular arythmia appeared in consequence of the serious coronary artery spasm. Several unsuccessful attempts were made to resuscitate the animal. It is believed that this event is not directly related to the active guidewire, but is rather attributed to the injection of acetylcholine.

Figure 4.33 summarizes the endothelial cell viability results versus the console power level and the tip geometry. Error bars correspond to the standard deviation. Sample sizes are labeled on the graph and are different from the Ach study since the results from two artery segments were missing. From these results, there is no clear correlation between the console power level and the endothelial cell viability. Within the experimental error, no difference was observed between square and round tip geometry. Console power levels of 0% and 50% resulted in the least cell viability percentage while 75% and 100% console power levels resulted in the higher cells viability percentage. Considering the large variability in cell viability, results from section 4.2.4 are comparable to the ones of this study. Also, these results are in accordance with the literature, where it was shown that endothelial denudation appears during angioplasty and especially during balloon angioplasty [98, 181]. Comparing results from figure 4.33 with the ones from the Ach study, no direct relationship can be observed between these set of data, adding to the ambiguity.

Figure 4.34 shows examples of artery cross-section treated, or not, with the active guidewire. Top left panel shows a cross-section of the RCA from animal 1. This artery was used as a control. This artery was not exposed to the device or to Ach, and no histologic finding was observed. The top right panel shows a cross-section of the mid LAD from animal #1 which was treated at 100% console power level and with a squared tip active guidewire. Thrombus formation, partially attached to the vessel wall, can be observed in the vessel

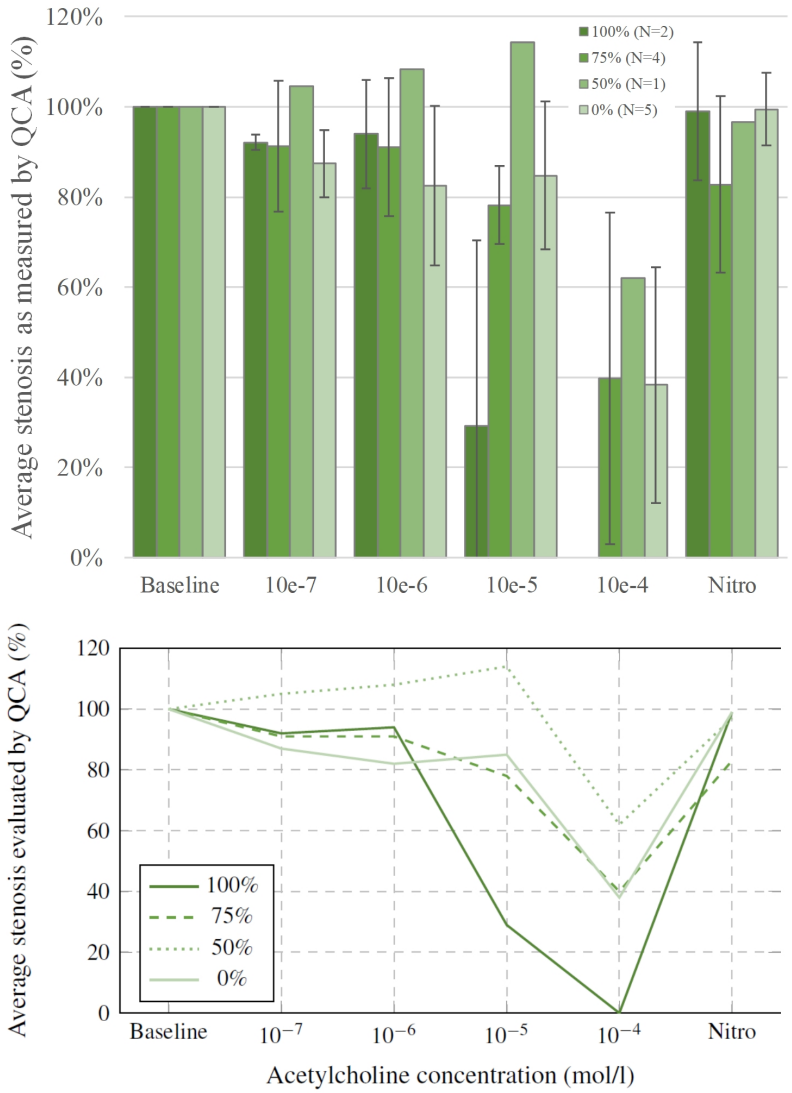

Figure 4.32 Average lumen diameter as measured by QCA versus console power amplitude levels and Ach concentrations (top = bar graph where the error bars correspond to the standard deviation and bottom = same as top, but with curves instead of bars)

lumen at around twelve o'clock. However, it cannot be concluded if this thrombus is related or not to the use of the device. For example, this thrombus may have resulted from the procedure itself or may have appeared during preparation of the heart for dissection of the treated vessels. The mid left panel shows a cross-section of the proximal RCA from animal #2 which was treated at 50% console power level with a squared tip active guidewire. A thrombus formation, not attached to the vessel wall, can be observed floating in the vessel lumen at around eleven o'clock. The mid right panel shows a cross-section of the distal RCA from animal #2 which was treated at 0% console power level with a squared tip active guidewire. Two thrombus formations, partially attached to the vessel wall, can

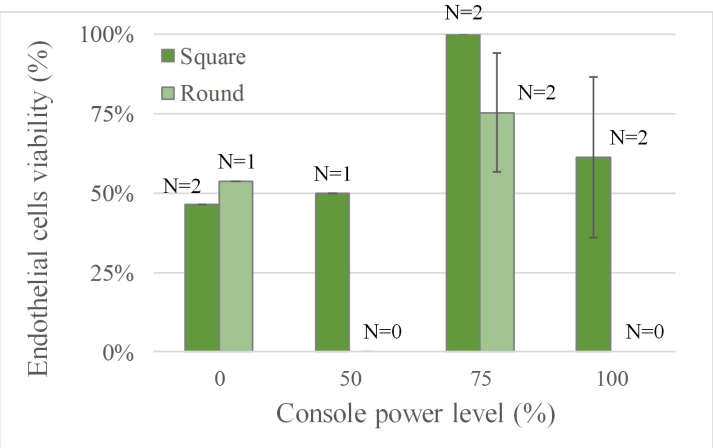

Figure 4.33 Average endothelial cells viability versus shock wave amplitude level and tip geometry (error bar = standard deviation)

be observed in the vessel lumen at around six and twelve o'clock. A small hemorrhage can also be observed in the media between seven and nine o'clock. The bottom panel from figure 4.34 shows a cross-section of the distal LCx from animal #3 which was treated at 0% console power level with a rounded tip active guidewire. No specific histological findings were recorded for this cross-section. It is noticed that thrombus formation was also observed in one case without insertion of the active guidewire and in other cases without shock wave emission. All these histology observations could be related to the test device, procedure and/or the operator. Considering the study design, it is not possible to clearly relate the findings with the cause.

The small sample size (N=3 animals) limited the statistical power of this study. The number of variables and the absence of an appropriate control also restrained the study outcomes. In addition, it is believed that the limited operator training may have influenced some of the study results. Future animal studies should take these limitations into account during the design of the protocol.

In conclusion, this study was still successful at demonstrating the feasibility to deliver shock waves via the active guidewire in-vivo in coronary arteries. Technical handling performance of the device were satisfactory from the operator standpoint. Preliminary acute safety data were gathered. No cardiac events during activation of the device were observed. Out of the twelve treated arteries with the active guidewire, only one vessel perforation was observed angiographically. The perforation resolved spontaneously without any treatment and the procedure was continued without any further observation. Acute in-vivo vessel injury was evaluated using acetylcholine injection followed by QCA measurement. No clear correlation was established between the console power level and the

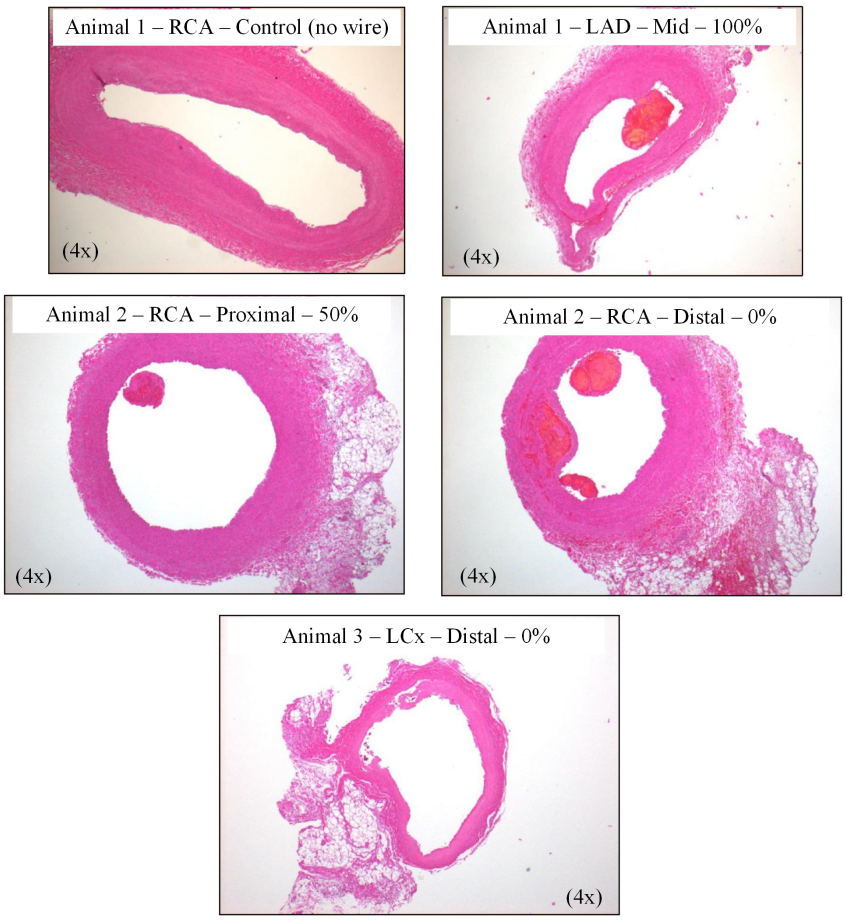

Figure 4.34 Example of artery cross-sections stained with H&E

vessel diameter after Ach injection. Vessel injury and endothelial denudation were also evaluated using histology. No clear correlation was established between console power levels and endothelial cell viability. Some vessel injury (thrombus formation and medial hemorrhage) were observed, but it was not possible to identify the precise cause. However, it is believed that the vessel injuries reported here are typical of what observed clinically in CTO PCI procedures [199]. Overall, the preliminary safety profile of the device is judged sufficient to continue its development of the proposed CTO crossing system.

CHAPTER 5

DISCUSSION

This chapter presents some of the limitations associated with the experimental methods and the design of the proposed device. The mechanism of action associated with the proposed CTO crossing system are presented and explained. Lastly, the advantages and disadvantages of the proposed technology are described and compared with other similar devices.

5.1 Method and technology limitations

The preliminary safety and efficacy data presented in section 4.2 are promising. These suggest to continue the development of this technology. However, some limitations associated with the test methods and the proposed system were also observed. These are summarized below and discussed later in this section:

- variability in the pressure measurement;
- missing evaluation of particle size and distribution released during simulated testing;
- active guidewire durability;
- active guidewire energy loss;
- active guidewire's distal tip geometry effect on performance;
- output waveform effect on performance.

When characterizing the performance of the CTO crossing system via the pressure measurement method, variability in the peak-to-peak pressure was noted. The standard deviation resulting from the peak-to-peak pressure measurement was sometime as large as $\pm$ 20% of the average value. This variability could be observed with the same device after different installations and connections. In addition, both the fiber optic hydrophone and the needle hydrophone have an uncertainty of 15-20% on their sensitivity value (according to their calibration data sheet). During ramp up tests (i.e. when peak-to-peak pressure was measured at different console power increments), saturation in pressure level was observed above a certain power output threshold. These observations may have multiple potential causes. For example, variability and saturation may be caused by the shock wave generator, the connection process, the active guidewire material, its boundary conditions, the fluid coupling between the active guidewire and the sensor and/or the sensor itself.

Further investigations are needed to determine the specific cause(s). However, it is believed that the pressure measurement results presented in subsection 4.2.1 still give a good understanding of the overall performance of the system. Other means were evaluated for measuring the system performance without success. For example, microphone and laser interferometer were considered, but they were lacking in sensitivity and acquisition rate.

One important safety aspect that was not addressed in the current research work is related the size and quantity of particles released by the device or from the CTO during a simulated procedure. This is an important safety concern as particles released in the blood circulation may lead to emboli, a blockage of a downstream vessel, and result in further complications [70]. There exists no specific acceptance criteria related to the safe limit of particle size and quantity that can be released in the circulation [9]. As an order of magnitude, a red blood cell has a diameter of about 6-8 μm and can pass freely through the smallest vessels (capillary). In comparison, typical embolic filter devices used to capture particle released during angioplasty have pore size of 80-100 μm [119]. In a more recent study comparing different types of hydrophilic coating on angioplasty balloon catheters, Babcock *et al.* [14] showed, in a 28-days chronic animal study, that injection of a fluid with about 25000 coating particulates $\geq$ 10 μm in the coronary arteries did not result in immediate angiographic evidence of occlusion. Moreover, only in rare occasions, particles appear in the tissue downstream during histology analysis. Future studies on the proposed CTO crossing system will need to address particle size and quantity released during simulated use. However, considering the construction of the active guidewire and its similarity with other devices, it is believed that particulate results will be within the same safe range as current CTO crossing devices.

One limitation of the current system is associated with the endurance of the active guidewire. During the experimental phase, a limited amount of failures at the proximal reducer weld and in the core wire were observed. These happened at various activation times and at various shock wave generator levels. No clear trend was noticed except that higher power level seems to shorten the time to failure. Figure 5.1 shows an example of such core wire failure observed under scanning electron microscope (SEM). This sample was obtained from a 300 cm long ground peripheral active guidewire with PTFE coating and a radiopaque marker. The failure location happened near the distal end, in the ground portion, where its diameter is 0.20 mm. This failure happened during a crossing test after more than 5 min of continuous activation and at maximum (100%) output power level. By examining the fracture surface on figure 5.1, it is observed that the main mode of failure is associated to fatigue (cyclic load). The initiation site is observed at the surface

of the active guidewire. Following initiation, the crack propagates after each pulse. This is characterized by the beach mark pattern observed on the top right image of figure 5.1. Once the crack was large enough, the remaining surface area of the material could not sustain the applied stress anymore and breaks. This zone corresponds to the final rupture and is typically associated with a surface fracture appearance that is different from the propagating zone. It is hypothesized that a rough surface finish and abrupt cross-section variation may facilitate crack initiation and should be avoided in the next iteration of the active guidewire to extend device lifetime. Alternatively, different surface treatments may be used to introduce residual compressive stresses at the surface, which can limit crack initiation and propagation (e.g. via shot peening, glow discharge plasma treatment or heat treatment) [109, 115, 129].

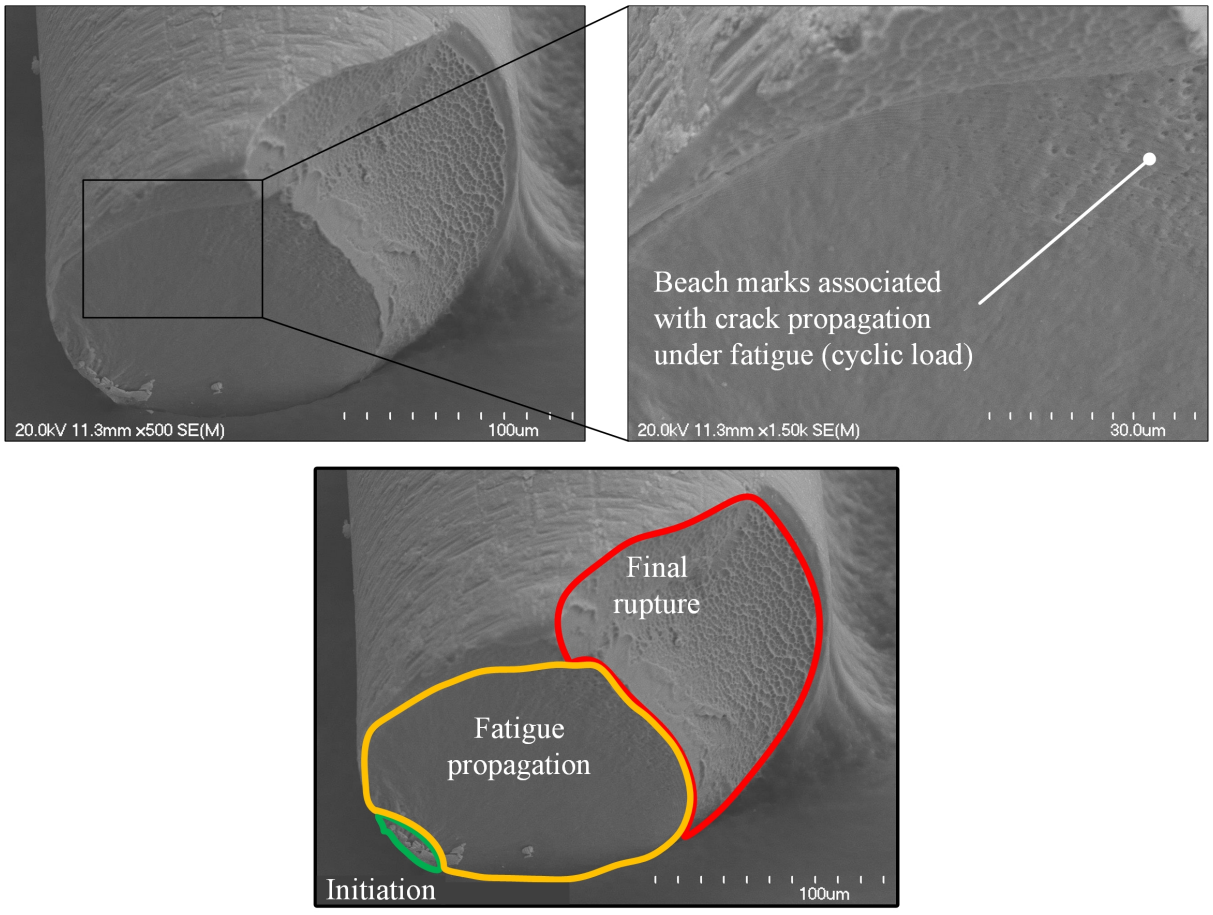

Figure 5.1 Scanning electron microscope images showing the surface fracture of the active guidewire core wire

Another limitation of the current system is associated with the losses observed from the active guidewire when used in different simulated conditions. It was noticed that performance of the CTO crossing system is a function of the boundary conditions and the

surrounding medium in which the active guidewire is used. For example, it was found that crossing performance was reduced when the active guidewire was squeezed between fingers versus free and when the active guidewire was in water versus in air. The presence and the type of coatings also impacted performance of the system. This is in accordance with the discussion presented in subsection 2.3.6 about wave attenuation caused by extrinsic factors. Attenuation level as high as 60 % was noticed depending on the boundary conditions. To avoid reduction in system performance, the input power level from the console may be increased to compensate for the losses, a shorter support catheter may be used and a special handling tool may be designed to manipulate the active guidewire during use (push, pull and rotate). In addition, according to figure 2.17, a reduction in wire size and/or operation at a lower centered frequency may reduce the attenuation level associated with the surrounding medium. Use of a core wire material with a higher acoustic impedance may also reduce loss into the surrounding fluid (saline or blood).

In the context of this research, one distal tip shape was mostly used (shown in figure 4.15). Even though preliminary performances were encouraging, it is unknown if this is the optimal tip configuration. For example, round tip, bevel tip or conical may be of interest. When assessing the performance of a new tip design, safety and efficacy should be considered. For example, a sharper tip may skive the inside the of the catheter and create emboli particles. It may also easily perforate the arterial wall. On the other side, a sharper tip may more easily penetrate the CTO and facilitate re-entry when in the sub-intimal space. Some tip shapes may favor radial tip motion, which can be useful to enlarge the hole created by the active guidewire. Also, as shown on figure 4.15, the grind profile of the active guidewire is such that the very distal tip is larger than the section proximal to it (underneath the radiopaque marker). It is unknown if this rapid increase in cross-section could affect the performance of the active guidewire. It is hypothesized that since the wavelength is much larger than the core wire diameter, only the first longitudinal mode is traveling and that it should not be impacted by small variation in cross-section. However, this was not verified experimentally.

Only one type of waveform was used during verification testing. [redacted]
. This output waveform is believed to maximize the peak-to-peak pressure output measured at the distal tip of the active guidewire. One unique advantage of the proposed technology concerns the fact that it can be calibrated to output many different waveforms. For example, output waveform with a reverse polarity, longer/shorter pulse duration or with more/less oscillations could be used. [redacted]
It is most likely that these other waveforms will have a lower peak-to-peak value, but they

could still demonstrate good crossing ability. It is unknown if different waveforms may be more appropriate on certain tissue types (for example, calcified versus fibrotic). Also, it is unknown if other waveforms may be less demanding for the electronic and/or less attenuated when traveling in the core wire. Future investigations are needed to assess the effect of the output waveform on the system performance and safety. It is important to note that, as opposed to other technologies like the Crosser, the output waveform parameters of the proposed CTO crossing system can be modulated over a certain range, which provides a unique advantage.

5.2 Mechanism of action

The mechanism of action associated with the proposed CTO crossing system were investigated and are described in this section. During investigation, high-speed videos of the tip of the active wire were captured. A Fastcam SA-X2 RV from Photron (Tokyo, Japan) was used in combination with a Navitar zoom lens 12X model 50486 (Rochester, United States), a Navitar tube adapter lens model 1-6030 (2X) and a Navitar lens attachment model 1-51473 (2X). The high-speed camera was interfaced with a computer and the Photron fastcam viewer software was used for acquisition and post-processing. Appropriate lighting was obtained using a large LED spotlight and mirrors. An example of the high-speed camera test setup is shown in figure 5.2. A 3D positioner was used with a pin vise to hold and position the distal end of the active guidewire in a small custom-made water tank. The right image on figure 5.2 is a view from the camera showing the distal tip of the active guidewire in water. Acquisition parameters were varied from test to test, which affected the camera shutter speed, field of view and the resolution. A maximum frame rate of 100000 images/s was used during testing. Above this level, the region of interest become so small that the distal tip could not be seen entirely. A variety of experiments were designed, performed and filmed with the high-speed camera. For example, one experiment was performed while filming the tip of the distal active guidewire immersed in water. In other experiments, the active guidewire was crossing various surrogate materials in water or in air. In another experiment, particles were suspended in water to capture the associated fluid motion in front of the active guidewire during activation.

From the high-speed video experiment in which particles were suspended in water, fluid motion was observed in front of the distal tip of the active guidewire. This fluid motion was associated to a streaming effect and resulted from the transmission and propagation of the mechanical pulse in the fluid medium. This result is consistent with the work of McGuinness *et al.* [120], where a similar streaming effect was observed near the tip of an

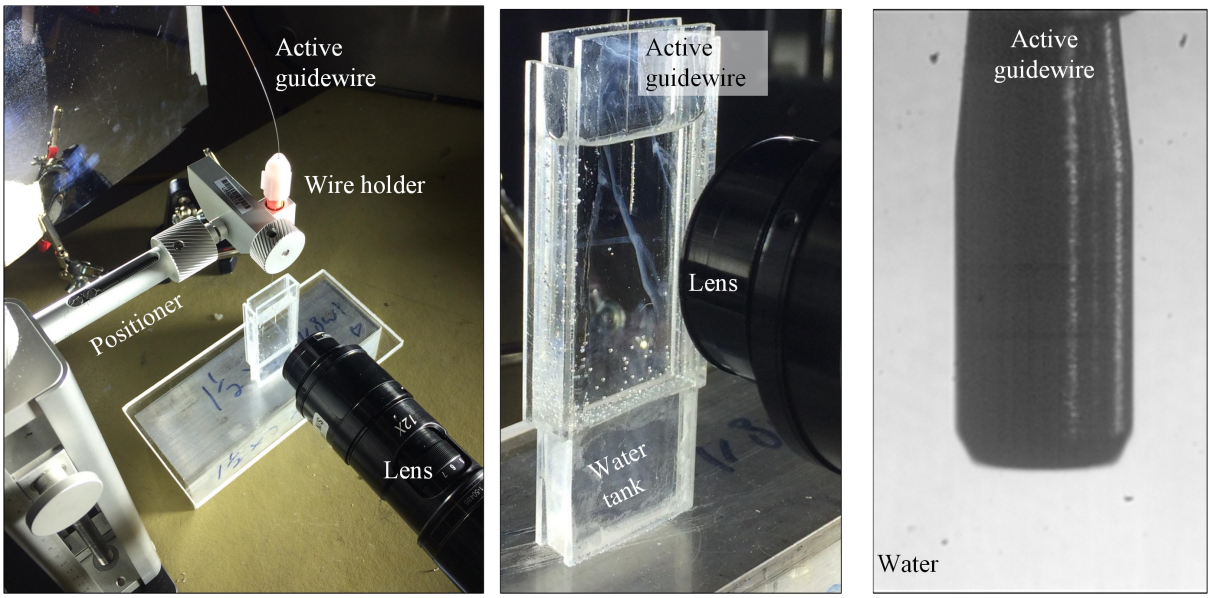

Figure 5.2 Example of the high-speed camera bench test setup

high-power low-frequency ultrasonic probe designed to cross CTOs. Streaming resulting from the active guidewire was not quantified. Qualitative assessment showed that streaming was limited in the region in front of the active guidewire and last much longer than the pulse duration. This phenomenon was also noticed during Begostone crossing (refer to subsection 4.2.2). It is believed that streaming accompanied with slow back and forth movement of the active guidewire can facilitate crossing by helping to clean the debris accumulated in front of the device. Particle image velocimetry (PIV) could be used to quantify the streaming motion and should be tried as part of the future work.

In addition, during high-speed video testing, attention was paid to assess the presence of cavitation bubbles. Cavitation is one of the key mechanisms used by other ultrasound therapeutic medical devices to facilitate CTO crossing or break down kidney stones [90, 120, 213]. From the analysis of the various high-speed videos and in specific conditions, cavitation bubbles and clouds were observed forming and collapsing near the distal tip when the principal pulse was emitted in water. Figure 5.3 shows one example of a cavitation cloud forming at the surface of the active guidewire during a single pulse emission at different time intervals. These frames were obtained following the analysis of a high-speed video recorded at a frame rate of 100000 images/s. A 300 cm long and ground peripheral active guidewire with a radiopaque marker and PTFE coating was used with the console at 100%. For this experiment, most of the active guidewire length was in air, with limited extrinsic attenuation. Distal tip diameter of the active guidewire was 0.29 mm. On figure 5.3, at t = 0 μs, the active guidewire is at rest. At t = 10 μs, the principal pulse is

emitted. A cavitation cloud of about the size of the active guidewire diameter is observed between t = 20 μs and t = 40 μs. Then, the cavitation cloud collapses at t = 50 μs. Many other weaker cavitation clouds are observed forming and collapsing between t = 60 μs to t = 150 μs. After t = 150 μs, no more cavitation is observed until the next pulse is emitted about 100000 μs later. Referring to figure 4.22, the cavitation clouds are lasting longer than the principal pulse duration (150 μs versus about 30 μs). Interestingly, it was also observed that cavitation was only visible above a certain console power threshold. For example, during the same experiment, the console power was gradually decreased by 20% increments. Cavitation was still visible at 80% console power, but not at 60% and below. This is consistent with what described by Leighton [107], where cavitation is presented as a threshold phenomenon. This threshold is characterized by the peak negative pressure p^-, the pulse frequency and the size of pre-existing bubble available to nucleate.

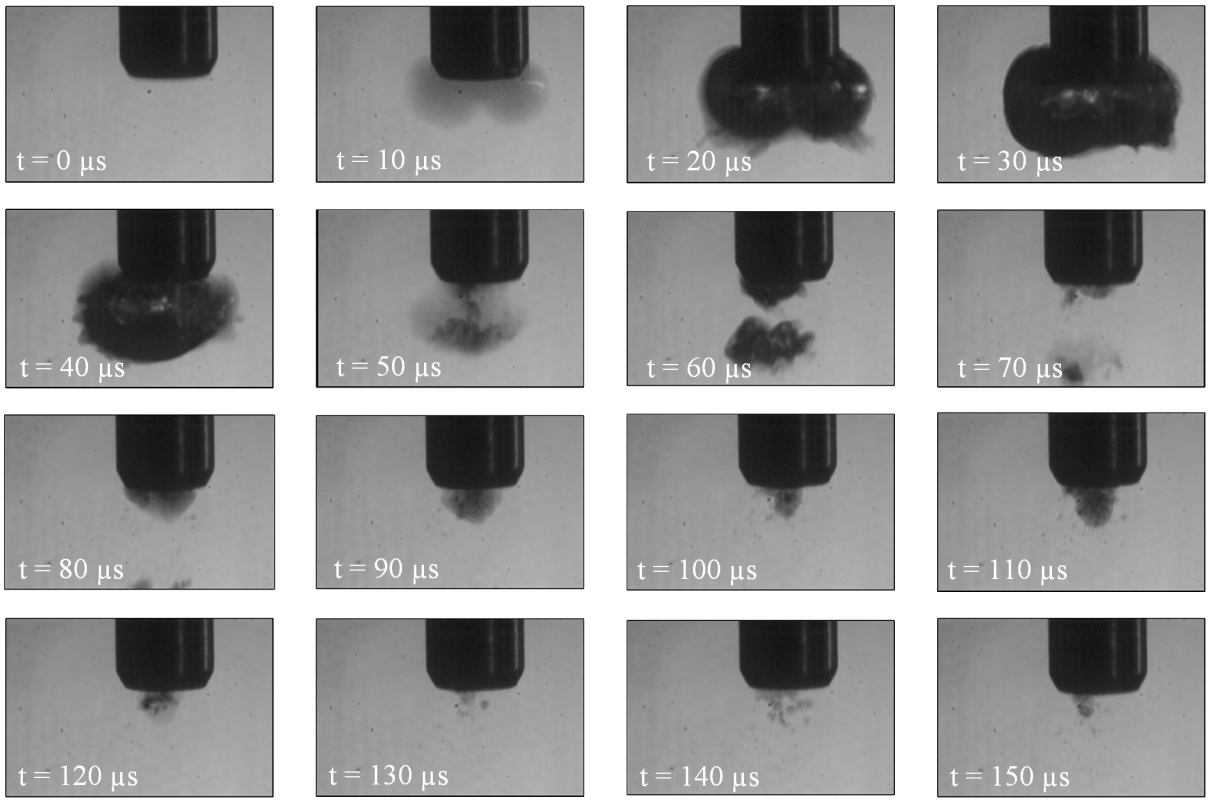

Figure 5.3 Example of a cavitation cloud at the surface of the active guidewire as observed during a high-speed video experiment (frame rate = 100000 images/s)

In comparison, cavitation bubbles caused by the Crosser tip motion can last for about 22000 μs [213]. Cavitation bubbles caused by extracorporeal shock wave lithotripter can last for about 300 μs [143, 176]. The difference in cavitation bubbles lifetime may be explained by the different pulse amplitudes, pulse durations, pulse shapes and repetition

rates of each device. Further investigations are still needed to evaluate if cavitation is present under real use conditions (i.e. when the active guidewire is used inside a catheter and in blood). It will also be important to evaluate the role that cavitation plays regarding the safety and efficacy of the device. The presence of cavitation may also explain the variability observed during pressure measurement test.

After analysis of all high-speed videos, it was possible to observe motion of the distal tip in specific conditions. However, considering that a maximum of 100000 frames/s (each frame corresponding to an increment of 10 μs) was achievable and knowing that the peak pulse half cycle last only 0.25 μs, detection of the real maximum tip displacement was challenging. In addition, at higher console power levels, the peak tip motion is usually hidden by the cavitation cloud (refer to figure 5.3). Nevertheless, a technique similar to the one proposed by Gavin *et al.* [78] was used to evaluate the tip motion. This technique consists to measure the blurred zone thickness in front of the distal tip in the exact frame corresponding to the principal pulse emission. An example of this is shown at figure 5.4 with the same active guidewire and test configuration described in cavitation experiment, but at a console power of 80% (to minimize the cavitation cloud blindness). In this example, a small blurred zone thickness is observed in front of the active guidewire in the frame right before the first cavitation bubble appeared. Knowing the diameter of the active guidewire and measuring the thickness of the blurred zone, the tip motion is estimated to be about 44 μm. In the following frames (t $>$ 20 μs), the blurred zone disappears, but residual slower oscillations (not blurred) of the tip are visible. Much later after the principal pulse (t $>$ 5000 μs), the distal tip motion completely stops until arrival of the next pulse. In comparison, high-power low-frequency ultrasound devices, like the Crosser catheter and the Sonopet UST-2001, has shown tip motion ranging from 20 to 320 μm when measured in similar test conditions [132, 210]. To confirm the active guidewire tip displacement results presented in figure 5.4, the experiment should be repeated many time while synchronizing the pulse emission with the trigger of the camera for a more accurate measurement.

Even though the tip motion is small, the force transmitted is high. For example, one indirect way of estimating the force traveling in the active guidewire is by looking at the fracture surface of a core wire. By estimating the surface area of the final rupture zone and knowing the ultimate strength of the material, the force at failure can be estimated. In the example presented in figure 5.1, the final rupture surface area is estimated to be ≈ 0.012 mm^2 (about 40% of the cross-section). The ultimate tensile strength is estimated to be close to the yield tensile strength for this material (around 1600 MPa) (refer to

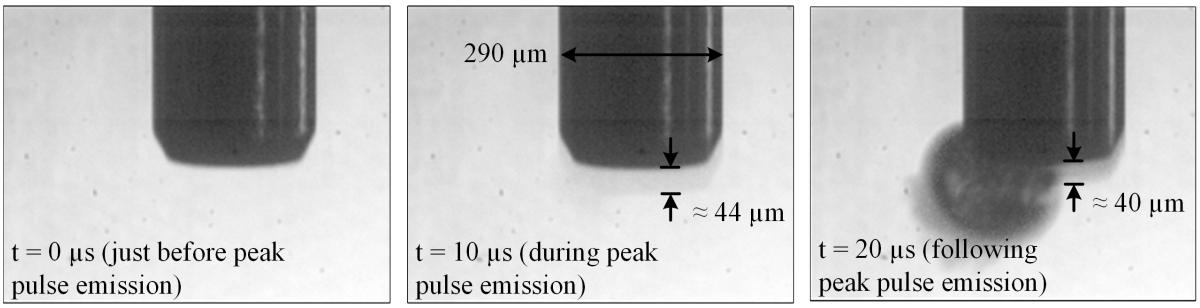

Figure 5.4 Example of tip motion measurement

table 4.2). Therefore, a propagating force of about 20 N can be estimated within the core wire. It should be noted that the associated load case is very complex (high strain rate, transient and multiple oscillations). Therefore, it is most likely that the quasi-static assumption is not valid. However, this calculation still provides an idea about the order of magnitude of the force associated with the traveling mechanical wave inside the core wire.

It was shown that the force deployed at the distal tip of the active guidewire is sufficient to drill through hard material. This was experimentally demonstrated, as highlighted in subsections 4.2.2 and 4.2.3, where the active guidewire showed crossing ability in hard Begostone plaster-based material and calcified ex-vivo CTOs. This was further confirmed in another experiment, not presented here, where the active guidewire could drill through a microscope cover glass of about 0.15 mm thick with only few pulses (< 10). As shown on figure 5.5, the active guidewire was able to drill through the cover glass without shattering it apart.

In summary, it is believed that the principal mechanism of action of the proposed CTO crossing system can be associated to a micro-jackhammer having very small displacement, but of large force. This micro-jackhammer effect is accompanied with fluid streaming motion. The fluid streaming is believed to facilitate crossing by removing the small dust particles resulting from the micro-jackhammer effect in front of the active guidewire. The proposed device mechanism of action is also characterized by the absence of heat accumulation. Another unique feature of the proposed technology is its ability to differentiate tissues according to their compliance (or elasticity). For example, when put in contact against soft tissues and activated, for example skin or healthy arterial wall, no damage was observed. This was verified through preliminary safety experiments (endothelial cell viability test and in-vivo animal study). However, when in contact with hard material (like vascular calcification or plaster-based material), surface erosion and drilling were observed. Cavitation may also play an important role, but further investigations are needed

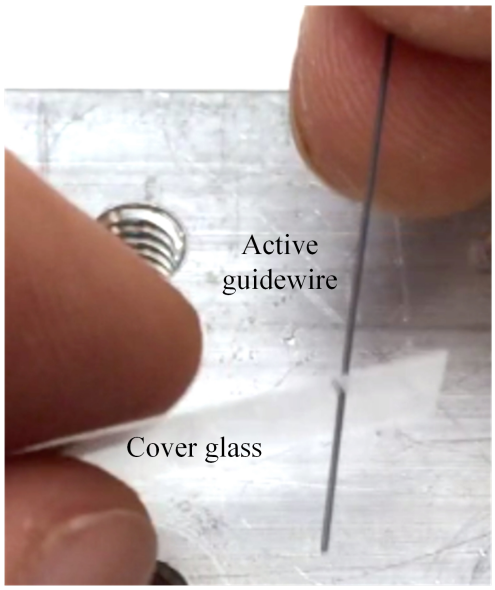

Figure 5.5 Active guidewire crossing a microscope cover glass

to evaluate its presence under real use conditions. Micro-jackhammer, streaming and tissue differentiation are consistent with the mechanisms of action of high-power low-frequencies ultrasonic probe used for tissue dissection and ablation [50, 132]. The key advantages of the proposed technology versus the ultrasonic probe are characterized by an absence of heat accumulation, its compatibility with conventional angioplasty equipment and the fact that it can be controlled (amplitude, repetition rate and waveform).

5.3 Comparison with similar technologies

At this point, it is premature to compare the proposed CTO crossing system with commercially approved CTO crossing devices. The goal of this research was to design and demonstrate the ability of a novel device to facilitate CTO crossing. Therefore, the experiments described in this thesis were designed only to demonstrate early safety and efficacy proof-of-concept. In addition, testing was performed with prototypes devices and further development will be needed to refine the design. However, it could still useful to list the anticipated advantages and disadvantages of the current prototype device relative to other technologies having the same intended use to identify opportunities for amelioration.

The downsides of the proposed technology can be associated with the size and cost of the shock wave generator, the active guidewire endurance and the inability to exchange support catheter over the active guide. Catheterization laboratories have limited space and many efforts are deployed to reduce hospital medical expenses. Therefore, the shock

wave generator will need to have a smaller footprint and be more affordable. Competitive devices like the Spectranetics laser, the Dabra laser and the Ocelot catheter using OCT can be used for bench marking of the shock wave generator size and cost. It is believed that with more development, appropriate footprint and cost of goods could be achieved. As noted in section 5.1, the core wire and proximal reducer weld may fail under fatigue (cyclic load). This is certainly something that will need to be addressed in the next iterations. However, one strategy proposed to mitigate this, in the short term, is to restrict the lifetime of the active guidewire. Even though this is not the ideal situation, other devices have adopted such strategy. For example, the Crosser catheter has a 5 minutes lifetime that is controlled by its console generator. Additional, due to the active guidewire's large proximal end, a catheter cannot be exchanged over the active guidewire. This forces the physician to start the procedure with the ideal support catheter, without the ability to easily switch catheters. Alternatively, the physician can exchange the active guidewire for a conventional guidewire before the support catheter can be exchanged, but this add extra steps and time to the procedure. Future iteration of the active guidewire should be able to be connected to the console directly at the wire level instead of using the section reducer.

One of the main advantages of the proposed CTO crossing system is the fact that it is a wire. Interventionalists are used to work with wires and these are well integrated in procedural workflow. Contrary to catheter-based devices (like the CrossBoss, Crosser, laser, WildCat and Enabler-P), the distal tip of wire-based devices can be shaped to increase control while navigating within the CTO. The size of the active guidewire, compared to other technologies, is another key advantage, especially when targeting CTOs in the lower leg or in the coronary arteries where the vascular anatomy is more tortuous and where vessels are smaller. Wire-based crossing devices are also compatible with most of the devices used during a PTA procedure (catheter, balloon, sheath, etc.). Therefore, ease of use is enhanced and the learning curve associated with this new technology is shortened. Contrary to other CTO crossing devices (like the TruePath and WildCat), the active guidewire has no sharp edge. Even though more testing is necessary to demonstrate the benefit of this feature, it is anticipated that perforation and dissection rate associated with the active guidewire could be less. Another unique feature of the proposed technology is its energy type. The proposed system is the first powered wire designed to transmit and deliver mechanical pulses. This energy source (short duration mechanical waves) was used in numerous medical applications and as shown, over the years, to be safe [122, 123, 132, 190]. Moreover, this energy type has demonstrated to be efficient at breaking hard tissue (like kidney stones, vascular calcification and even bone), while being safe on soft and more

compliant tissues. Another key advantage of the proposed technology is the absence of heat accumulation. Considering the low duty cycle of the pulse emission (one pulse of about 2 μs emitted every 100000 μs), it is believed that heat accumulation at the distal tip of the device is negligible. This is important when considering that an elevation of 4°C above normal temperature for five minutes or more could be considered potentially hazardous for human tissue [87]. One last advantage can be associated with the output waveform modulation capability. Even though this feature was not tested in the context of this research, it is conceptually possible to modulate the output pulse shape and repetition rate to facilitate CTO crossing of different tissue compositions.

CHAPTER 6

CONCLUSION (français)

Ce chapitre présente un résumé de la thèse et met en évidence la contribution originale que celle-ci apporte. Les travaux futurs sont aussi présentés à la toute fin.

6.1 Résumé de la thèse

Tel que décrit aux sections 1.1 et 2.1, les occlusions totales chroniques (CTO) sont courantes et problématiques en médecine cardiovasculaire. Les CTOs peuvent être observées dans les membres inférieurs périphériques ainsi que dans les artères coronaires. Les CTOs sont définies comme un blocage complet des artères. Les CTOs sont composées d'un mélange hétérogène de calcium, tissus fibrosé, caillot, dépôts lipidiques et des cellules mortes. Les principales causes menant à un échec d'une procédure de recanalisation percutanée d'un CTO sont la présence de calcification, une tortuosité sévère des artères, la présence d'un cap proximal convexe, la longueur du CTO ainsi qu'un échec précédent. Plusieurs techniques et appareils ont été développés au cours des dernières années. Pourtant, le taux d'échec associé à ce genre de procédure demeure important, ces nouveaux appareils demeurent complexes à opérer et les durées moyennes associées à ce genre de procédure sont toujours aussi élevées. Par conséquent, il existe un besoin non-comblé associé au traitement des CTOs via une procédure de recanalisation percutanée. L'absence d'un appareil simple, efficace et sécuritaire dans le domaine de la recanalisation des CTOs a mené aux travaux de recherche présentés dans cette thèse.

Le but de ces travaux de recherche consistait à développer et démontrer les performances d'un nouvel appareil minimalement invasif pour le traitement des CTO, palliant aux limitations des appareil actuels. Pour ce faire, les objectifs suivants ont été proposés:

1. Concevoir, développer et construire un générateur d'ondes capable de produire des ondes mécaniques de forte amplitude.
2. concevoir, développer et construire un fil guide actif capable de transmettre ces ondes mécaniques jusqu'à une CTO située dans un environnement vasculaire tortueux.
3. Évaluer les performances préliminaires (efficacité et sécurité) de l'appareil (générateur et fil guide actif) à travers une série de tests et d'études ex-vivo et in-vivo.

L'appareil proposé exploite les ondes mécaniques générées, amplifiées et transmises dans des structures solides pour faciliter la recanalisation des CTOs durant une procédure d'angioplastie. L'appareil proposé tire avantage de diverses théories associées avec la propagation des ondes élastiques dans un solide. Par exemple, des ondes mécaniques de faibles amplitudes sont combinées dans l'espace et dans le temps, dans un guide d'ondes solide, pour créer une onde de forte amplitude à l'autre extrémité. Aussi, les pertes acoustiques sont considérées dans le processus de design afin de permettre la transmission et l'émission d'ondes mécaniques de forte amplitude à l'extrémité du fil guide actif en contact avec l'occlusion totale chronique.

Le design de l'appareil proposé a été obtenu en suivant un processus itératif expérimental, tel que décrit à la section 3.1. L'expérience antérieure, la connaissance des théories en lien avec la propagation des ondes et la simulation par éléments finis ont été mis à contribution durant le développement technologique. Les concepts suivants, en lien avec la propagation d'ondes élastiques dans un solide, ont été présentés plus en détail considérant qu'ils sont applicables à l'appareil proposé: propagation des ondes dans un milieu infini, l'effet des conditions frontières sur la propagation des ondes, les effets de diffraction et directivité, la focalisation des ondes, la dispersion, l'atténuation ainsi que les effets non linéaires. Le logiciel d'éléments finis PZFlex a été utilisé pour la création de modèles, la création de maillages et la simulation de différentes configurations. PZFlex est un logiciel utilisé par l'industrie pour le design de transducteurs piézoélectriques, pour l'analyse non-destructive et pour l'imagerie par ultrasons.

L'appareil proposé a été décrit à la section 4.1. L'appareil a deux composantes principales: (i) le générateur d'ondes mécaniques (console) et (ii) le fil guide actif. La console est utilisée pour générer et amplifier les ondes mécaniques tandis que le fil guide actif sert à propager et émettre les ondes mécaniques jusqu'aux CTOs. Les composantes principales du générateur sont les amplificateurs électriques, les transducteurs piézoélectriques, le réflecteur parabolique, le guide d'ondes dispersif et le connecteur mécanique. Les transducteurs piézoélectriques sont utilisés pour convertir les signaux électriques haut voltage des amplificateurs en ondes mécaniques. Le réflecteur parabolique et le guide d'ondes dispersif sont utilisés pour combiner dans l'espace et dans le temps les ondes mécaniques de faibles amplitudes en une seule onde mécanique de forte amplitude et de courte durée (onde de choc). Le design et la construction du fil guide actif sont similaires à ceux de fils guides conventionnels utilisés couramment dans les procédures d'angioplastie. Les principales composantes du fil guide actif sont le réducteur de section, le matériel du fil, le profil du fil à son extrémité distale, le marqueur radio-opaque et les divers revêtements.

Le design du fil guide actif est unique en ce sens qu'il permet la transmission et l'émission d'ondes mécaniques jusqu'aux CTOs. Pour y parvenir, le fil guide actif doit être flexible, résistant, biocompatible et conduire les ondes mécaniques avec le moins d'atténuation possible.

À la section 4.2, les performances préliminaires de l'appareil proposé ont été présentées par rapport à son efficacité et à sa sécurité. Par exemple, la pression de sortie mesurée près de l'extrémité distale du fil guide actif et sa capacité de recanalisation ont été évaluées. De plus, le profil de sécurité de l'appareil a été évalué en analysant la viabilité des cellules endothéliales exposées aux ondes mécaniques ainsi que via une étude animal in-vivo ciblant les artères coronaires de porcs.

Durant le test de mesure de pression, il a été démontré que le signal de pression était composé d'un pulse pression suivi d'un train d'oscillations pour une durée combinée d'environ 30 μs. La demie-durée du pulse principal était d'environ 0.25 μs, tandis que la durée du pulse principal était d'environ 2.15 μs. À une distance de 5 mm de l'extrémité du fil guide actif, une pression (pic à pic) de 0.35 MPa a été mesurée dans l'eau. Il a aussi été démontré que la pression décroît avec une augmentation de la distance par rapport au bout distal et que la zone de pression maximale est localisée près de l'extrémité distale du fil guide actif. La pression n'a pu être mesurée plus près que 2 mm du bout du fil afin d'éviter d'endommager le capteur de pression. Même si la pression maximale n'a pas pu être mesurée, il est anticipé que cette dernière pourrait être supérieure à 1 MPa.

Les tests mesurant la capacité de recanalisation de l'appareil ont été faits sur du Begostone et avec des spécimens ex-vivo de CTO. Le Begostone est un type de plâtre dont les propriétés mécaniques s'apparentent à celles des calcifications vasculaires. Plusieurs tests ont été réalisés dans différentes conditions simulant une procédure de recanalisation. La première étape d'un test de recanalisation consistait à utiliser l'appareil sans énergie. Dans tous les cas, l'appareil ne pouvait pas traverser les différents matériaux sans énergie. Ensuite, la console était activée et le fil guide actif était capable de recanaliser les différents matériaux. Le taux (vitesse) de recanalisation était dépendant des paramètres de la console, de la configuration du fil guide actif, du type de matériaux et des conditions d'utilisation.

Les cellules endothéliales exposées au fil guide actif avec énergie ont démontré une bonne viabilité lorsque comparées avec celles exposées à un appareil de contrôle (fil guide commercial sans énergie). La viabilité des cellules endothéliales a été calculée comme le pourcentage des cellules marquées positivement pour la protéine PECAM-1 par rapport à la

circonférence de la paroi interne de l'artère. En plus, aucun dommage à la paroi artérielle n'a été observé suite à l'analyse histologique.

L'étude animale aigue a permis de démontrer la faisabilité d'envoyer des ondes de choc via un fil guide actif dans les artères coronaires d'un cochon. Les performances techniques et les manipulations du fil guide actif étaient satisfaisantes du point de vue de l'opérateur. Aucun événement cardiaque, noté à l'électrocardiogramme, n'a été observé durant l'activation du fil guide actif. Une perforation causée par le fil guide actif a été observée à l'angiographie, mais sans aucune conséquence sur la santé de l'animal et la suite de la procédure. Les dommages aigus in-vivo des vaisseaux traités ont été évalués en utilisant une méthode novatrice où différentes concentrations d'acétylcholine (Ach) sont injectées dans l'artère. Suite à l'injection d'Ach, il y a vasoconstriction de l'artère et son diamètre est mesuré pour chaque concentration. Toutefois, aucune corrélation n'a pu être établie entre le niveau d'amplitude des ondes mécaniques émises et le diamètre de l'artère après l'injection d'Ach. Les dommages aux artères traitées et la viabilité des cellules endothéliales ont aussi été évalués par histologie. Aucune corrélation n'a pu être établie entre le niveau d'amplitudes des ondes mécaniques émises et la viabilité des cellules endothéliales. Quelques dommages (thrombus et hémorragie dans la parois médiale) ont été observés sur les artères traitées, mais les causes précises n'ont pu être établies. Les dommages observés dans le cadre de cette étude sont typiques des dommages cliniques observés dans les procédures percutanées visant la recanalisation de CTO.

À la section 5.1, les limitations associées aux méthodes expérimentales et à la technologie ont été présentées. Les principales limitations associées à la méthode sont liées avec la méthode de mesure de pression et l'absence d'un test visant à évaluer la quantité et la grosseur des particules libérées lors d'une procédure de recanalisation. Les principales limitations associées à la technologie sont la durabilité du fil guide actif lorsque soumis à l'énergie et les phénomènes associés aux pertes acoustiques lorsque les ondes se propagent. Par ailleurs, l'effet de la géométrie du bout distal du fil guide actif ainsi que la forme de l'onde émise n'ont pas été caractérisées dans le cadre de cette thèse et devraient l'être dans le cadre des travaux futurs.

À la section 5.2, les mécanismes d'action associés à l'appareil proposé ont été discutés. Il a été suggéré que les principaux mécanismes d'action sont: (i) l'effet marteau-piqueur associé aux déplacements du bout du fil guide actif, (ii) le mouvement du fluide à proximité du fil guide actif, (iii) l'absence de chaleur et (iv) la possibilité de différencier les tissus en fonction de leur élasticité. De plus, de la cavitation a été observée dans certains tests et son

rôle comme mécanisme d'action potentiel devrait être évalué de manière plus approfondie dans le cadre de travaux futurs.

Pour terminer, à la section 5.3, les avantages et inconvénients de la technologie proposée ont été décrits et comparés avec ceux des principaux compétiteurs. En plus des limitations mentionnées précédemment, la grosseur et les coûts anticipés de la console devront être réduits dans la prochaine itération. De plus, la présence du réducteur de section à l'extrémité proximal du fil guide actif limite la possibilité d'échanger des cathéters par-dessus le fil guide durant une procédure. Toutefois, il a été démontré que l'appareil proposé offre des caractéristiques uniques par rapport aux autres appareils sur le marché. De plus, cet appareil offre la possibilité d'ajuster et de contrôler le signal de pression en sortie, ce qui pourrait s'avérer utile. Considérant que la technologie proposée utilise un fil guide actif et considérant les mécanismes d'action associés, il est suggéré que cet appareil est facile d'utilisation, efficace et sécuritaire.

Cette thèse a présenté le design d'un nouvel appareil facilitant la recanalisation percutanée des occlusions totales chroniques via la transmission d'ondes mécaniques dans un fil guide. Les performances de cet appareil ont été évaluées à travers une série de tests et d'études pré-cliniques. Des résultats préliminaires encourageants ont été démontrés et suggèrent la poursuite du développement de cette technologie.

6.2 Contribution

La contribution originale de ces travaux de recherche est associée avec la méthode utilisée pour amplifier et transmettre des ondes mécaniques de forte amplitude jusqu'aux CTOs via un fil guide. Selon l'auteur, ces travaux de recherche sont les premiers à décrire l'émission d'ondes mécaniques, via des transducteurs piézoélectriques, qui sont spatialement et temporellement combinées dans un fil mince et flexible pour produire une onde de forte amplitude et de courte durée. De la même manière, ces travaux de recherche sont les premiers à expliquer comment l'émission d'ondes mécaniques pulsées via un fil guide peut faciliter la recanalisation d'occlusions totales chroniques. D'autres appareils utilisant une haute puissance et une faible fréquence ultrasonique ont précédemment été développés pour des applications similaires. Toutefois, ces appareils produisent une augmentation de température, ce qui nécessite l'utilisation d'un système de refroidissement. De plus, ces autres appareils ont un plus grand diamètre (donc plus difficile de se rendre dans des artères tortueuses) et leur pression en sortie ne peut être contrôlée.

6.3 Travaux futurs

Cette thèse résume les travaux de recherche qui se sont majoritairement déroulés entre 2011 et 2015. À la suite des résultats prometteurs décrits précédemment, il a été décidé de poursuivre le développement de cette technologie. À cet effet, une compagnie, SoundBite Medical Solutions, a officiellement été mise en opération en avril 2015. Une équipe multidisciplinaire a été mise en place, incluant des gens avec de l'expérience en développement de produit, en affaires réglementaires, en qualité, en finance et en développement des affaires. Les premières activités de la compagnie ont été de développer un produit sécuritaire et rencontrant les standards réglementaires. Pour cela, des processus de contrôle du design et de la qualité ont été implémentés. Le générateur a été redesigné afin qu'il rencontre le standard IEC 60601 et en utilisant des composantes faites sur mesure. Le fil guide actif a été amélioré et plusieurs tests ont été effectués (biocompatibilité, test sur l'emballage, validation de la stérilisation, étude animale aigue suivant la méthode GLP [1], tests mécaniques standards et tests de simulation). En décembre 2016, une première étude clinique périphérique a été initiée avec un premier patient traité à Sherbrooke avec le SoundBite Crossing System - Peripheral. En mai 2017, la compagnie a obtenu sa certification ISO 13485:2003. Motivée par les résultats très prometteurs de l'étude clinique, celle-ci a été arrêtée en septembre 2017. Un total de 37 patients, dans trois différents sites (Sherbrooke, Montréal et Graz en Autriche), ont été traités avec le SoundBite Crossing System - Peripheral. Aucun événement majeur lié à l'appareil n'a été rapporté durant cette étude. Un taux de succès de 91.9% associé à la facilitation de recanaliser une occlusion totale périphérique a été obtenu avec l'utilisation de l'appareil SoundBite. Avec ces résultats, la compagnie a appliqué pour un marquage CE (commercialisation en Europe) en Octobre 2017. La revue du dossier est toujours en cours. En même temps, SoundBite a aussi développé une version coronarienne du fil guide actif avec une nouvelle étude clinique prévue en 2018. De nouvelles itérations du fil guide actif périphérique sont aussi en recherche et développement (R&D). Ces nouvelles itérations sont conçues afin d'augmenter le niveau d'énergie délivré et la durabilité du fil. De la même manière, une nouvelle console est aussi en développement afin d'augmenter le niveau d'énergie qu'elle peut livrer. Un autre produit, un cathéter actif, est aussi en R&D. La majorité des travaux futurs décrits précédemment ont été ou sont en train d'être réalisés.

En conclusion, l'auteur souhaite remercier, une fois de plus, toutes les personnes qui ont été impliquées ou qui sont impliquées dans ce projet. Cela a été une aventure extraordinaire. Sans votre support, rien de tout cela n'aurait été possible. Merci!

1. GLP = Good Laboratory Practice

CHAPTER 7

CONCLUSION (english)

This chapter provides a thesis summary and outlines the original contribution. Future work is also described.

7.1 Thesis summary

As described in sections 1.1 and 2.1, chronic total occlusion (CTO) is a prevalent and problematic condition in cardiovascular medicine. CTOs can be found in the lower extremities and in the coronary arteries. CTOs are defined as totally occluded arterial segments that have remained occluded for an extended period. CTOs are primarily composed of a heterogeneous mix of calcium, fibrosis, thrombus, lipid deposits and necrotic core. The principal causes of angioplasty CTO crossing failure are the presence of calcification, severe tortuosity, blunt proximal cap morphology, CTO length and prior failed attempt. Many CTO crossing devices and crossing techniques were developed in the last few years. However, the current crossing failure rates, the current devices complexity, the longer associated procedure time and the steep learning curve suggest that there remains an unmet need to address CTO angioplasty. The lack of a simple, effective and safe CTO crossing wire or specialty device has led to the research work described in this thesis.

The goal of this research work was to develop and demonstrate the performance associated with a new minimally invasive CTO crossing system that addresses the limitations of current CTO crossing devices. For this, the following objectives were proposed:

1. Design, develop and build a mechanical wave generator capable of producing high amplitude mechanical waves.
2. Design, develop and build an active guidewire that can transmit mechanical waves up to CTO located in tortuous vascular anatomy.
3. Investigate preliminary safety and efficacy of the system (generator and active guidewire) through various bench tests, ex-vivo and in-vivo studies.

The proposed system exploits mechanical waves that are generated, amplified and transmitted along solid structures to facilitate CTO crossing during an angioplasty procedure. The proposed technology takes advantage of various principles that are associated with the propagation of elastic waves in solid. For example, small amplitude mechanical waves are

spatially and temporally compress in a solid waveguide to create a high amplitude wave. Also, acoustic losses are considered in the design process to allow for transmission and delivery of high amplitude mechanical wave at the end of the active guidewire in contact with the CTO.

The design of the proposed CTO crossing system was obtained following an experimental iterative process, as described in section 3.1. Past experience, knowledge about wave propagation theories and finite element simulations were also considered during the development process. The following concepts associated with the propagation of elastic waves in solid were presented as they are relevant to the proposed technology: wave propagation in an infinite medium, effect of boundary conditions on wave propagation, diffraction and directivity, wave focalization, dispersion, attenuation and nonlinearity. PZFlex finite element software was used to create the model, to create the mesh and to solve the different simulations. PZFlex is commonly used by the industry for the design of piezoelectric transducers and sensors, for non-destructive testing and for medical ultrasound diagnostic imaging.

The proposed CTO crossing system was presented in section 4.1. The crossing system has two main components: (i) the mechanical wave generator (console) and (ii) the active guidewire. The console is used to generate and amplify the mechanical waves, while the active guidewire is used to transmit and deliver these waves at the CTO. The key components of the generator are the electrical amplifiers, the piezoelectric transducers, the parabolic reflector, the dispersive waveguide and the connector. The piezoelectric transducers are used to convert the high power electrical signal form the amplifier into mechanical waves. The parabolic reflector and the dispersive waveguide are used to spatially and temporally compressed the low amplitude mechanical waves into one single large amplitude and short duration mechanical pulse. The design and construction of the active guidewire are similar to commercial guidewires used in endovascular procedures. The key components of the active guidewire are the section reducer, the core wire material, the grind profile, the radiopaque marker and the coatings. The design of the active guidewire is such that it allows the propagation and delivery of the mechanical pulses at the CTO. For this, the active guidewire must be flexible, mechanically resistant, biocompatible and demonstrate good wave transmission.

In section 4.2, the preliminary performance of the proposed CTO crossing system was described from an efficacy and safety point of view. The output pressure near the distal tip of the active guidewire and the crossing ability of the proposed device were measured.

The safety profile of the active guidewire and of the shock wave energy was evaluated by looking at the viability of endothelial cell and in an acute in-vivo animal study.

During the pressure measurement experiment, it was shown that the principal pulse is composed of one peak pulse followed by a series of oscillations for a total duration of about 30 μs. The peak pulse half cycle duration is about 0.25 μs and the peak pulse cycle duration is about 2.15 μs. At a distance of 5 mm in front of the active guidewire, a peak-to-peak pressure of 0.35 MPa was measured in water. It was shown that the pressure decreases with increasing distance from the distal tip of the active guidewire and that the peak pressure zone is located near the tip. Pressure was not measured closer than 2 mm from the distal tip of the active guidewire to prevent damage to the sensor. It is expected that the maximum pressure near the distal tip can reach value above 1 MPa.

Crossing ability tests were performed on Begostone material and on ex-vivo CTO specimens. Begostone plaster-based material was shown to be a good surrogate material for vascular calcification. Different tests were performed in various simulated conditions. The tests were first performed without activation. In all cases without activation, the active guidewire was not able to cross the material. When the shock wave energy was applied, the active guidewire could cross these materials at variable rates depending on the generator settings, simulated conditions and active guidewire configurations.

Endothelial cell exposed to the active guidewire and shock waves showed good viability results when compared to the control article (commercial guidewire without energy). Cell viability was calculated as the percentage of cells staining positively for PECAM-1 by the lumen circumference of the cross section. No vessel wall damage was observed during histology analysis.

The acute in-vivo animal study was successful at demonstrating the feasibility to deliver shock waves via the active guidewire in coronary arteries. Technical handling performance of the device was satisfactory from the operator standpoint. No cardiac events during activation of the device were observed. One vessel perforation was observed angiographically, but without any consequence. Acute in-vivo vessel injury was evaluated using acetylcholine injection followed by QCA measurement. No clear correlation was established between the shock wave amplitude level and the vessel diameter after Ach injection. Vessel injury and endothelial denudation were also evaluated using histology. No clear correlation was established between shock wave amplitude level and endothelial cells viability. Some vessel injuries (thrombus formation and medial hemorrhage) were observed, but it was not pos-

sible to identify the precise cause. It is believed that the vessel injuries reported here are typical of what observed clinically in CTO-PCI procedures.

In section 5.1, limitations associated with the experimental methods and the technology were presented. Key method limitations were associated with the pressure measurement techniques and to the absence of particulate analysis in the performance tests. Key technology limitations were associated with the active guidewire durability and associated energy loss. Also, the impact of the tip geometry and output waveform on the system performance were not characterized in this research and should be evaluated in future work.

In section 5.2, the mechanisms of action associated with the proposed CTO crossing system were discussed. It was hypothesized that the key mechanisms of action are the following: (i) micro-jackhammer effect resulting from the active guidewire tip motion (small displacement and large force), (ii) streaming resulting from the fluid motion, (iii) absence of heat accumulation and (iv) the ability to differentiate tissue based on elasticity properties. In addition, cavitation was observed in specific test conditions and its role as a potential mechanism of action should be further investigate.

Lastly, advantages and disadvantages of the proposed technology were described and compared with competitive devices in section 5.3. Other than the devices limitations mentioned above, the size and anticipated cost of the shock wave generator should be reduced in the next iteration. Also, the large proximal end of active guidewire limits the ability to easily exchange catheter over the device. However, it was shown that the proposed CTO technology offers unique features over commercial devices. Mainly, its wire-based design and its mechanism of action offer great advantage in terms of ease of use, efficacy and safety. In addition, this technology offers the possibility to adjust and control the characteristics of the output pressure waveform, which may come useful.

This thesis presented the design of a new angioplasty CTO crossing device meant to facilitate crossing of chronic total occlusion via the use of mechanical waves transmitted along a guidewire platform. Performance of this device was then evaluated through a series of different bench tests and preclinical studies. Encouraging preliminary efficacy results and safety profile were demonstrated and suggest to continue the development of this technology.

7.2 Contribution

The original contribution of this research work is associated with the method use to amplify, transmit and deliver high amplitude mechanical waves up to a CTO via a wire platform. To the author's knowledge, this is the first reported case where mechanical waves emitted from piezoelectric transducers are spatially and temporally compressed into a small and flexible wire to create a large amplitude and short duration mechanical wave. Similarly, this is the first reported case where it is explained how the delivery of pulsed mechanical energy via a wire can facilitate CTO crossing. Other high-power low-frequency ultrasound devices were developed for similar intended use. However, these devices generate heat and need to be enclosed in a catheter platform with some sort of a cooling system. In addition, these other devices are bulkier (more difficult to reach CTO located in a tortuous anatomy) and their output waveform cannot be modulated.

7.3 Future work

This thesis summarizes the research work that was mostly done between the year 2011 and 2015. Following the promising results that were presented above, it was decided to pursuit the development of the technology. A company, SoundBite Medical Solutions, was officially launched in April 2015 to bring this technology to the next level. A multidisciplinary team was put in place with people having background in product development, regulatory, clinical, quality, finance and business development. The first activities of the company have consisted to develop a product that was safe and that could meet all regulatory standards. For that, design control and quality management were implemented. The shock wave generator was redesigned with the IEC 60601 standard in mind and with custom build components. The active guidewire design was improved and tested extensively (biocompatibility, packaging, sterilization, acute animal GLP [1] study, standard mechanical tests and simulated use tests). In December 2016, a First-In-Man (FIM) clinical study was initiated and a first subject was treated with the SoundBite Crossing System - Peripheral at the Centre Hospitalier Universitaire de Sherbrooke. In May 2017, the company obtained its ISO 13485:2003 certification. Motivated by the impressive safety and efficacy results obtained, the FIM study was stopped in September 2017. A total of 37 subjects, from three different sites (Sherbrooke, Montreal and Graz in Austria), were treated with the SoundBite Crossing System - Peripheral. No device related major adverse event were reported. Facilitating crossing of peripheral CTOs was achieved in 91.9% with the use of this SoundBite crossing system. With these results, SoundBite applied for a CE mark in

1. GLP = Good Laboratory Practice

October 2017 for this first device. CE mark was obtained in March 2018. Simultaneously, SoundBite is working of the coronary version of the SoundBite Crossing System. New iterations of the peripheral wire are in the research and development (R&D) phase. These new versions are designed to improve energy delivery and increase device endurance. The development of a new console iteration is ongoing to improve energy delivery and to reduce its footprint. Another product, the active catheter, is also in the early stage of R&D. Majority of the future work described in chapter 5 were or are being addressed.

In conclusion, the author would like to thank one more time all the people that were or are still involved in this project. It has been a crazy and amazing ride. Without your support and help, none of this would have been possible. Thank you!

LIST OF REFERENCES

[1] Achenbach, J., Lauwerier, H. and Koiter, W. (2016). *Wave Propagation in Elastic Solids*. North-Holland series in applied mathematics and mechanics, Elsevier Science.

[2] Adams, C., McLaughlan, J., Nie, L. and Freear, S. (2017). Excitation and acquisition of cranial guided waves using a concave array transducer. *Proc. Mtgs. Acoust.*, volume 30, number 1, pp. 1–11.

[3] Ai, Y. L., Liu, L., He, W., Liang, B. L. and Xu, J. L. (2011). Influence of microstructure of tc11 titanium alloy on ultrasonic velocity and attenuation. *Advanced Materials Research*, volume 337, pp. 719–723.

[4] Ai, Y. L., Liu, L., He, W., Liang, B. L. and Xu, J. L. (2012). Influence of microstructure of tc4 titanium alloy on ultrasonic velocity and attenuation. *Applied Mechanics and Materials*, volume 117, pp. 1766–1769.

[5] Al-Ameri, H., Clavijo, L., Matthews, R., Kkoner, R. and Shavelle, D. (2012). Devices to treat peripheral chronic total occlusions. *Journal of Interventional Cardiology*, volume 25, number 4, pp. 395–403.

[6] Al-Mukhaini, M., Panduranga, P., Sulaiman, K., Riyami, A. A., Deeb, M. and Riyami, M. B. (2011). Coronary perforation and covered stents: An update and review. *Heart Views : The Official Journal of the Gulf Heart Association*, volume 12, number 2, pp. 63–70.

[7] Amann, K. (2008). Media calcification and intima calcification are distinct entities in chronic kidney disease. *Clinical journal of the American Society of Nephrology : CJASN*, volume 3, pp. 1599–605.

[8] Asahi (No date). *Technical document about Asahi Neo's guidewire (online presentation)* (Technical report).

[9] Association for the Advancement of Medical Instrumentation (1010). *AAMI TIR42 - Evaluation of particulates associated with vascular medical devices* (Technical report).

[10] ASTM (2010). *C20 Test Methods for Apparent Porosity, Water Absorption, Apparent Specific Gravity, and Bulk Density of Burned Refractory Brick and Shapes by Boiling Water* (Technical report).

[11] Azar, L., Shi, Y. and Wooh, S.-C. (2000). Beam focusing behavior of linear phased arrays. *NDT & E International*, volume 33, number 3, pp. 189–198.

[12] Aziz, S. and Ramsdale, D. R. (2005). Chronic total occlusions–a stiff challenge requiring a major breakthrough: is there light at the end of the tunnel? *Heart*, volume 91, number suppl 3, p. iii42.

[13] Azo materials (2017). Grade 10 Ti-11.5Mo-6Zr-4.5Sn - Titanium Beta III (UNS R58030). https://www.azom.com/article.aspx?ArticleID=9903 (accessed on December 8, 2017).

[14] Babcock, D. E., Hergenrother, R. W., Craig, D. A., Kolodgie, F. D. and Virmani, R. (2013). InÂăvivo distribution of particulate matter from coated angioplasty balloon catheters. *Biomaterials*, volume 34, number 13, pp. 3196–3205.

[15] Balasubramanian, T. S., Balasubramanian, V. and Muthu Manickam, M. A. (2011). Fatigue crack growth behaviour of gas tungsten arc, electron beam and laser beam welded ti-6al-4v alloy. *Materials & Design*, volume 32, number 8, pp. 4509–4520.

[16] Banerjee, S. (2017). *Practical Approach to Peripheral Arterial Chronic Total Occlusions*. Springer Singapore.

[17] Banerjee, S., Das, T. S., Abu-Fadel, M. S., Dippel, E. J., Shammas, N. W., Tran, D. L., Zankar, A., Varghese, C., Kelly, K. C., Weideman, R. A., Little, B. B., Reilly, R. F., Addo, T. and Brilakis, E. S. (2012). Pilot trial of cryoplasty or conventional balloon post-dilation of nitinol stents for revascularization of peripheral arterial segments: The cobra trial. *Journal of the American College of Cardiology*, volume 60, number 15, pp. 1352–1359.

[18] Banerjee, S., Jeon-Slaughter, H., Tsai, S., Mohammad, A., Foteh, M., Abu-Fadel, M., Gigliotti, O. S., Cawich, I., Rodriguez, G., Kumbhani, D., Addo, T., Luna, M., Das, T. S., Prasad, A., Armstrong, E. J., Shammas, N. W. and Brilakis, E. S. (2016). Comparative assessment of procedure cost and outcomes between guidewire and crossing device strategies to cross peripheral artery chronic total occlusions. *JACC. Cardiovascular interventions*, volume 9, pp. 2243–2252.

[19] Banerjee, S., Master, R. G., Peltz, M., Willis, B., Mohammed, A., Little, B. B., DiMaio, M. J., Jessen, M. E. and Brilakis, E. S. (2012). Influence of chronic total occlusions on coronary artery bypass graft surgical outcomes. *Journal of Cardiac Surgery*, volume 27, number 6, pp. 662–667.

[20] Banerjee, S., Sarode, K., Patel, A., Mohammad, A., Parikh, R., Armstrong, E. J., Tsai, S., Shammas, N. W. and Brilakis, E. S. (2015). Comparative assessment of guidewire and microcatheter vs a crossing device-based strategy to traverse infrainguinal peripheral artery chronic total occlusions. *Journal of endovascular therapy : an official journal of the International Society of Endovascular Specialists*, volume 22, pp. 525–34.

[21] Bard Peripheral (—). Crosser CTO Recanalization Catheters. http://www.bardpv.com/portfolio/crossercto/ (accessed on January 11, 2018).

[22] Bardaji, A., Rodriguez-Lopez, J. and Torres-Sanchez, M. (2014). Chronic total occlusion: To treat or not to treat. *World Journal of Cardiology*, volume 6, number 7, pp. 621–629.

[23] Bardeesi, A. S. A., Gao, J., Zhang, K., Yu, S., Wei, M., Liu, P. and Huang, H. (2017). A novel role of cellular interactions in vascular calcification. *Journal of translational medicine*, volume 15, p. 95.

[24] Bazergui, A. (2002). *Résistance des matériaux*. Presses internationales Polytechnique.

[25] Beard, P. C., Hurrell, A., Van Den Elzen, E. and Mills, T. N. (1998). Comparison of a miniature, ultrasonic, optical fibre hydrophone with pvdf hydrophone technology. Volume 2. IEEE, pp. 1881–1884.

[26] Becker, A., Epple, M., Muller, K. and Schmitz, I. (2004). A comparative study of clinically well-characterized human atherosclerotic plaques with histological, chemical, and ultrastructural methods. *Journal of Inorganic Biochemistry*, volume 98, number 12, pp. 2032–2038.

[27] Bego (—). *BegoStone plus - High-strength dental stone with high hardness and low expansion, scannable - Instruction for use* (Technical report).

[28] Benko, A., Berube, S., Buller, C. E., Dion, S., Riel, L.-P., Brouillette, M. and Genereux, P. (2017). Novel crossing system for chronic total occlusion recanalization: First-in-man experience with the soundbite crossing system. *The Journal of invasive cardiology*, volume 29, pp. E17–E20.

[29] Bentzon, J. F., Otsuka, F., Virmani, R. and Falk, E. (2014). Mechanisms of plaque formation and rupture. *Circulation research*, volume 114, pp. 1852–66.

[30] Bertrand, M.-J., Riel, L.-P., Dion, S., Geoffroy, P., Clavet-Lanthier, M.-E., Brouillette, M. and Tanguay, J.-F. (2016). Safety and feasibility study of a device using guidewire-mediated shock waves to treat chronic total occlusions (CTO) of coronary arteries. In *Interventional Cardiology - Montreal*.

[31] Bessonova, O. V., Khokhlova, V. A., Bailey, M. R., Canney, M. S. and Crum, L. A. (2009). Focusing of high power ultrasound beams and limiting values of shock wave parameters. *Acoustical Physics*, volume 55, number 4, pp. 463–473.

[32] Bhardwaj, M. (2008). Piezoelectric transducer with gas matrix, United States patent 7,382,082.

[33] Bhargav, D. (2016). Recanalization of chronic total occlusion lesions: A critical appraisal of current devices and techniques. *Journal of clinical and diagnostic research*, volume 10, pp. OE01–OE07.

[34] Bishop, P. D., Feiten, L. E., Ouriel, K., Nassoiy, S. P., Pavkov, M. L., Clair, D. G. and Kashyap, V. S. (2008). Arterial calcification increases in distal arteries in patients with peripheral arterial disease. *Annals of Vascular Surgery*, volume 22, number 6, pp. 799–805.

[35] Bolia, A., Miles, K. A., Brennan, J. and Bell, P. R. F. (1990). Percutaneous transluminal angioplasty of occlusions of the femoral and popliteal arteries by subintimal dissection. *CardioVascular and Interventional Radiology*, volume 13, number 6, pp. 357–363.

[36] Bosiers, M., Diaz-Cartelle, J., Scheinert, D., Peeters, P. and Dawkins, K. D. (2014). Revascularization of lower extremity chronic total occlusions with a novel intraluminal recanalization device: Results of the reopen study. *Journal of Endovascular Therapy*, volume 21, number 1, pp. 61–70.

[37] Boston Scientific (—). Truepath - Chronic Total Occlusion Device. `http://www.bostonscientific.com/en-US/products/cto-systems/truepath-cto-device.html` (accessed on January 11, 2018).

[38] Boström, K. I. (2016). Where do we stand on vascular calcification? *Vascular Pharmacology*, volume 84, number Supplement C, pp. 8–14.

[39] Brentnall, M. D., Martin, R. W., Vaezy, S., Kaczkowski, P., Forster, F. and Crum, L. (2001). A new high intensity focused ultrasound applicator for surgical applications. *IEEE Transactions on Ultrasonics, Ferroelectrics, and Frequency Control*, volume 48, number 1, pp. 53–63.

[40] Brilakis, E. S. (2017). Randomized Comparison of a CrossBoss First vs. Standard Wire Escalation Strategy for Crossing Coronary Chronic Total Occlusions: the CrossBoss First trial. In *TCT Conference*.

[41] Brilakis, E. S., Banerjee, S., Karmpaliotis, D., Lombardi, W. L., Tsai, T. T., Shunk, K. A., Kennedy, K. F., Spertus, J. A., Holmes, D. R. J. and Grantham, J. A. (2015). Procedural outcomes of chronic total occlusion percutaneous coronary intervention: a report from the ncdr (national cardiovascular data registry). *JACC. Cardiovascular interventions*, volume 8, pp. 245–53.

[42] Brilakis, E. S., Grantham, J. A., Rinfret, S., Wyman, R. M., Burke, M. N., Karmpaliotis, D., Lembo, N., Pershad, A., Kandzari, D. E., Buller, C. E., DeMartini, T., Lombardi, W. L. and Thompson, C. A. (2012). A percutaneous treatment algorithm for crossing coronary chronic total occlusions. *JACC: Cardiovascular Interventions*, volume 5, number 4, pp. 367–379.

[43] Brouillette, M., Dion, S. and Riel, L. P. (2013). Mechanical wave generator and method thereof, United States patent 13,819,575.

[44] Brujan, E.-A. (2000). Collapse of cavitation bubbles in blood. *Europhysics Letters*, volume 50, number 2, p. 175.

[45] Buller, C. E. (2013). Coronary guidewires for chronic total occlusion procedures: function and design. *Interventional Cardiology*, volume 5, number 5, pp. 533–540.

[46] Chandrasekar, B., Nattel, S. and Tanguay, J.-F. (2001). Coronary artery endothelial protection after local delivery of 17β-estradiol during balloon angioplasty in a porcine model: a potential new pharmacologic approach to improve endothelial function. *Journal of the American College of Cardiology*, volume 38, number 5, pp. 1570–1576.

[47] Chandrasekar, B., Sirois, M. G., Geoffroy, P., Lauzier, D., Nattel, S. and Tanguay, J.-F. (2005). Local delivery of 17β-estradiol improves reendothelialization and decreases inflammation after coronary stenting in a porcine model. *Thrombosis and Haemostasis*, volume 94, number 5, pp. 1042–1047.

[48] Christopoulos, G., Kandzari, D. E., Yeh, R. W., Jaffer, F. A., Karmpaliotis, D., Wyman, M. R., Alaswad, K., Lombardi, W., Grantham, J. A., Moses, J., Christakopoulos, G., Tarar, M. N. J., Rangan, B. V., Lembo, N., Garcia, S., Cipher, D., Thompson, C. A., Banerjee, S. and Brilakis, E. S. (2016). Development and validation of a novel scoring system for predicting technical success of chronic total occlusion percutaneous coronary interventions. *JACC: Cardiovascular Interventions*, volume 9, number 1, pp. 1–9.

[49] Christopoulos, G., Wyman, R. M., Alaswad, K., Karmpaliotis, D., Lombardi, W., Grantham, J. A., Yeh, R. W., Jaffer, F. A., Cipher, D. J., Rangan, B. V., Christakopoulos, G. E., Kypreos, M. A., Lembo, N., Kandzari, D., Garcia, S., Thompson, C. A., Banerjee, S. and Brilakis, E. S. (2015). Clinical utility of the japan–chronic total occlusion score in coronary chronic total occlusion interventions. *Circulation: Cardiovascular Interventions*, volume 8, number 7.

[50] Cimino, W. W. (1999). The physics of soft tissue fragmentation using ultrasonic frequency vibration of metal probes. *Clinics in plastic surgery*, volume 26, pp. 447–61.

[51] Clauer, A. H., Holbrook, J. H. and Fairand, B. P. (1981). Effects of laser induced shock waves on metals. In *Shock Waves and High-Strain-Rate Phenomena in Metals: Concepts and Applications*. Springer US, Boston, MA, pp. 675–702.

[52] Conti, C. (2013). *The Netter Collection of Medical Illustrations*. Number v. 8 in Netter Green Book Collection, Elsevier Health Sciences.

[53] Cordis (—). FRONTRUNNER XP CTO Catheter. `https://emea.cordis.com/emea/endovascular/lower-extremity-solutions/cross/frontrunner-xp-cto-catheter.html` (accessed on January 11, 2018).

[54] CRT Online (–). The ENABLER-P – A Novel CTO Crossing System. `http://www.crtonline.org/presentation-detail/enabler-p-novel-cto-crossing-system` (accessed on February 3, 2018).

[55] Danilchenko, S. N., Kuznetsov, V. N., Stanislavov, A. S., Kalinkevich, A. N., Starikov, V. V., Moskalenko, R. A., Kalinichenko, T. G., Kochenko, A. V., Lu, J., Shang, J. and Yang, S. (2013). The mineral component of human cardiovascular

deposits: morphological, structural and crystal-chemical characterization. *Crystal Research and Technology*, volume 48, number 3, pp. 153–162.

[56] Dash, D. (2016). Guidewire crossing techniques in coronary chronic total occlusion intervention: A to z. *Indian Heart Journal*, volume 68, number 3, pp. 410–420.

[57] Delgadillo, J. O. V., Delorme, S., El-Ayoubi, R., DiRaddo, R. and Hatzikiriakos, S. G. (2010). Effect of freezing on the passive mechanical properties of arterial samples. *Journal of Biomedical Science & Engineering*, volume 3, number 7, pp. 645 – 652.

[58] Demer, L. L. and Tintut, Y. (2008). Vascular calcification: Pathobiology of a multifaceted disease. *Circulation*, volume 117, number 22, pp. 2938–2948.

[59] Dion, S. (2006). *Conception, fabrication et essai d'un émetteur/récepteur unidimentionnel pour un lithotriteur extracorporel à ondes de choc intelligent*. Master's thesis, Université de Sherbrooke.

[60] Dion, S. (2014). Technical communication with Steven Dion (not yet published).

[61] Donachie, M. J. (2000). *Titanium: A Technical Guide, 2nd Edition*. ASM International.

[62] Dwivedi, A., Gupta, R. K., Varma, R. K. and Narayanan, K. S. (2016). Effect of processing and microstructure on ultrasonic response of aerospace alloys: An overview. *Russian Journal of Nondestructive Testing*, volume 52, number 12, pp. 703–709.

[63] Ebenstein, D. M., Coughlin, D., Chapman, J., Li, C. and Pruitt, L. A. (2009). Nanomechanical properties of calcification, fibrous tissue, and hematoma from atherosclerotic plaques. *Journal of Biomedical Materials Research Part A*, volume 91A, number 4, pp. 1028–1037.

[64] Elmansy, H. E. and Lingeman, J. E. (2016). Recent advances in lithotripsy technology and treatment strategies: A systematic review update. *International Journal of Surgery*, volume 36, number Part D, pp. 676–680.

[65] Esch, E., Simmons, W., Sankin, G., Cocks, H., Preminger, G. and Zhong, P. (2010). A simple method for fabricating artificial kidney stones of different physical properties. *Urological Research*, volume 38, pp. 315–319.

[66] Fefer, P., Knudtson, M. L., Cheema, A. N., Galbraith, P. D., Osherov, A. B., Yalonetsky, S., Gannot, S., Samuel, M., Weisbrod, M., Bierstone, D., Sparkes, J. D., Wright, G. A. and Strauss, B. H. (2012). Current perspectives on coronary chronic total occlusions: The canadian multicenter chronic total occlusions registry. *Journal of the American College of Cardiology*, volume 59, number 11, pp. 991–997.

[67] Fink, M., Montaldo, G. and Tanter, M. (2003). Time-reversal acoustics in biomedical engineering. *Annual Review of Biomedical Engineering*, volume 5, number 1, pp. 465–497.

[68] Food and Drug Administration (1995). *Coronary and Cerebrovascular Guidewire Guidance* (Technical report).

[69] Food and Drug Administration (2008). *Guidance for Industry - Coronary Drug-Eluting Stents, Nonclinical and Clinical Studies* (Technical report).

[70] Food and Drug Administration (2010). *Guidance for Industry and FDA Staff - Non-Clinical Engineering Tests and Recommended Labeling for Intravascular Stents and Associated Delivery Systems* (Technical report).

[71] Food and Drug Administration (2013). *Use of International Standard ISO 10993-1, "Biological evaluation of medical devices - Part 1: Evaluation and testing within a risk management process" - Guidance for Industry and Food and Drug Administration Staff* (Technical report).

[72] Food and Drug Association (2015). Intravascular Medical Devices: FDA Safety Communication - Lubricious Coating Separation. `https://www.fda.gov/Safety/MedWatch/SafetyInformation/SafetyAlertsforHumanMedicalProducts/ucm473924.htm` (accessed on December 16, 2017).

[73] Food and Drug Association (2017). Premarket notification for the DABRA Laser System (DABRA Laser model RA-308 and DABRA Catheter model 101) - Traditional 510(k) summary (K170349).

[74] Fort Wayne Metals (2017). Nitinol#1. `http://www.fwmetals.com/services/resource-library/nitinol-1/` (accessed on December 3, 2017).

[75] Fort Wayne Metals (2017). Stainless steeel 304v. `http://www.fwmetals.com/services/resource-library/304V/` (accessed on December 3, 2017).

[76] Galassi, A. R., Boukhris, M., Azzarelli, S., Castaing, M., Marza, F. and Tomasello, S. D. (2016). Percutaneous coronary revascularization for chronic total occlusions: A novel predictive score of technical failure using advanced technologies. *JACC: Cardiovascular Interventions*, volume 9, number 9, pp. 911–922.

[77] Gao, X.-L., Zhang, L.-J., Liu, J. and Zhang, J.-X. (2013). A comparative study of pulsed nd:yag laser welding and tig welding of thin ti6al4v titanium alloy plate. *Materials Science and Engineering: A*, volume 559, number Supplement C, pp. 14–21.

[78] Gavin, G. P., McGuinness, G. B., Dolan, F. and Hashmi, M. S. J. (2007). Performance characteristics of a therapeutic ultrasound wire waveguide apparatus. *International Journal of Mechanical Sciences*, volume 49, number 3, pp. 298–305.

[79] Giancoli, D. (2014). *Physics: Principles with Applications*. Physics: Principles with Applications, Pearson.

[80] Godino, C., Sharp, A. S. P., Carlino, M. and Colombo, A. (2009). Crossing ctos–the tips, tricks, and specialist kit that can mean the difference between success and failure. *Cathet. Cardiovasc. Intervent.*, volume 74, number 7, pp. 1019–1046.

[81] Goueffic, Y. (2016). The piculet recanalization device for peripheral cto. In *LINC*.

[82] Government of Canada (2017). Heart disease in canada. `https://www.canada.ca/en/public-health/services/publications/diseases-conditions/heart-disease-canada.html` (accessed on November 4, 2017).

[83] Graff, K. (2012). *Wave Motion in Elastic Solids*. Dover Books on Physics, Dover Publications.

[84] Grantham, J. A., Marso, S. P., Spertus, J., House, J., Holmes, D. R. and Rutherford, B. D. (2009). Chronic total occlusion angioplasty in the united states. *JACC: Cardiovascular Interventions*, volume 2, number 6, pp. 479–486.

[85] Grundeken, M. J., Li, X., Kurpershoek, C. E., Kramer, M. C., Vink, A., Piek, J. J., Tijssen, J. G. P., Koch, K. T., Wykrzykowska, J. J., de Winter, R. J. and van der Wal, A. C. (2015). Distal embolization of hydrophilic-coating material from coronary guidewires after percutaneous coronary interventions. *Circulation: Cardiovascular Interventions*, volume 8, number 2, pp. e001816–e001816.

[86] Hallow, D. M., Mahajan, A. D. and Prausnitz, M. R. (2007). Ultrasonically targeted delivery into endothelial and smooth muscle cells in ex vivo arteries. *Journal of Controlled Release*, volume 118, number 3, pp. 285–293.

[87] Health Canada (–). Guidelines for the Safe Use of Diagnostic Ultrasound. `http://www.hc-sc.gc.ca/ewh-semt/alt_formats/hecs-sesc/pdf/pubs/radiation/01hecs-secs255/01hecs-secs255-eng.pdf` (accessed on February 10, 2018).

[88] Heart & Stroke (2016). What is atherosclerosis? `http://www.heartandstroke.ca/heart/conditions/atherosclerosis` (accessed on January 9, 2018).

[89] Heimbach, D., Munver, R., Zhong, P., Jacobs, J., Hesse, A., Müller, S. and Preminger, G. (2000). Acoustic and mechanical properties of artificial stones in comparison to natural kidney stones. *The Journal of Urology*, volume 164, number 2, pp. 537–544.

[90] Ikeda, T., Yoshizawa, S., Tosaki, M., Allen, J. S., Takagi, S., Ohta, N., Kitamura, T. and Matsumoto, Y. (2006). Cloud cavitation control for lithotripsy using high intensity focused ultrasound. *Ultrasound in Medicine & Biology*, volume 32, number 9, pp. 1383–1397.

[91] Ilan, A. and Weight, J. P. (1990). The propagation of short pulses of ultrasound from a circular source coupled to an isotropic solid. *The Journal of the Acoustical Society of America*, volume 88, number 2, pp. 1142–1151.

[92] Iliopoulos, S. N., Aggelis, D. G. and Polyzos, D. (2016). Wave dispersion in fresh and hardened concrete through the prism of gradient elasticity. *International Journal of Solids and Structures*, volume 78-79, pp. 149–159.

[93] International Organization for Standardization (2009). *ISO 10993-1 Biological evaluation of medical devices – Part 1: Evaluation and testing within a risk management process* (Technical report).

[94] International Organization for Standardization (2014). *ISO 11070 Sterile single-use intravascular introducers, dilators and guidewires* (Technical report).

[95] Joyal, D., Afilalo, J. and Rinfret, S. (2010). Effectiveness of recanalization of chronic total occlusions: a systematic review and meta-analysis. *American heart journal*, volume 160, pp. 179–87.

[96] Kanno, D., Tsuchikane, E., Nasu, K., Katoh, O., Kashima, Y., Kaneko, U., Fujita, T., Suzuki, Y. and Suzuki, T. (2017). Initial results of a first-in-human study on the PlasmaWire™ system, a new radiofrequency wire for recanalization of chronic total occlusions. *Catheterization and Cardiovascular Interventions*.

[97] Khatri, J., Abdallah, M. and Ellis, S. (2017). Management of coronary chronic total occlusion. *Cleveland Clinic Journal of Medicine*, volume 84, number 12 suppl 3, pp. 27–38.

[98] Kipshidze, N., Dangas, G., Tsapenko, M., Moses, J., Leon, M. B., Kutryk, M. and Serruys, P. (2004). Role of the endothelium in modulating neointimal formation: Vasculoprotective approaches to attenuate restenosis after percutaneous coronary interventions. *Journal of the American College of Cardiology*, volume 44, number 4, pp. 733–739.

[99] Kolsky, H. (2003). *Stress Waves in Solids*. Dover phoenix editions, Dover Publications.

[100] Kumar, V., Abbas, A., Fausto, N. and Aster, J. (2009). *Robbins and Cotran Pathologic Basis of Disease*. Robbins Pathology, Elsevier Health Sciences.

[101] Ladwiniec, A., Allgar, V., Thackray, S., Alamgir, F. and Hoye, A. (2015). Medical therapy, percutaneous coronary intervention and prognosis in patients with chronic total occlusions. *Heart*, volume 101, number 23, p. 1907.

[102] Laird, J., Joye, J., Sachdev, N., Huang, P., Caputo, R., Mohiuddin, I., Runyon, J. and Das, T. (2014). Recanalization of infrainguinal chronic total occlusions with the crosser system: results of the patriot trial. *The Journal of invasive cardiology*, volume 26, pp. 497–504.

[103] Laird, J. R., Zeller, T., Gray, B. H., Scheinert, D., Vranic, M., Reiser, C., Biamino, G. and Investigators, L. (2006). Limb salvage following laser-assisted angioplasty for critical limb ischemia: results of the laci multicenter trial. *Journal of endovascular therapy : an official journal of the International Society of Endovascular Specialists*, volume 13, pp. 1–11.

[104] Laugier, P. and HaÃŕat, G. (2011). *Bone Quantitative Ultrasound*. Springer Netherlands.

[105] Lautrup, B. (2011). *Physics of Continuous Matter, Second Edition: Exotic and Everyday Phenomena in the Macroscopic World*. Taylor & Francis.

[106] LeGeros, R. (2001). Formation and transformation of calcium phosphates: relevance to vascular calcification. *Zeitschrift fur Kardiologie*, volume 90, number 3, pp. 116–124.

[107] Leighton, T. G. (2007). What is ultrasound? *Progress in Biophysics and Molecular Biology*, volume 93, number 1, pp. 3–83.

[108] Liang, G. Z. and Zhang, F. X. (2013). Novel devices and specialized techniques in recanalization of peripheral artery chronic total occlusions (ctos) – a literature review. *International Journal of Cardiology*, volume 165, number 3, pp. 423–429.

[109] Liu, X., Chu, P. K. and Ding, C. (2004). Surface modification of titanium, titanium alloys, and related materials for biomedical applications. *Materials Science and Engineering: R: Reports*, volume 47, number 3, pp. 49–121.

[110] Liu, Y., Wear, K. A. and Harris, G. R. (2017). Uncertainty of high intensity therapeutic ultrasound (hitu) field characterization with hydrophones: Effects of nonlinearity, spatial averaging, and complex sensitivity. *Ultrasound in medicine & biology*, volume 43, number 10, pp. 2329–2342.

[111] Liu, Y. and Zhong, P. (2002). Begostone—a new stone phantom for shock wave lithotripsy research (l). *The Journal of the Acoustical Society of America*, volume 112, number 4, pp. 1265–1268.

[112] London, N. J. M., Srinivasan, R., Naylor, A. R., Hartshorne, T., Ratliff, D. A., Bell, P. R. F. and Bolia, A. (1994). Subintimal angioplasty of femoropopliteal artery occlusions: The long-term results. *European Journal of Vascular Surgery*, volume 8, number 2, pp. 148–155.

[113] Lovell, M., Harris, K., Forbes, T., Twillman, G., Abramson, B., Criqui, M. H., Schroeder, P., Mohler, E. R. and Hirsch, A. T. (2009). Peripheral arterial disease: Lack of awareness in canada. *Canadian Journal of Cardiology*, volume 25, number 1, pp. 39–45.

[114] Lucas, B. G. and Muir, T. G. (1982). The field of a focusing source. *The Journal of the Acoustical Society of America*, volume 72, number 4, pp. 1289–1296.

[115] Ludian, T. and Wagner, L. (2008). Mechanical surface treatments for improving fatigue behavior in titanium alloys. *Advances in Materials Sciences*, volume 8, number 2, pp. 44–52.

[116] Makin, I. R. S. and Everbach, E. C. (1996). Measurement of pressure and assessment of cavitation for a 22.5âĂŘkhz intraâĂŘarterial angioplasty device. *The Journal of the Acoustical Society of America*, volume 100, number 3, pp. 1855–1864.

[117] Markose, G., Miller, F. N. A. C. and Bolia, A. (2010). Subintimal angioplasty for femoro-popliteal occlusive disease. *Journal of Vascular Surgery*, volume 52, number 5, pp. 1410–1416.

[118] Matweb - Material Property Data (2017). Titanium Ti-6Al-4V (Grade 5), Annealed. `http://www.matweb.com/search/DataSheet.aspx?MatGUID=a0655d261898456b958e5f825ae85390` (accessed on December 3, 2017).

[119] Mauri, L., Rogers, C. and Baim, D. S. (2006). Devices for distal protection during percutaneous coronary revascularization. *Circulation*, volume 113, number 22, pp. 2651–2656.

[120] McGuinness, G. B., Wylie, M. P. and Gavin, G. P. (2010). Ablation of chronic total occlusions using kilohertz-frequency mechanical vibrations in minimally invasive angioplasty procedures. *Critical Reviews in Biomedical Engineering*, volume 38, number 6.

[121] Mebs, R. W., Darr, J. H. and Grimsley, J. D. (1953). Metal ultrasonic delay lines. *Journal of Research of the National Bureau of Standards*, volume 51, number 5, pp. 209–220.

[122] Miller, D., Smith, N., Bailey, M., Czarnota, G., Hynynen, K., Makin, I. and of Ultrasound in Medicine Bioeffects Committee, A. I. (2012). Overview of therapeutic ultrasound applications and safety considerations. *Journal of ultrasound in medicine : official journal of the American Institute of Ultrasound in Medicine*, volume 31, number 4, pp. 623–634.

[123] Mitragotri, S. (2005). Healing sound: the use of ultrasound in drug delivery and other therapeutic applications. *Nature Reviews Drug Discovery*, volume 4, p. 255.

[124] Mohr, F. W., Morice, M.-C., Kappetein, A. P., Feldman, T. E., Stahle, E., Colombo, A., Mack, M. J., Holmes, D. R., Morel, M.-a., Dyck, N. V., Houle, V. M., Dawkins, K. D. and Serruys, P. W. (2013). Coronary artery bypass graft surgery versus percutaneous coronary intervention in patients with three-vessel disease and left main coronary disease: 5-year follow-up of the randomised, clinical syntax trial. *The Lancet*, volume 381, number 9867, pp. 629–638.

[125] Montaldo, G., Roux, P., Derode, A., Negreira, C. and Fink, M. (2001). Generation of very high pressure pulses with 1-bit time reversal in a solid waveguide. *The Journal of the Acoustical Society of America*, volume 110, number 6, pp. 2849–2857.

[126] Munce, N. R., Yang, V. X. D., Standish, B. A., Qiang, B., Butany, J., Courtney, B. K., Graham, J. J., Dick, A. J., Strauss, B. H., Wright, G. A. and Vitkin, I. A. (2007). Ex vivo imaging of chronic total occlusions using forward-looking optical coherence tomography. *Lasers in surgery and medicine*, volume 39, pp. 28–35.

[127] Nazarchuk, Z., Skalskyi, V., Serhiyenko, O., Nazarchuk, Z. and Skalskyi, V. (2017). *Acoustic Emission*. Springer.

[128] Nicholson, N. C., McDicken, W. N., Watson, L. M. and Jervis, J. (1994). Effects of anneal upon transmission loss and mode group velocity in polycrystalline metal wires. *The Journal of the Acoustical Society of America*, volume 95, number 2, pp. 836–848.

[129] Niinomi, M. (2007). Fatigue characteristics of metallic biomaterials. *International Journal of Fatigue*, volume 29, number 6, pp. 992–1000.

[130] Nitta, K. (2011). Vascular calcification in patients with chronic kidney disease. *Therapeutic Apheresis and Dialysis*, volume 15, number 6, pp. 513–521.

[131] Norgren, L., Hiatt, W. R., Dormandy, J. A., Nehler, M. R., Harris, K. A. and Fowkes, F. G. R. (2007). Inter-society consensus for the management of peripheral arterial disease (tasc ii). *European Journal of Vascular and Endovascular Surgery*, volume 33, number 1, Supplement, pp. S1–S75.

[132] O'Daly, B. J., Morris, E., Gavin, G. P., OâĂŹByrne, J. M. and McGuinness, G. B. (2008). High-power low-frequency ultrasound: A review of tissue dissection and ablation in medicine and surgery. *Journal of Materials Processing Technology*, volume 200, number 1, pp. 38–58.

[133] Oliver, W. and Pharr, G. (1992). An improved technique for determining hardness and elastic modulus using load and displacement sensing indentation experiments. *Materials research society*, volume 7, pp. 1564–1583.

[134] Olympus (–). Beam Characteristics. `https://www.olympus-ims.com/en/ndt-tutorials/transducers/characteristics/` (accessed on January 21, 2018).

[135] Onda Corporation (2017). Tables of acoustic properties of materials. `http://www.ondacorp.com/tecref_acoustictable.shtml` (accessed on December 2, 2017).

[136] Opolski, M. P. and Achenbach, S. (2015). CT angiography for revascularization of CTO. *JACC: Cardiovascular Imaging*, volume 8, number 7, pp. 846–858.

[137] Orlic, D., Stankovic, G., Sangiorgi, G., Airoldi, F., Chieffo, A., Michev, I., Montorfano, M., Carlino, M., Corvaja, N., Finci, L. and Colombo, A. (2005). Preliminary experience with the frontrunner coronary catheter: Novel device dedicated to mechanical revascularization of chronic total occlusions. *Catheterization and Cardiovascular Interventions*, volume 64, number 2, pp. 146–152.

[138] Palanichamy, P., Joseph, A., Jayakumar, T. and Raj, B. (1995). Ultrasonic velocity measurements for estimation of grain size in austenitic stainless steel. *NDT & E International*, volume 28, number 3, pp. 179–185.

[139] Patel, S. M., Menon, R. V., Burke, M. N., Jaffer, F. A., Yeh, R. W., Vo, M., Karmpaliotis, D., Azzalini, L., Carlino, M., Mashayekhi, K., Galassi, A. R., Rinfret, S., Ellis, S. G., Patel, M., Rangan, B. V., Karatasakis, A., Danek, B. A., Karacsonyi, J.,

Resendes, E., Banerjee, S. and Brilakis, E. S. (2018). Current perspectives and practices on chronic total occlusion percutaneous coronary interventions. *The Journal of invasive cardiology*, volume 30, pp. 43–50.

[140] Patel, V. G., Brayton, K. M., Tamayo, A., Mogabgab, O., Michael, T. T., Lo, N., Alomar, M., Shorrock, D., Cipher, D., Abdullah, S., Banerjee, S. and Brilakis, E. S. (2013). Angiographic success and procedural complications in patients undergoing percutaneous coronary chronic total occlusion interventions: A weighted meta-analysis of 18,061 patients from 65 studies. *JACC: Cardiovascular Interventions*, volume 6, number 2, pp. 128–136.

[141] Pavlakovic, B. (1998). *Leaky Guided Ultrasonic Waves in NDT.* Ph.D. thesis, University of London.

[142] Pigott, J. P., Raja, M. L. and Davis, T. (2012). A multicenter experience evaluating chronic total occlusion crossing with the wildcat catheter (the {CONNECT} study). *Journal of Vascular Surgery*, volume 56, number 6, pp. 1615 – 1621.

[143] Pishchalnikov, Y. A., Sapozhnikov, O. A., Bailey, M. R., Williams Jr, J. C., Cleveland, R. O., Colonius, T., Crum, L. A., Evan, A. P. and McAteer, J. A. (2003). Cavitation bubble cluster activity in the breakage of kidney stones by lithotripter shockwaves. *Journal of endourology*, volume 17, number 7, pp. 435–446.

[144] Precision Acoustics (2017). 2.0mm needle hydrophone. `https://www.acoustics.co.uk/product/2mm-needle-hydrophone/` (accessed on January 6, 2018).

[145] Precision Acoustics (2017). Fibre-optic hydrophones. `https://www.acoustics.co.uk/product/fibre-optic-hydrophones/` (accessed on January 6, 2018).

[146] Proudfoot, D. and Shanahan, C. M. (2001). Biology of calcification in vascular cells: Intima versus media. *Herz*, volume 26, number 4, pp. 245–251.

[147] Puckett, A. (2004). *An experimental and theoretical investigation of axially symmetric wave propagation in thick cylindrical waveguides.* Ph.D. thesis, The University of Maine.

[148] Puckett, A. D. (2000). *Fidelity of a Finite Element Model for Longitudinal Wave Propagation in Thick Cylindrical Wave Guides.* Master's thesis, Colorado State University.

[149] Qian, L., Li, M., Zhou, Z., Yang, H. and Shi, X. (2005). Comparison of nanoindentation hardness to microhardness. *Surface and Coatings Technology*, volume 195, pp. 264–271.

[150] Ra Medical (—). DABRA Atherectomy System. `https://www.ramed.com/cardiovascular/#products` (accessed on January 11, 2018).

[151] Rajendran, P., Rengarajan, T., Thangavel, J., Nishigaki, Y., Sakthisekaran, D., Sethi, G. and Nishigaki, I. (2013). The vascular endothelium and human diseases. *International Journal of Biological Sciences*, volume 9, number 10, pp. 1057–1069.

[152] Riel, L.-P. (2011). *Conception d'un générateur miniaturisé d'ondes mécaniques.* Master's thesis, Université de Sherbrooke.

[153] Riel, L.-P., Dion, S., Brouillette, M., Berube, S., Despatis, M.-A. and Bousser, E. (2014). Characterization of calcified plaques retrieved from occluded arteries and comparison with potential artificial analogues. Number 46469, p. V003T03A018.

[154] Riel, L.-P., Tanguay, J., Clavet-Lanthier, M. and Brouillette, M. (2016). Ex-vivo arterial exposure to guidewire-mediated shock waves. *Canadian Journal of Cardiology*, volume 32, number 10, pp. S159–S160.

[155] Rocha-Singh, K. J., Zeller, T. and Jaff, M. R. (2013). Peripheral arterial calcification: Prevalence, mechanism, detection, and clinical implications. *Catheterization and Cardiovascular Interventions*, volume 83, number 6, pp. E212–E220.

[156] Rogers, J. H. and Laird, J. R. (2007). Overview of new technologies for lower extremity revascularization. *Circulation*, volume 116, number 18, pp. 2072–2085.

[157] Roylance, D. (2000). *Beam displacement* (Technical report). Massachusetts Institute of Technology - Department of Materials Science and Engineering.

[158] Sakakura, K., Nakano, M., Otsuka, F., Ladich, E., Kolodgie, F. D. and Virmani, R. (2013). Pathophysiology of atherosclerosis plaque progression. *Heart, Lung and Circulation*, volume 22, number 6, pp. 399–411.

[159] Sanchis-Gomar, F., Perez-Quilis, C., Leischik, R. and Lucia, A. (2016). Epidemiology of coronary heart disease and acute coronary syndrome. *Annals of Translational Medicine*, volume 4, number 13, pp. 256–256.

[160] Sapontis, J., Salisbury, A. C., Yeh, R. W., Cohen, D. J., Hirai, T., Lombardi, W., McCabe, J. M., Karmpaliotis, D., Moses, J., Nicholson, W. J., Pershad, A., Wyman, R. M., Spaedy, A., Cook, S., Doshi, P., Federici, R., Thompson, C. R., Marso, S. P., Nugent, K., Gosch, K., Spertus, J. A. and Grantham, J. A. (2017). Early procedural and health status outcomes after chronic total occlusionÂăangioplasty. *JACC: Cardiovascular Interventions*, volume 10, number 15, pp. 1523–1534.

[161] Sathananthan, J. and Džavík, V. (2017). Coronary intervention for chronic total occlusion. *Coronary Artery Disease*, volume 28, number 5, pp. 426–436.

[162] Sato, T. and Hiroshima, J. (2011). Current situation of below the knee intervention in the patients of cli (critical limb ischemia) (poster c-1372). In *European society of radiology (Congress ECR 2011)*.

[163] Scheinowitz, M., Amrami, I., Oppenhaim, U., Engelberg, S., Schwartz, O., Belenky, A. and Siev-Ner, I. (2009). Crossing chronic total occlusions with a new 0.014" citop guidewire: Proof of concept. *Cathet. Cardiovasc. Intervent.*, volume 74, number 2, pp. 278–285.

[164] Schmerr, L. (2014). *Fundamentals of Ultrasonic Phased Arrays*. Solid Mechanics and Its Applications, Springer International Publishing.

[165] Schmerr, L. W. (2016). *Fundamentals of Ultrasonic Nondestructive Evaluation*. Springer.

[166] Schwartz, R. S., Edelman, E., Virmani, R., Carter, A., Granada, J. F., Kaluza, G. L., Chronos, N. A. F., Robinson, K. A., Waksman, R., Weinberger, J., Wilson, G. J. and Wilensky, R. L. (2008). Drug-eluting stents in preclinical studies: updated consensus recommendations for preclinical evaluation. *Circulation. Cardiovascular interventions*, volume 1, pp. 143–53.

[167] Selmon, M. R., Schwindt, A. G., Cawich, I. M., Chamberlin, J. R., Das, T. S., Davis, T. P., George, J. C., Janzer, S. F., Lopez, L. A., McDaniel, H. B., McKinsey, J. F., Pigott, J. P., Raja, M. L., Reimers, B. and Schreiber, T. L. (2013). Final results of the chronic total occlusion crossing with the ocelot system ii (connect ii) study. *Journal of Endovascular Therapy*, volume 20, number 6, pp. 770–781.

[168] Serruys, P. W., Hamburger, J. N., Fajadet, J., Haude, M., Klues, H., Seabra-Gomes, R., Corcos, T., Hamm, C., Pizzuli, L., Meier, B., Fleck, E., Taeymans, Y., Melkert, R., Teunissen, Y. and Simon, R. (2000). Total occlusion trial with angioplasty by using laser guidewire. the total trial. *European Heart Journal*, volume 21, number 21, pp. 1797–1805.

[169] Sethi, S., Mohammad, A., Ahmed, S. H., Germanwala, S., Sarode, K., Ortiz-Lopez, C., Banerjee, S. and Prasad, A. (2015). Recanalization of popliteal and infrapopliteal chronic total occlusions using viance and crossboss crossing catheters: a multicenter experience from the xlpad registry. *The Journal of invasive cardiology*, volume 27, pp. 2–7.

[170] Sharpe, W. N. (2007). *The Springer Handbook of Experimental Solid Mechanics*. Springer-Verlag New York Inc.

[171] Shetty, R., Vivek, G., Thakkar, A., Prasad, R., Pai, U. and Nayak, K. (2013). Safety and efficacy of the frontrunner xp catheter for recanalization of chronic total occlusion of the femoropopliteal arteries. *The Journal of invasive cardiology*, volume 25, pp. 344–7.

[172] Shockwave Medical (2017). Lithoplasty technology. `http://shockwavemedical.com/us/lithoplasty-technology/` (accessed on November 6, 2017).

[173] Shrivastava, S. (2004). *Medical Device Materials: Proceedings from the Materials & Processes for Medical Devices Conference 2003, 8-10 September 2003, Anaheim, California*. ASM International.

[174] Sianos, G., Werner, G. S., Galassi, A. R., Papafaklis, M. I., Escaned, J., Hildick-Smith, D., Christiansen, E. H., Gershlick, A., Carlino, M., Karlas, A., Konstantinidis, N. V., Tomasello, S. D., Di Mario, C. and Reifart, N. (2012). Recanalisation of

chronic total coronary occlusions: 2012 consensus document from the eurocto club. *EuroIntervention : journal of EuroPCR in collaboration with the Working Group on Interventional Cardiology of the European Society of Cardiology*, volume 8, pp. 139–45.

[175] Singh, G. D., Armstrong, E. J., Yeo, K.-K., Singh, S., Westin, G. G., Pevec, W. C., Dawson, D. L. and Laird, J. R. (2014). Endovascular recanalization of infrapopliteal occlusions in patients with critical limb ischemia. *Journal of Vascular Surgery*, volume 59, number 5, pp. 1300–1307.

[176] Smith, A. (2007). *Smith's Textbook of Endourology*. Pmph USA Ltd Series, BC Decker Incorporated.

[177] Spectranetics (2013). Product Catalogue - Turbo Elite.

[178] Srivatsa, S. S., Edwards, W. D., Boos, C. M., Grill, D. E., Sangiorgi, G. M., Garratt, K. N., Schwartz, R. S. and Holmes, D. R. (1997). Histologic correlates of angiographic chronic total coronary artery occlusions: influence of occlusion duration on neovascular channel patterns and intimal plaque composition. *Journal of the American College of Cardiology*, volume 29, pp. 955–963.

[179] Staniloae, C. S., Mody, K. P., Yadav, S. S., Han, S. Y. and Korabathina, R. (2011). Endoluminal treatment of peripheral chronic total occlusions using the crosserÂő recanalization catheter. *The Journal of invasive cardiology*, volume 23, pp. 359–362.

[180] Stanke, F. E. and Kino, G. S. (1984). A unified theory for elastic wave propagation in polycrystalline materials. *The Journal of the Acoustical Society of America*, volume 75, number 3, pp. 665–681.

[181] Steele, P. M., Chesebro, J. H., Stanson, A. W., Holmes, D. R., Dewanjee, M. K., Badimon, L. and Fuster, V. (1985). Balloon angioplasty. natural history of the pathophysiological response to injury in a pig model. *Circ Res*, volume 57, number 1, p. 105.

[182] Stemper, B. D., Yoganandan, N., Stineman, M. R., Gennarelli, T. A., Baisden, J. L. and Pintar, F. A. (2007). Mechanics of fresh, refrigerated, and frozen arterial tissue. *Journal of Surgical Research*, volume 139, number 2, pp. 236–242.

[183] Stone, G. W., Reifart, N. J., Moussa, I., Hoye, A., Cox, D. A., Colombo, A., Baim, D. S., Teirstein, P. S., Strauss, B. H., Selmon, M., Mintz, G. S., Katoh, O., Mitsudo, K., Suzuki, T., Tamai, H., Grube, E., Cannon, L. A., Kandzari, D. E., Reisman, M., Schwartz, R. S., Bailey, S., Dangas, G., Mehran, R., Abizaid, A., Moses, J. W., Leon, M. B. and Serruys, P. W. (2005). Percutaneous recanalization of chronically occluded coronary arteries: a consensus document: part ii. *Circulation*, volume 112, pp. 2530–7.

[184] Summit Medical Group (—). What is angioplasty? `https://www.summitmedicalgroup.com/library/adult_health/aha_angioplasty/` (accessed on January 11, 2018).

[185] Sutin, A. M., TenCate, J. A. and Johnson, P. A. (2004). Single-channel time reversal in elastic solids. *The Journal of the Acoustical Society of America*, volume 116, number 5, pp. 2779–2784.

[186] Suzuki, K., Saito, N., Zhang, G., Conditt, G., McGregor, J., Flynn, A. M., Leahy, D., Glennon, P., Leon, M. B. and Hayase, M. (2008). Development of a novel calcified total occlusion model in porcine coronary arteries. *The Journal of invasive cardiology*, volume 20, number 6, pp. 296–301.

[187] Suzuki, Y., Oyane, A., Ikeno, F., Lyons, J. K. and Yeung, A. C. (2009). Development of animal model for calcified chronic total occlusion. *Catheterization and Cardiovascular Interventions*, volume 74, number 3, pp. 468–475.

[188] Swaminathan, A., Vemulapalli, S., Patel, M. R. and Jones, W. S. (2014). Lower extremity amputation in peripheral artery disease: improving patient outcomes. *Vascular Health and Risk Management*, volume 10, pp. 417–424.

[189] Tang, X. M., Zhu, Z. and ToksÃűz, M. N. (1994). Radiation patterns of compressional and shear transducers at the surface of an elastic halfâĂŘspace. *The Journal of the Acoustical Society of America*, volume 95, number 1, pp. 71–76.

[190] ter Haar, G. (2007). Therapeutic applications of ultrasound. *Progress in Biophysics and Molecular Biology*, volume 93, number 1, pp. 111–129.

[191] Teraa, M., Conte, M. S., Moll, F. L. and Verhaar, M. C. (2016). Critical limb ischemia: Current trends and future directions. *Journal of the American Heart Association*, volume 5, number 2, p. e002938.

[192] Tesauro, M., Mauriello, A., Rovella, V., Annicchiarico-Petruzzelli, M., Cardillo, C., Melino, G. and Di Daniele, N. (2017). Arterial ageing: from endothelial dysfunction to vascular calcification. *Journal of internal medicine*, volume 281, pp. 471–482.

[193] Tiroch, K., Cannon, L., Reisman, M., Caputo, R., Caulfield, T., Heuser, R., Braden, G., Low, R., Stone, G., Almonacid, A. and Popma, J. J. (2008). High-frequency vibration for the recanalization of guidewire refractory chronic total coronary occlusions. *Catheterization and cardiovascular interventions : official journal of the Society for Cardiac Angiography & Interventions*, volume 72, pp. 771–780.

[194] Tol, S., Degertekin, F. L. and Erturk, A. (2017). Structurally embedded reflectors and mirrors for elastic wave focusing and energy harvesting. *Journal of Applied Physics*, volume 122, number 16, p. 164503.

[195] Tolvanen, S. (2016). *Microstructure and mechanical properties of Ti-6Al-4V welds produced with different processes*. Ph.D. thesis, Chalmers University of Technology.

[196] Topol, E. J. (2015). *Textbook of Interventional Cardiology*. Elsevier Science.

[197] Total Medical Solutions (–). Piculet : Active Micro-Catheter for CTO Crossing. `http://tmsolutions.eu/cto-peripheral-arteries/` (accessed on February 3, 2018).

[198] Tournat, V. (2014). *Introductory Lecture on Nonlinear Acoustics* (Technical report). Laboratoire d'coustique de l'Université du Maine (LAUM).

[199] Tsujita, K., Maehara, A., Mintz, G. S., Kubo, T., Doi, H., Lansky, A. J., Stone, G. W., Moses, J. W., Leon, M. B. and Ochiai, M. (2009). Intravascular ultrasound comparison of the retrograde versus antegrade approach to percutaneous intervention for chronic total coronary occlusions. *JACC: Cardiovascular Interventions*, volume 2, number 9, pp. 846–854.

[200] Ultran Group (2007). *University of Sherbrooke Piezoelectric Comparisons* (Technical report).

[201] Vassanelli, C., Menegatti, G., Zanolla, L., Molinari, J., Zanotto, G. and Zardini, P. (1994). Coronary vasoconstriction in response to acetylcholine after balloon angioplasty: possible role of endothelial dysfunction. *Coronary Artery Disease*, volume 5, number 12.

[202] Vogt, T. K. (2002). *Determination of material properties using guided waves.* Ph.D. thesis, University of London.

[203] Wahlstrom, S. (1985). The parabolic reflector as an acoustical amplifier. *J. Audio Eng. Soc*, volume 33, number 6, pp. 418–429.

[204] Walker, C. (2013). Guidewire selection for peripheral vascular interventions. *Endovascular today.*

[205] Welsch, G., Boyer, R. and Collings, E. W. (1993). *Materials Properties Handbook: Titanium Alloys.* Materials properties handbook, ASM International.

[206] Whitlow, P. L., Burke, M. N., Lombardi, W. L., Wyman, R. M., Moses, J. W., Brilakis, E. S., Heuser, R. R., Rihal, C. S., Lansky, A. J. and Thompson, C. A. (2012). Use of a novel crossing and re-entry system in coronary chronic total occlusions that have failed standard crossing techniques: results of the fast-ctos (facilitated antegrade steering technique in chronic total occlusions) trial. *JACC. Cardiovascular interventions*, volume 5, pp. 393–401.

[207] Willis, M., Homeister, J. and Stone, J. (2013). *Cellular and Molecular Pathobiology of Cardiovascular Disease.* Elsevier Science.

[208] Wilson, W. M., Walsh, S. J., Bagnall, A., Yan, A. T., Hanratty, C. G., Egred, M., Smith, E., Oldroyd, K. G., McEntegart, M., Irving, J., Douglas, H., Strange, J. and Spratt, J. C. (2017). One-year outcomes after successful chronic total occlusion percutaneous coronary intervention. *Cathet. Cardiovasc. Intervent.*, pp. n/a–n/a.

[209] Wojcik, G., Mould, J., Abboud, N., Ostromogilsky, M. and Vaughan, D. (1995). Nonlinear modeling of therapeutic ultrasound. In *Ultrasonics Symposium. Proceedings. An International Symposium.* IEEE.

[210] Wylie, M. (2011). *Arterial Tissue Perforation Using Ultrasonically Vibrating Wire Waveguides*. Ph.D. thesis.

[211] Yahagi, K., Davis, H. R., Arbustini, E. and Virmani, R. (2015). Sex differences in coronary artery disease: Pathological observations. *Atherosclerosis*, volume 239, number 1, pp. 260–267.

[212] Zeller, Thomas, M., Kambara, Antonio M., M., Moreira, Samuel M., M., Atar, Eliyahu, M., Chulsky, Alexander, M., Turgeman, Yoav, M., Sixt, Sebastian, M., Tepe, Gunnar, M., Rastan, Aljoscha, M. and Buchbinder, Maurice, M. (2012). Recanalization of femoropopliteal chronic total occlusions using the enabler-p balloon catheter system. *Journal of Endovascular Therapy*, volume 19, number 2, pp. 131–9.

[213] Zheng, P., Roll, J., Parmentier, B., O'Brien, J. and Crall, A. (2014). Therapeutic ultrasound for cto recanalization. *Endovascular Today*.

[214] Zoeram, S. A. and Mousavi, A. S. A. (2014). Laser welding of ti-6al-4v to nitinol. *Materials & Design*, volume 61, number Supplement C, pp. 185–190.

[215] Zukas, J. A. (2004). Chapter 3 shock waves in solids. In Zukas, J. A., *Studies in Applied Mechanics*, volume 49. Elsevier, pp. 75–102.

[216] Zysset, P. K., Edward Guo, X., Edward Hoffler, C., Moore, K. E. and Goldstein, S. A. (1999). Elastic modulus and hardness of cortical and trabecular bone lamellae measured by nanoindentation in the human femur. *Journal of Biomechanics*, volume 32, number 10, pp. 1005–1012.